Nagoya University

Development and Applications of
Tip-Scan High-Speed Atomic Force Microscopy
Combined with
Substrate Stretching Device

基板の一軸伸張機構を有する

探針走査型高速原子間力顕微鏡の開発

CHAN Feng-Yueh

詹 豐 嶽

December 5, 2022

Table of Content

Abstract

Nanometer-scale imaging technology with the air of atomic force microscopy (AFM) unveiled fruitful scientific insight into various areas, including biology, polymer, tribology, and metrology. Although dynamic imaging processes of both biological and non-biological processes have been long-standing challenging to the conventional apparatus, the emergence of high-speed AFM has allowed the direct observation of nanoscale dynamics processes of samples with subsecond temporal resolution and is very powerful in the analysis of single-molecule dynamics of various proteins. In addition, technological developments toward the multi-functionality of high-speed AFM, such as the combination with optical microscopy to enable more multifaceted analysis, have also been carried out.

One of the developments required to enhance the versatility of high-speed AFM is the mechanical manipulation of samples because the functions of proteins are often modulated by mechanical stress from an external environment. Thus, I developed a tip-scan-type high-speed AFM equipped with a uniaxial stretching mechanism for the substrate on which the sample is fixed to capture unprecedented dynamics under mechanical loads. As a demonstration of the application of the developed device to biological samples, I observed the stress-induced microtubule rupture process, the change in the affinity of actinin for the curvature of actin fibers, the curvature-sensitive binding affinity of BIN1 protein to the lipid membrane. Further, I applied the technique to non-living samples and observed morphological changes in latex films formed with polymer particles under an extreme strain of 140%.

These application studies effectively demonstrate that the high-speed AFM with uniaxial extension mechanism developed should be a versatile tool for analyzing nanometer-scale dynamics of samples under controlled mechanical stress and is expected to provide novel and innovative methods for life science and materials science.

Chapter 1 Introduction

1.1 Background

1.1.1 Atomic Force Microscopy

After atomic force microscopy (AFM) was invented,[1] this technology enabled superior spatial resolution in the air and rapidly acquired numerous attentions.[2] Instead of directly observing the light refracted from the sample, the AFM detects the deflection of the cantilever caused by the tip-sample interaction, and the surface of interest can be resolved with a vertical resolution of less than 1 Å by regulating a constant force exerted on the sample surface. The scheme of AFM is shown in Figure 1.1 (a). The application was then boosted with the invention of the dynamic AFM method,[3] in which the AFM cantilever is oscillated around its resonance frequency and scanning across the surface, as depicted in Figure 1.1 (b). As the cantilever oscillates above the sample, instead of scratching on it, the lateral force is reduced.

There are two major dynamic modes of AFM implemented: amplitude modulation AFM (AM-AFM) and frequency modulation AFM (FM-AFM). For both modes in common, the cantilever oscillating motion is captured by either interferometry,[3] optical lever method,[4,5] or self-sensing cantilever,[6] and converted to electrical signals. As the distance between the tip and surface changes, the oscillatory motion of the cantilever is varied, hence, the oscillation amplitude is changed, and the cantilever resonance frequency is shifted. The main difference between AM-AFM and FM-AFM is signal demodulation methods accordingly. The demodulated amplitude or frequency drift signal is fed to the close-loop system and regulates the tip-sample distance, thus maintaining a constant oscillatory amplitude or resonance frequency. The feedback signal is then processed with a computer to display the surface topography. The use of force detection thus allows AFM measurements can be performed in the air, liquid, or vacuum environments and is not restricted by the optical diffraction limit.

Apart from the versatile environments an AFM can operate in, another superiority of AFM over conventional optical and fluorescence microscopies is functional scalability. For instance, nanometer-scale physical properties, including thermal and electrical conductivity, and surface potential, are accessible simultaneously with topographic imaging. Among the available measurements, AFM-based mechanical property measurements have brought enormous attentions and have turned into a

standard tool for nano- and micromechanics. Among the available measurements, AFM-based mechanical property measurements have brought enormous attentions and have turned into a standard tool for micro- and nano-mechanics.[7,8] Nano- and micromanipulation techniques based on AFM[9,10] are categorized as trending
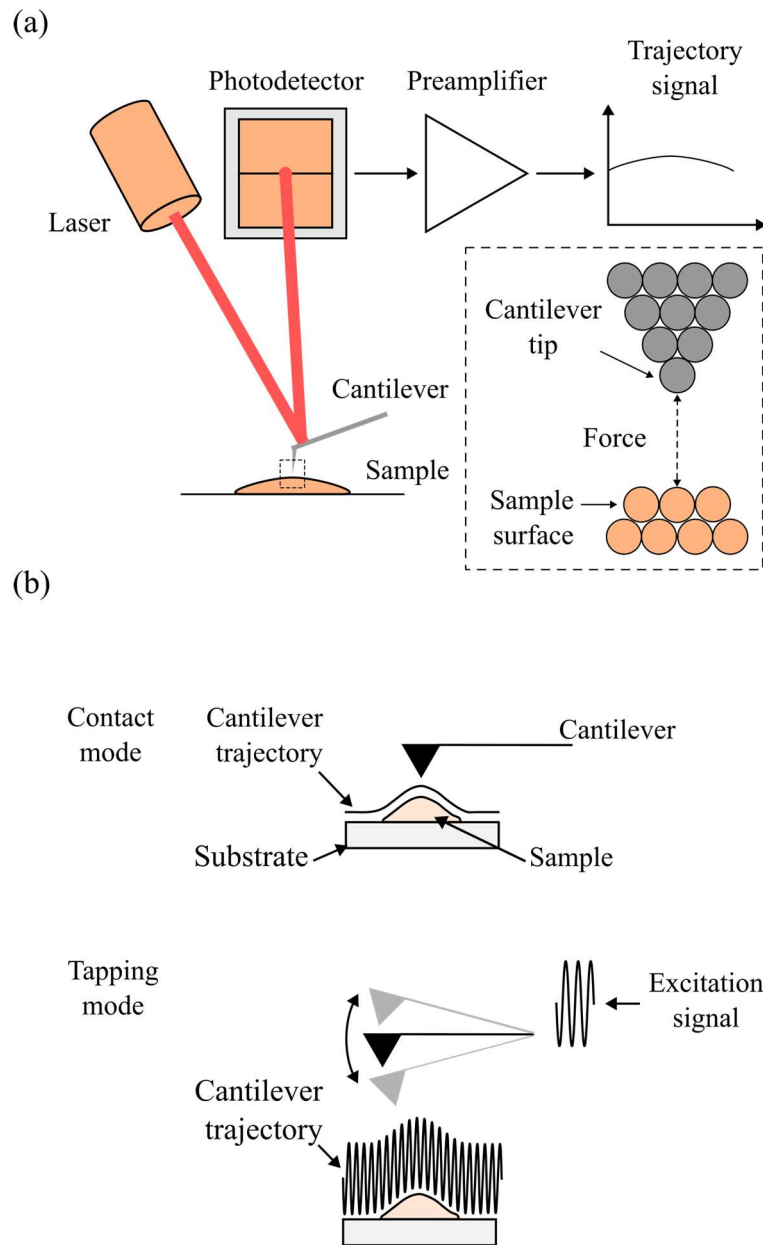
(a)

(b)

Figure 1.1   AFM operation principle. (a) Tip/sample interaction alters the cantilever deflection, which regulates the optical power distribution on the photodetector, hence modulating the topographic information on the electrical signal. (b) Two primary operation modes of AFM: contact mode and tapping mode.

nanomechanical methods and contribute further surface-focused understandings.[11,12] Other than snapshots from a region of interest (ROI), a functionalized AFM tip can unfold the proteins and elucidate the equilibrium conditions via the free-energy landscape.[13] Though probing the surface directly with AFM for quantitative properties is commonly adopted, one can also induce mechanical stimuli to the sample and monitor the evolution of topographical and physical properties. Using an AFM integrated with a sample stretcher, Liu et al. visualized the strain-induced local changes in modulus and polymer microdomain reorganization.[14] Cortelli et al. analyzed the electrical conductivity of the fractured gold layer deposited on the elastomer substrate to understand the electrical properties affected by tensile strain.[15] By combining substrate stretcher and in situ conductivity measurements, charge transportation between fragments was permitted by tunneling effect. Aside from the elastic materials, the development of breakage on stiff materials like bones was conducted by Qian et al., and the formation of nanobridge toughened the nanostructure, hindering the crack's growth resulting from tensile stress.[16] As the increasing analytic methods are introduced to AFM continuously, the surface-oriented studies stemming with AFM is still growing .

1.1.2 High-Speed AFM

While the development of AFM enabled observations at the atomic resolution on various surfaces, a conventional AFM requires several minutes for one image. The low data throughput thus circumscribed investigations to static samples or quasi-static processes. The tradeoff between spatial and temporal resolutions was alleviated with the emergence of high-speed AFM (HS-AFM). Figure 1.2 shows a typical system structure of HS-AFM. By improving scanner designs,[17–19] system feedback bandwidth,[20] and introducing miniaturized cantilevers,[21] imaging with the nanometer-scale resolution at millisecond per frame has been realized and enables the single-molecule observation of vibrant samples.[22] Appended to the low force perturbations[23] virtues, HS-AFM has recognized a go-to methodology for studying single-molecule dynamics and vulnerable materials such as cells[24] and hydrogels.[25] In addition, proteins at unprecedented spatial resolution can be acquired with high throughput HS-AFM images by localization methods.[26]

Therefore, for the last decades, HS-AFM has been used to investigate proteins, including ion-channels,[27] assembly chaperones,[28] cytoskeletons,[29] motor proteins,[30,31] and enzymes.[32]
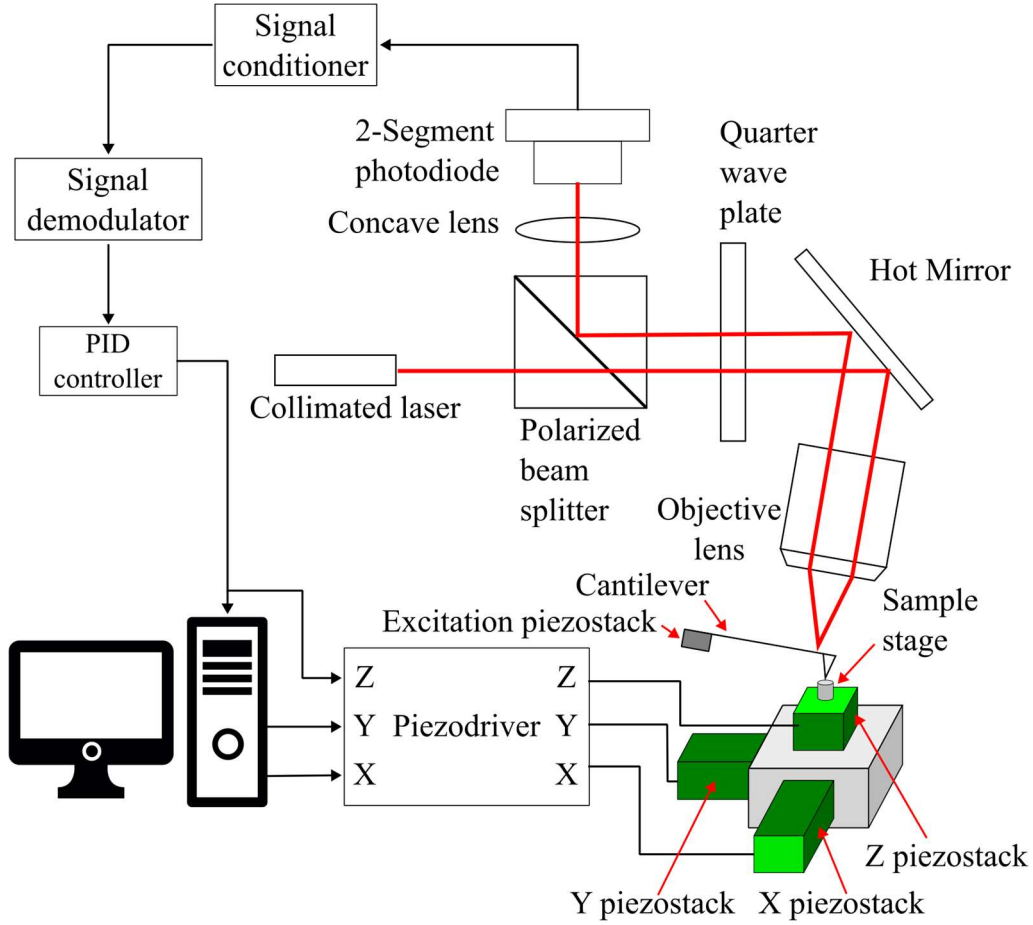
Figure 1.2   Scheme of a typical HS-AFM instrumentation.

1.1.3 HS-AFM Limitation & Motivation

Though the HS-AFM has extended the scanning speed to as low as tens milliseconds per frame, the persuasion of higher imaging speed has never been stopped. To describe the speed limitation of HS-AFM, the minimum bandwidth f_B of high-speed imaging is approximated[33] as

$$f_B = \frac{1}{8} / \left(\tau_c + \tau_{amp} + \tau_z + \delta \right), \tag{1.1}$$

where the response time of the cantilever, amplitude demodulator, and Z-scanner are denoted as τ_c, τ_{amp}, and τ_z, respectively. Uncategorized time delay in the system is denoted as δ. Each response time is expressed by

$$\tau_c = \frac{Q_c}{\pi f_c},$$ (1.2)

$$\tau_{amp} = \frac{\Delta\phi}{2\pi f_c},$$ (1.3)

and

$$\tau_z = \frac{Q_z}{\pi f_z},$$ (1.4)

where Q_c and f_c represent the quality factor and the resonance frequency of the cantilever, $\Delta\phi$ represents the phase lag attributed to the amplitude demodulation, and Q_z and f_z represent the quality factor and the resonance frequency of the Z-scanner, respectively. With the conventional setup of HS-AFM, response time τ_c, τ_{amp}, and τ_z were 0.4, 0.2, and 1.1 µs, respectively, with the following parameters: $f_c \sim 1.2$ MHz, $Q_c \sim 1.5$ in the liquid, $\Delta\phi \sim \pi/2$, $f_z \sim 150$ kHz, $Q_z \sim 0.5$ and $\delta = 0.1$µs. As can be seen that the time response τ_z of the Z-scanner is the primary limitation for achieving higher imaging speed above 70 kHz according to the equation. The required feedback bandwidth is further demanded if the sample fragility is included.[34] Attempts were reported to improve the signal demodulation speed[35] and control the quality factor of the cantilever;[36] however, the sample scanner still dominates the performance. By combining active damping[17] and using a smaller piezoelectric stack as a sample stage, $f_z \sim 1.1$ MHz was achieved;[37] however, a trade-off should be made with a smaller displacement a miniature piezoelectric stack can serve.

Though HS-AFM has been adopted widely for decades and the sample scanner designs are continuously improved as well as the motion controllers, electronics, and imaging processing techniques, mechanical manipulations on the samples or substrates were still challenging due to insufficient space around the Z-scanner for functional design. Figure 1.3 (a) shows the sample scanner images of the HS-AFM with a magnified view around the sample stage [Figure 1.3 (b)]. The high-speed scanner is placed over the fixed cantilever, and a glass rod is glued on the Z-piezostack (not shown, covered by black glue around the rod) as a sample stage. The magnified image clearly shows the dimensional limitation for designing a mechanical manipulator around the sample, not to mention the decreased f_z resulted from the additional weight of the manipulator.

The emergence of the tip-scan HS-AFM alleviated the hindrance of the functional design around the sample stage. Unlike the sample-scan method implemented on the HS-AFM, the tip-scan HS-AFM implements the cantilever/tip scanning with a piezo-actuated positioner and an adjustable hot mirror for the cantilever-deflection-detection laser to track the scanning cantilever. Other than the optical tracking system,[38] self-sensing cantilevers made of tuning forks[39] or deposited with piezoresistive materials[40] can translate the oscillatory trajectory of the cantilever into electrical signals. However, the self-sensing cantilever usually has a higher spring constant (>1 N/m) that would

(a)
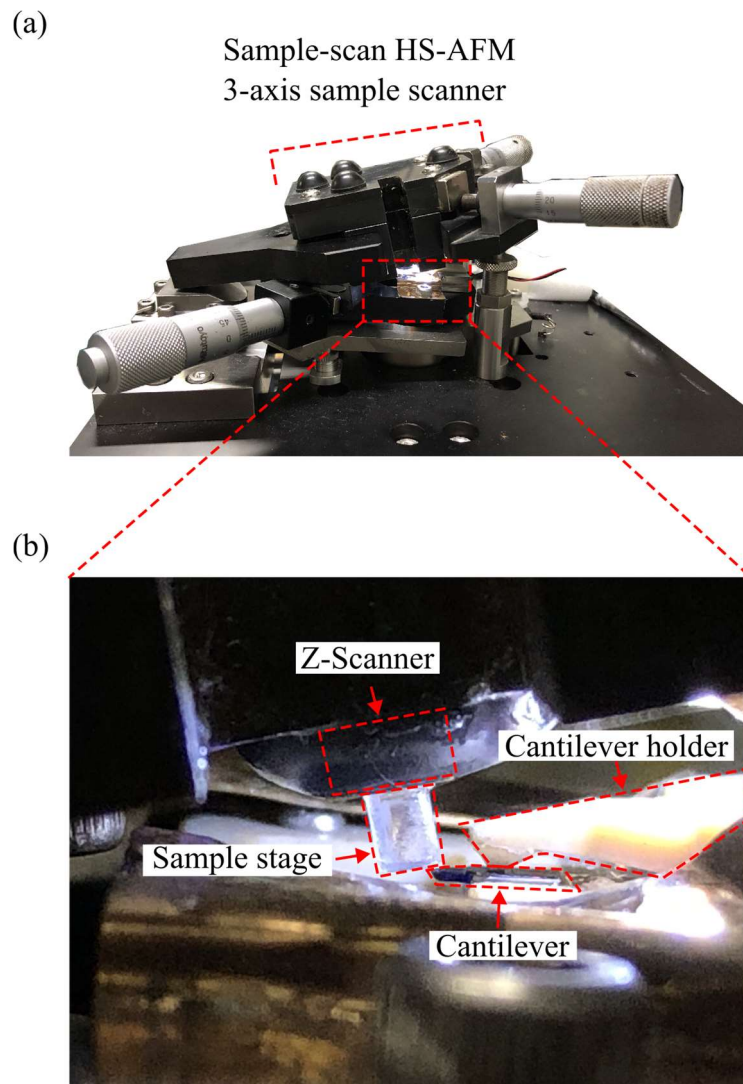
Sample-scan HS-AFM
3-axis sample scanner

(b)

Figure 1.3   Images on the sample area of the HS-AFM. (a) The sample scanner is settled above the cantilever (inside the dash-line box). (b) Magnified view of the sample scanner area. The cantilever is fixed by the cantilever holder, and the sample stage is brought close to the cantilever by z-scanner for imaging.

interfere with the imaging of biomolecules in the absence of ultrafine force control on the cantilever.[2,41] Integrating the laser/photodetector module into the mobile tip scanner is an alternative strategy to the self-sensing cantilever.[42] Yet, it resulted in a lower bandwidth of the scanner as weight increased. As the tip-scanning configuration allows the sample stage to be stationary, it is possible to incorporate diverse optical imaging methods such as total internal reflection fluorescence microscopy,[42] tip-enhanced optical imaging,[43] and awaited mechanical manipulator as described in this thesis.

While the success of HS-AFM development was proven with abundant researches delivered, the function demands on HS-AFM are yet fulfilled. In a recent discovery by HS-AFM, it was revealed that bent microtubules regulates the processive speed of the motor protein kinesin-1.[30] Although the bending curvatures of the microtubules were not controllable in the report, the demand for mechanical manipulation with HS-AFM lighted up the opportunity to combine tip-scan HS-AFM with a mechanical manipulator. Therefore, the study throughout this thesis is to bridge the gap between the HS-AFM and mechanical manipulation with a novel mechanism tailored for this purpose.

1.2 Structure of the Dissertation

The structure of this dissertation is arranged as follows. The development and characterization of the tip-scan HS-AFM are described in chapter 2. A newly designed stretching device for tip-scan HS-AFM is characterized in chapter 3. Substrate surface treatments to incubate different biomolecules for mechanical stimulation experiments are explained in chapter 4. Applications of the combined HS-AFM are demonstrated in chapter 5. In chapter 6, a conclusion and prospect of the tip-scan HS-AFM are provided.

Chapter 2 Development of Tip-Scan High-Speed Atomic Force Microscopy

The tip-scan HS-AFM developed in this thesis work consists of the following major modules: an optics system for detecting the cantilever deflection; a tip scanner for hosting the AFM cantilever; a laser tracking module to keep the laser spots on the mobile cantilever; a Q-controller for damping the tip scanner and extending the system bandwidth; and a sample scanner allows a slow imaging speed but has a wider scanning range than the high-speed scanner. Figure 2.1 shows the scanning module of the tip-scan HS-AFM developed in this thesis.
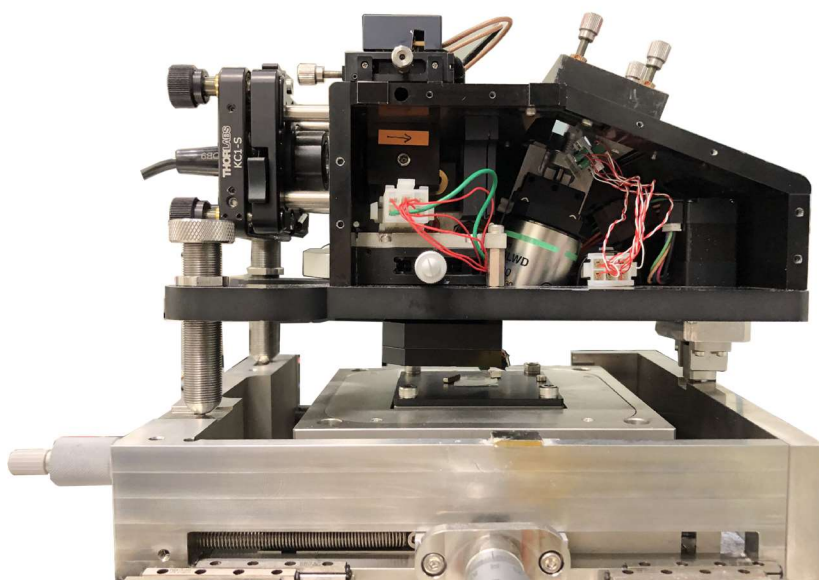
Figure 2.1   The tip-scan type HS-AFM developed in this thesis.

2.1 Optics

As the core of AFM, the topographic information and the sample's mechanical properties are modulated in the deflection of the cantilever during imaging. To derive the information, the physical trajectory of the cantilever needs to be converted into electrical signals for further processing. In this tip-scan HS-AFM, the optical lever detection method is adopted to resolve the cantilever motion

The optics diagram is depicted in Figure 2.2. The optics structure consists of the following components: a collimated laser source (laser diode: TLD78MZA6, Rohm,

Japan; collimation tube: LT110P-B, Thorlabs, Japan), a polarized beam splitter (PBS 102, Edmunds Optics, USA), a quarter wave plate (WPQ-7800-4M, Sigmakoki, Japan), a hot mirror (NT464-64, Edmunds Optics, USA), an objective length (CFI-TU-EPI-ELWD 20X, Nikon, Japan), a concave lens (CL5A, Thorlabs, USA), and a 2-segment photodetector (KA4PDAPCB, Graviton, Japan). The collimated laser beam propagates through the polarized beam splitter and the quarter-wave plate. It is then reflected by the hot mirror and passes through the objective lens to get focused on the back side of the gold-coated AFM cantilever (BL-AC10DS-A2, Olympus, Japan). The reflected laser beam returns via the original path until the polarized beam splitter then propagates toward the concave lens and finally is collected by the 2-segment photodetector. The cantilever's deflection changes the laser beam's reflection angle, hence changing the optical power distribution on the photodetector, and is then converted to the output electrical signal from the photodetector.
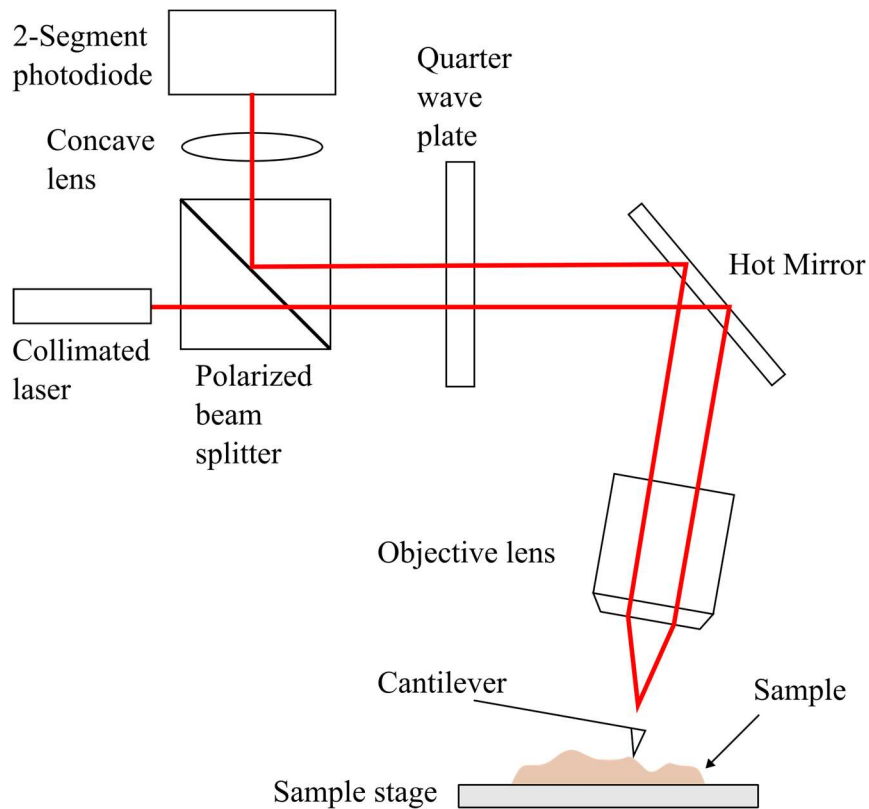

Figure 2.2   Optical diagram of the tip-scan HS-AFM.

2.2 Tip Scanner

As the tip of the cantilever interacts with the sample in a few nanometers range, it is essential to maintain such distance constant during scanning. The feedback control system regulates this off-plane precision displacement, and the controller output for distance regulation is then visualized as height data of topography. A tip scanner, therefore, carries the cantilever and scans over an area with nanometer-scale resolution, thus generating a nanometer-scale topography.

2.2.1 Tip Scanner Configuration

The tip scanner consists of four major parts: a flexure structure, piezoelectric stacks, a cantilever holder, and a scanner window, as shown in Figure 2.3. Stainless steel (SUS416) was chosen to make the frame of the tip scanner. The magnetic property of SUS416 allows the tip scanner to be held magnetically by the scanning head body with embedded magnets (NSC0001, Magfine, Japan), as shown in Figure 2.4. The piezoelectric stacks (X-axis and Z-axis: AE0203DF, Y-axis: AE0505DF, TOKIN, Japan) are held in place by a highly rigid structure with a fine bending flexure, enabling precision motion while maintaining high resonance frequency in all directions.

Figure 2.5 shows the frequency responses of the tip scanner at each axis. From the frequency responses, the resonant frequencies of X, Y, and Z are 40 kHz, 20 kHz, and
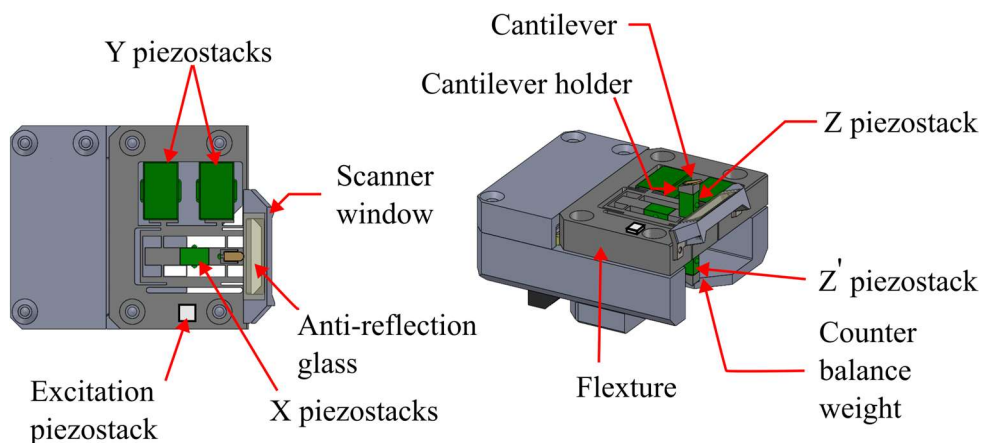

Figure 2.3   Models of tip scanner from top view (left) and isometric view(right).

94 kHz, respectively. Although the Y axis has the lowest resonance frequency, it works as the slow axis for a typical raster scanning pattern.

The cantilever holder, machined from duralumin for lightweight and stiffness consideration, has a trench size designed to host most of the commercially available AFM cantilevers. Figure 2.6 shows the relative location between the cantilever holder and other components. The flat side of cantilever holder is fixed on the z-actuator by the same two-component epoxy and curing time. To host the AFM cantilever, we apply a thin layer of wax (NP-0010, Ono Sokki, Japan) on the trench surface, then place the AFM cantilever on the surface with a gentle press. The wax is water-insoluble and can be easily cleaned and removed with ethanol. A comparison between wax fixation and conventional glue fixation will be discussed in the later section.

Many of the material properties varies with the environment. Of the most affected among the object, biological samples often require maintain hydrated to exhibit the natural conformation. Therefore, AFM observations of biological samples are mostly conducted in the aqueous environment. To avoid refracting laser at the air-liquid interface and bending AFM by the surface tension when scanning in the liquid, the scanner window of the tip scanner is designed to create a meniscus channel connected
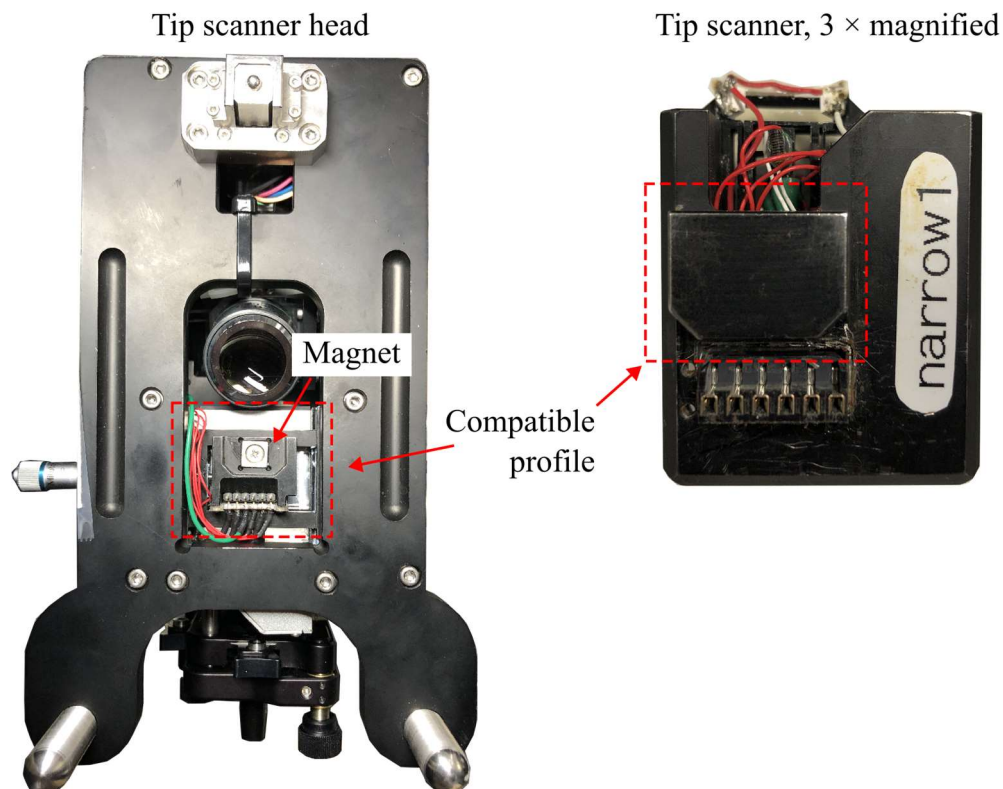
Figure 2.4   Tip scanner is installed on the scanner head via compatible profile and magnet. Image shows the associated surface of the scanner head and tip scanner.

from the tip scanner window, through the AFM cantilever, to the sample. To create a meniscus channel, the observation solution was carefully supplied within the gap between the scanner window and the glass substrate, as shown in Figure 2.7 (a). As the liquid amount increases, the liquid drop will expand to the substrate and forms a meniscus from the scanner window to the sample [Figure 2.7 (b)].
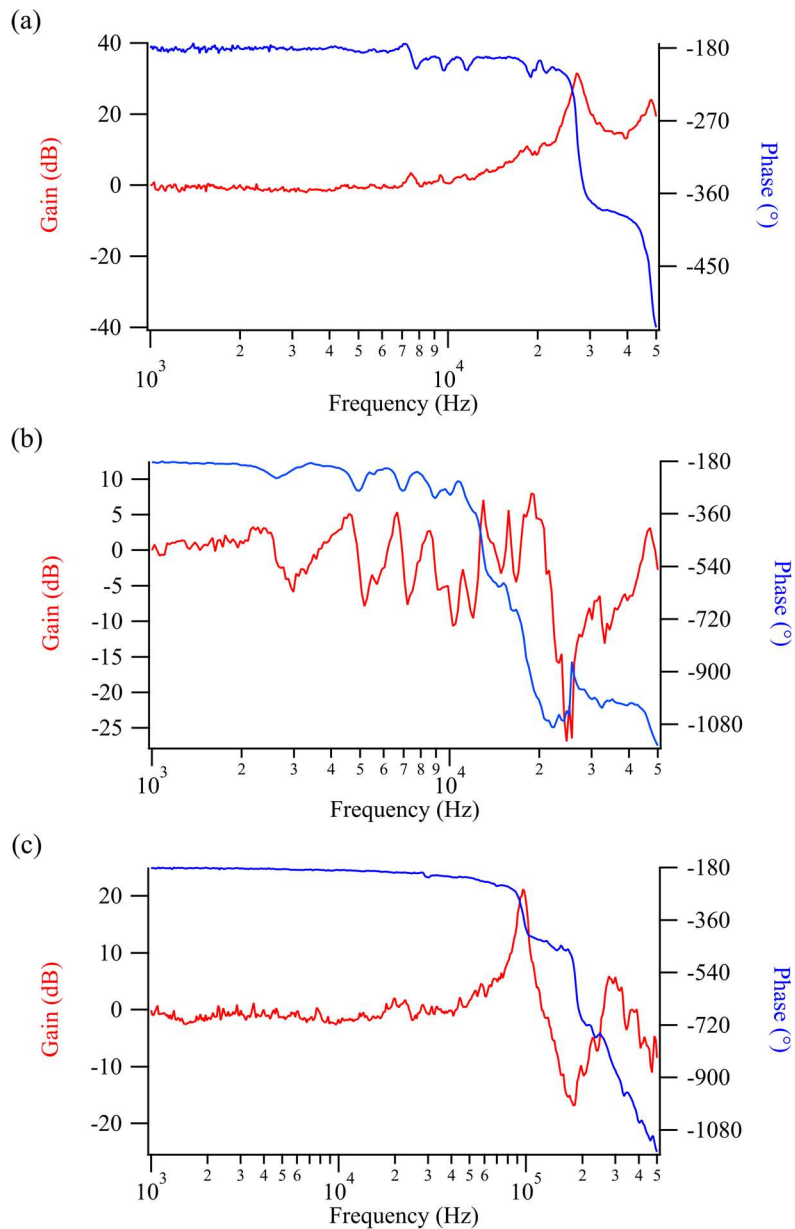
Figure 2.5   Frequency responses of the tip scanner in (a) X, (b) Y, and (c) Z directions.
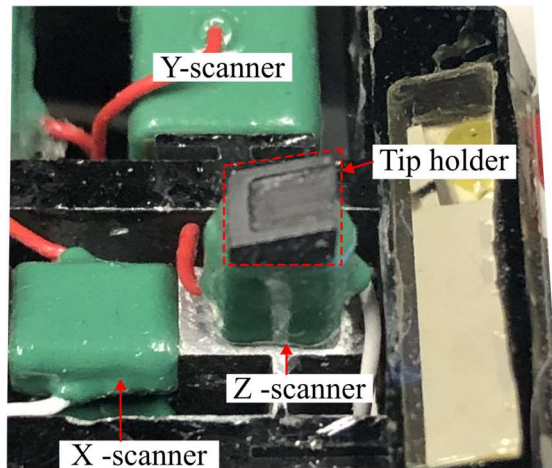
Figure 2.6   Duralumin made cantilever holder is glued on top of the Z-scanner. Trench on top of the cantilever holder is used to fix AFM cantilevers with wax.
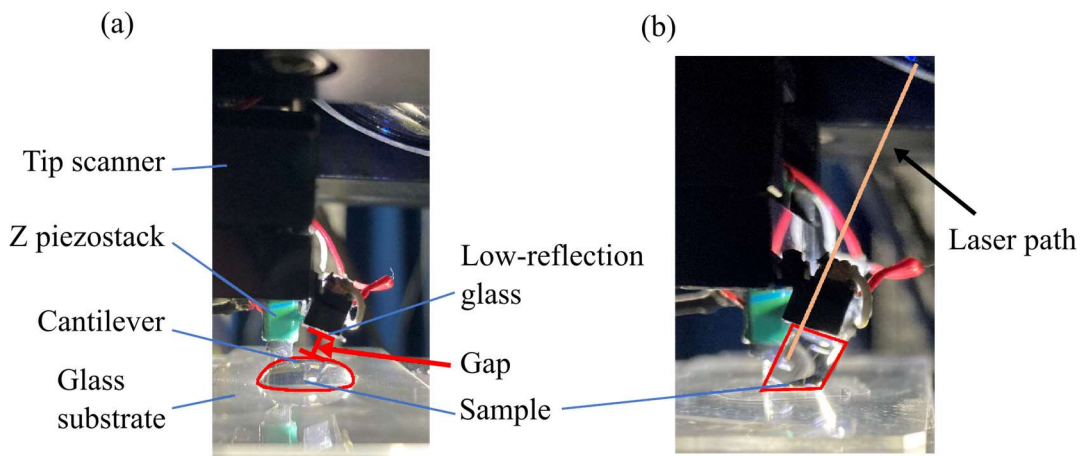
Figure 2.7   Formation of meniscus for AFM imaging in liquid. (a) Prior and (b) post the meniscus formation.

2.3 Q-controller

Quality factor (Q-factor) is a dimensionless parameter for a dynamic system to describe how fast the system loses its energy during the oscillation and can be derived by the ratio of natural frequency f_n to the full width at half maximum Δf. The illustrative definition is shown in Figure 2.8 (a). Figure 2.8 (b) demonstrates that for systems with

the same resonance frequency, the higher the Q-factor, the slower the system loses its energy, hence having pronounced ringing to a step response. An example of a high Q-factor object in our daily life is the bell from a church or a temple. For a precise measurement instrument, an excessive Q-factor would lead to undesired ringing behavior and deteriorate the measurement data. As can be seen from the z-scanner characterization section before, the frequency response of the z-scanner has a sharp peak at its first and second resonant frequencies with $Q \sim 13$ and 4, respectively. To avoid triggering the resonance frequency, the actuator needs to be driven at a lower speed, design a high bandwidth actuator, or eliminate the effect of the resonance by control methods .
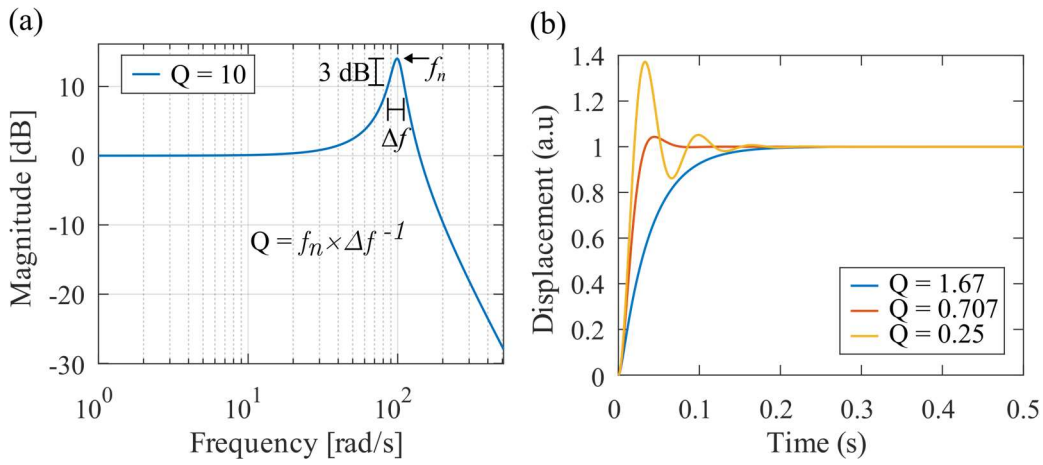
Figure 2.8   Explanation of Q-factor and its effects on dynamic systems. (a) Q-factor is derived from the f_n to full width at half maximum bandwidth ratio Δf. (b) Step responses of second-order system $G(s)$ with different Q-factors.
$G(s) = 10^4/(s^2 + 100Q^{-1}s + 10^4)$

2.3.1 Working Principle of Q-controller

Compared to the other existing solutions to damp an AFM system,[44] the Q-controller[17] has the merit of a simple structure, and it can be implemented by an analog or digital circuit as a plug-in module. The Q-controller comprises a mock second-order linear time-invariant (LTI) system and a differentiator. The control signal connects to the mock system and the real system simultaneously, where the mock system mimics the dynamics of the z-scanner and is followed by the differentiator to generate an estimated velocity signal. The velocity signal later sums up the control signal again and forms a

negative feedback system. The control diagram of the system, including the Q control, is illustrated in Figure 2.9.

The damping efficacy of the Q-controller on damping is described below. The system dynamics of a second-order LTI system with the Q-controller is expressed as follows:

$$\ddot{x} + 2\zeta\omega_n\dot{x} + {\omega_n}^2 = -\alpha\dot{x}, \tag{2.1}$$

where ζ and ω_n represents the damping ratio and resonance frequency of the system, respectively. The x is the system displacement that $\dot{x}$, and $\ddot{x}$ are the first- and second-time derivatives, whereas the α is the gain of the Q-Controller larger than zero.

The equation (2.1) is rearranged as follows:

$$\ddot{x} + (2\zeta\omega_n + \alpha)\dot{x} + {\omega_n}^2 = 0. \tag{2.2}$$

As $Q = \frac{1}{2\zeta}$, the damping ratio of the open-loop system is increased by incorporating the Q-controller, and the Q factor of the system is reduced equivalently.

2.3.2 Stability Analysis of Q-controller

The open loop system stability of connecting a Q-controller to the second-order LTI system is discussed here. The transfer function of a second-order linear expressed by the equation (2.2) can be described as
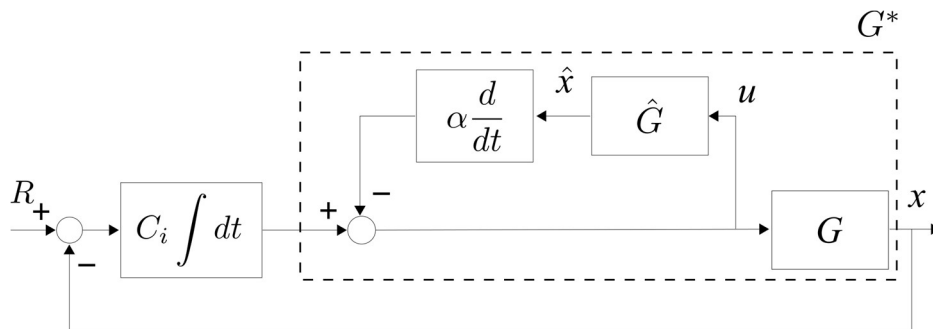
Figure 2.9   Control block diagram for analyzing the stability of the system G with the Q-controller G^*.

$$G^*(s) = \frac{1}{s^2 + (2\zeta\omega_n + \alpha)s + \omega_n{}^2} \qquad (2.3)$$

The characteristic equation of $G^*(s)$, $\Delta(s)$, is expressed as follows:

$$\Delta(s) = s^2 + (2\zeta\omega_n + \alpha)s + \omega_n{}^2 \qquad (2.4)$$

The roots of the characteristic equation, $s_1, s_{\bar{1}}$, are solved as

$$s_{1,\bar{1}} = \frac{1}{2}\left(-2\zeta\omega_n - \alpha \pm \sqrt{(2\zeta\omega_n + \alpha)^2 - 4\omega_n^2}\right) \qquad (2.5)$$

Thus, the damped system is stable if and only if all roots are located at the left-hand plane, which yields

$$\alpha > -2\zeta\omega_n \qquad (2.6)$$

Equation (2.6) indicates the open loop LTI system is asymptotically stable when a Q-controller is connected as α is defined greater than 0. Next, we close the loop with an integral controller,

$$C_i(s) = \frac{\beta}{s}, \qquad (2.7)$$

where β is the integral gain. The closed-loop transfer function, $G^*_{cl}(s)$, is expressed as

$$G^*_{cl}(s) = \frac{\frac{\beta}{s}G^*}{1 + \frac{\beta}{s}G^*} \qquad (2.8)$$

$$= \frac{\beta}{s^3 + (2\zeta\omega_n + \alpha)s^2 + \omega_n{}^2 s + \beta} \qquad (2.9)$$

The characteristic equation of the closed-loop system is f

$$\Delta_{cl}(s) = s^3 + (2\zeta\omega_n + \alpha)s^2 + \omega_n{}^2 + \beta. \qquad (2.10)$$

The closed loop system is asymptotically stable if and only if all the following

17

conditions are achieved:

$$\begin{cases} 2\zeta\omega_n + \alpha > 0, \\ \beta > 0, \\ (2\zeta\omega_n + \alpha)\omega_n^2 > \beta. \end{cases} \tag{2.11}$$

From the inequality equation (2.11), it can be seen that the upper limit of the integral gain β is extended when the system includes the Q-controller. Therefore, the Q-controller allows to use higher integral gain during faster scanning and prevents the system from ringing.

2.3.3 Experimental Result

The frequency response of the z-actuator of the tip scanner was discussed in the previous section. Following that, the Q-controller was configured to match the frequency response of the z-actuator, and the performance of damping was evaluated.

Figure 2.10 (a) shows the frequency responses of the z-scanner and the configured Q-controller. The red and blue dashed lines represent the gain and phase of the z-actuator, respectively. The solid lines are for the mocked system where the gain is in red, and the phase is in blue. As can be seen in Figure 2.10 (a), the z-actuator (dashed line) has the first resonance frequency at 94 kHz and the second at 240 kHz. The configured Q-controller was then used to damp the first two modes of the z-scanner. A comparison of the response characteristics of the Z piezo-actuator when the Q-controller is inactive (Q-off) and active (Q-on) is shown in Figure 2.10 (b). When the Q-controller was connected to the z-actuator and turned on, the first peak was greatly damped Q-factor of the first resonance was decreased from 13 to 0.5. The second resonance was also effectively damped to -8 dB, which is below the DC level and does not contribute to the system instability. As a result, the Q-controller configured here is integrated into the tip-scan HS-AFM and preventing the z-scanner from ringing at high-speed scanning.
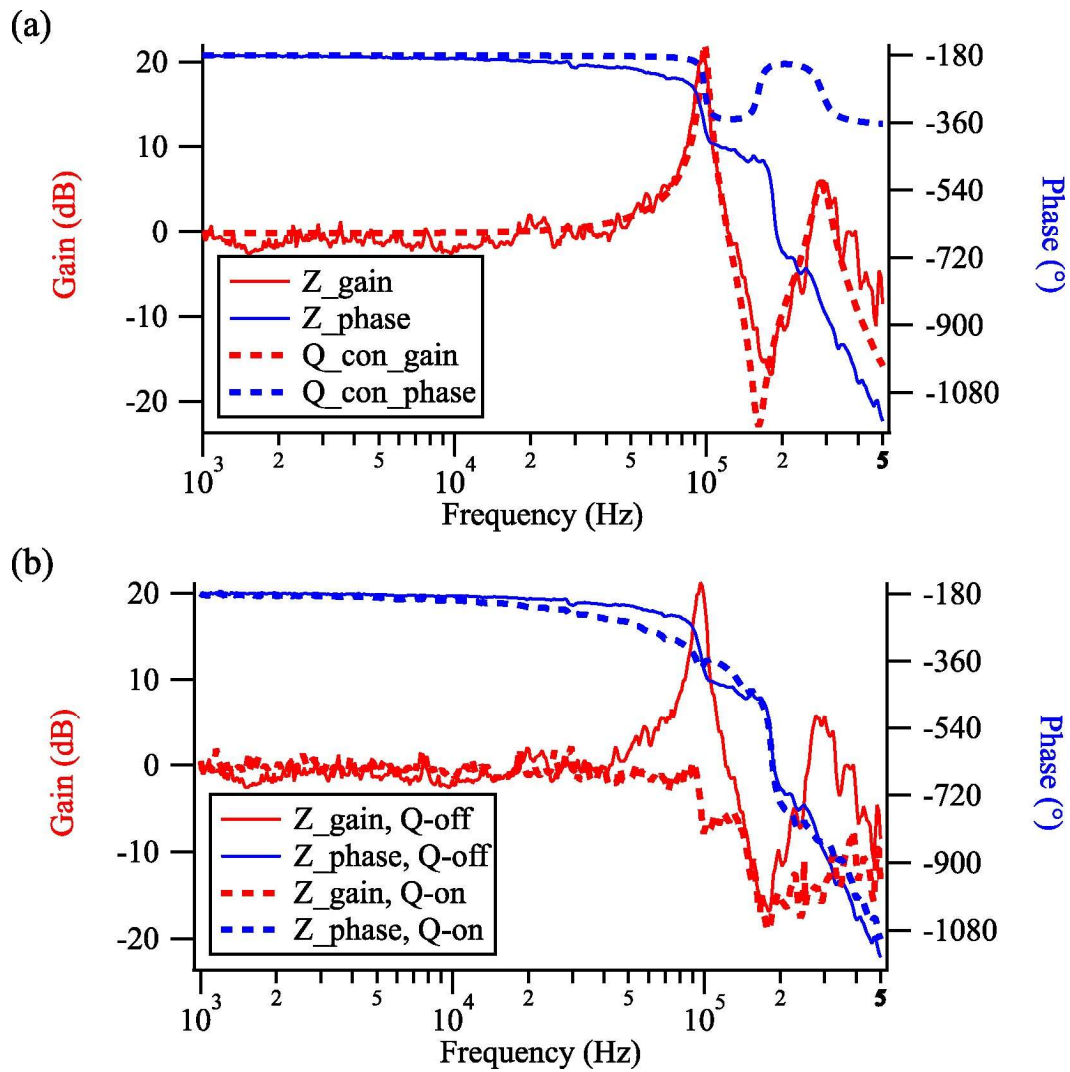
Figure 2.10   Frequency spectrum of the z axis actuator with Q-controller. (a) Q-controller (solid line) was modeled to match the z axis actuator (dash line). (b) The first two resonance were damped as Q-controller was active (dash line) compared to inactive (solid line).

2.4 Laser Tracking

2.4.1 Background

Compared to the sample-scan HS-AFM, the tip-scan HS-AFM using an optical lever detection scheme faces a major challenge with laser tracking on the cantilever. The cantilever is fixed on the mobile piezoelectric stage, while the laser component in the structure is static. As the tip scanner scans over the sample area, it is expected that the laser reflection from the cantilever will not be consistent over the scanning area. For an amplitude modulation AFM used in this study, the inconsistent laser illumination leads to the undesired amplitude change, resulting in an excessive force on the sample and making feedback control impossible.

The reported solutions to the laser tracking problem can be classified into two types, as illustrated in Figure 2.11. First, in an integrated module settled above a precision positioner, the optical module is combined with the tip scanner, as shown in Figure 2.11 (a). This method resolves the laser tracking problem; however, the drawback of the integrated module is that the operating bandwidth is greatly reduced because the tip scanner has to carry the additional load from the bulky alignment mechanism.

A self-sensing cantilever method is another solution to the laser alignment problem. A simplified self-sensing method is illustrated in Figure 2.11 (b). Unlike the optical level detection scheme, the self-sensing cantilever does not require a laser to detect cantilever deflection. The self-sensing cantilever is usually made from silicon nitride cantilever with a layer of piezoresistive material coated on either side of the cantilever. When the force is applied to the cantilever, the electrical signal is induced by the deformation of the piezoresistive material and amplified by the following instruments for imaging the surface properties. Although the self-sensing cantilever provides an alternative to the optical lever detection technique and eliminates the optical components for measurements, the main pitfall of the self-sensing cantilever is its spring constant and resonance frequency. Most of the reported self-sensing cantilevers have a spring constant from 1 to 20 N/m, and the resonance frequency in the air is below 100 kHz. For example, the commercially available HS-AFM cantilever, AC10 from Olympus, has a spring constant of about 0.1 N/m and a resonance frequency of around 1.5 MHz in the air. Therefore, it is substantially inapplicable to high-speed imaging of biomolecules.
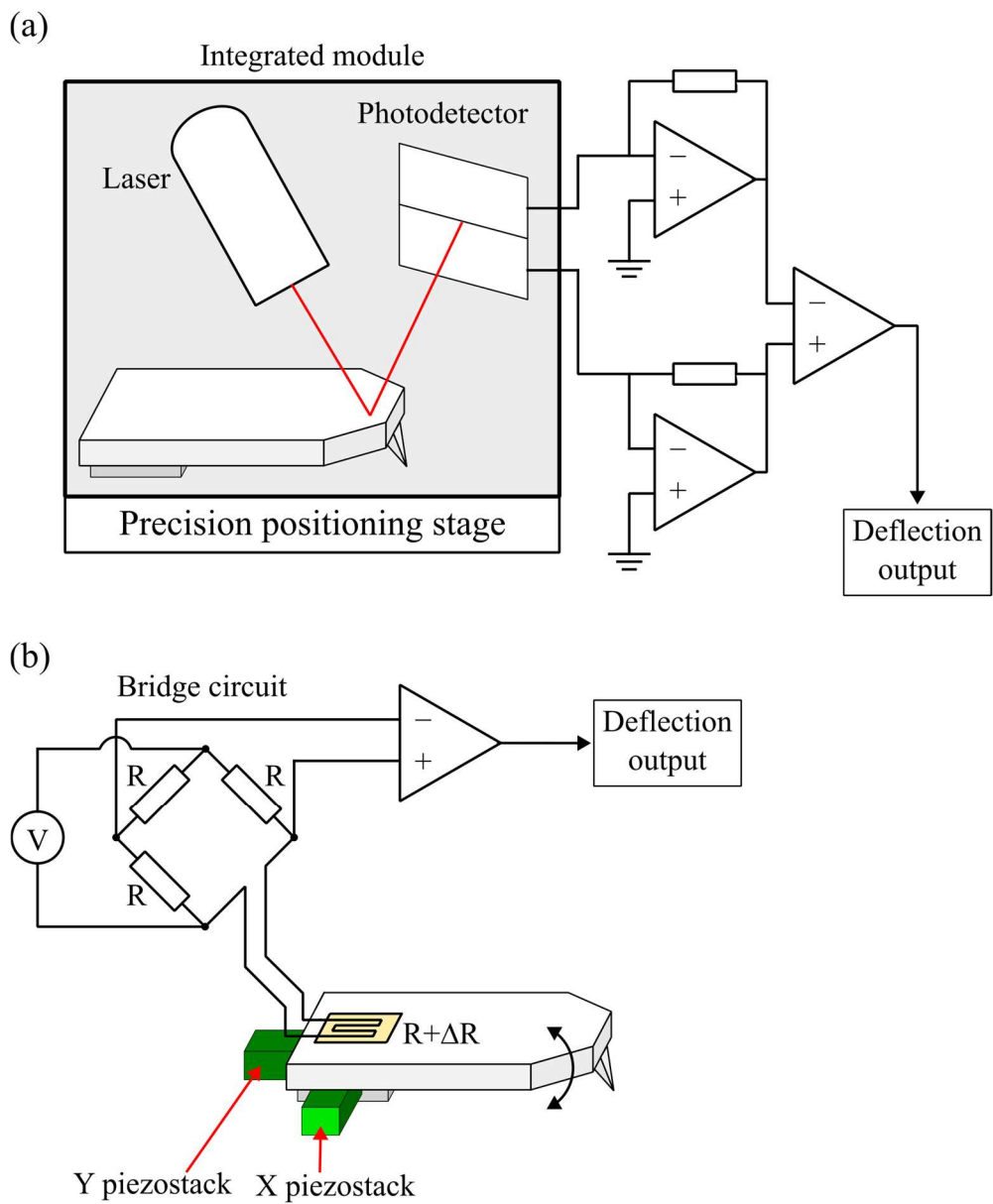
Figure 2.11   Exemplar implementation of cantilever sensing. (a) Self-sensing cantilever method, and (b) integration of laser module and scanner (conceptual).

2.4.2 Laser Tracking

In the tip-scan HS-AFM developed in this study, optical lever detection method is adopted for detecting the cantilever deflection, and the laser tracking on the cantilever motion is accomplished by a controllable tilt hot mirror which allows the laser to follow the scanning cantilever, as illustrated in Figure 2.12 (a) and modeled in Figure 2.12 (b).

The hot mirror is supported by two sets of piezoelectric stacks for rotating about two orthogonal axes that the mirror rotational motion is synchronized with the tip scanner's motion in a feedforward fashion. The tracking performance was evaluated by scanning the cantilever in the aqueous environment while no contact with the substrate or sample was made. The AC10 cantilever was initially aligned with the laser and oscillated around the resonance frequency with an amplitude of 10 nm. The amplitude of the oscillating cantilever was then recorded and visualized as amplitude images. Figure 2.12 (c) shows the amplitude image of AFM scanning within the scan area of 900×900 nm^2. As can be seen, the amplitude image shows a larger variation when the laser tracking was inactive. Figure 2.12 (d) shows line profiles taken from Figure 2.12 (c) along the red line to evaluate the amplitude variation caused by laser alignment. When the tracking was inactive, the maximum amplitude variation was about 2.5 nm with a standard deviation of 0.65 nm. When the tracking was activated, the maximum variation was reduced to about 0.5 nm with a standard deviation of 0.25 nm. As a result, the maximum variation of amplitude was reduced from 25% to 5%. The tip force exerted on the sample during scanning can be approximated with the following equation:[45]

$$F_{tip} = (k_c/Q_c) \times h_0 \times sin(\theta/2) \tag{2.12}$$

where, k_c and Q_c are 0.1 N/m and ~ 2 in water for AC10 cantilevers from Olympus, h_0 is the laser tracking resulted amplitude error, and θ is the phase lag of the feedback system, for which 30° is assumed. From equation (2.12), the maximum force exerted on the sample contributed to amplitude error was reduced from 32 pN to 6.5 pN. It is important to avoid sabotaging the samples or disturbing the fragile interactions between proteins. For example, the conformational change of the Piezo1 protein can be activated as low as 60 pN and resumed when the force is reduced to below 30 pN;[46] binding between F-actin and α-actinin can be interrupted at 18 pN.[47] Thus, the implemented laser tracking of the tip-scan HS-AFM is a crucial step toward dynamic process imaging.
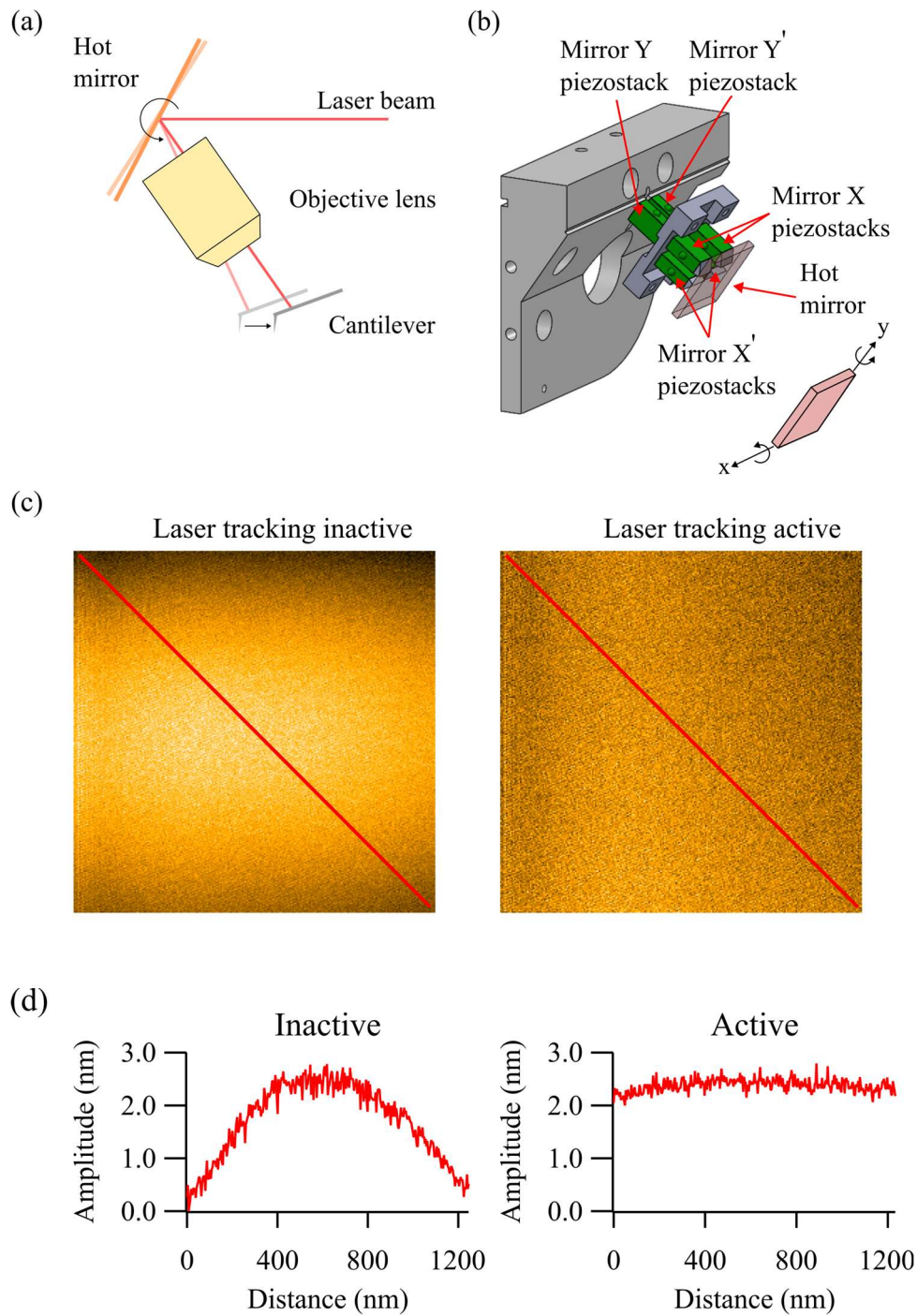
Figure 2.12　Laser tracking method. (a) Scheme of tracking principle. (b) Illustration of the hardware implementation. Mirror X piezostacks are driven in opposite direction respect to Mirror X' piezostacks, results the mirror rotation along the x axis. Mirror Y piezostack and Mirror Y' piezostack are driven in the same method. (c) Amplitude images of laser tracking inactivated and activated scanning. (d) Line profiles taken from amplitude images. The line profiles for both images are offset by -2.5 nm.

2.4.3 Cantilever Fixation Methods

For a tip-scan HS-AFM, the cantilever should be fixed by applying water-insoluble glue to the contact surface between the cantilever and the holder if no mechanical clamp mechanism is involved. However, using glue to fix the cantilever has a time-consuming process. If a rapid exchanging cantilever situation is required, the glue should be cured rapidly as well. However, the short curing time of the glue also means dexterous skill
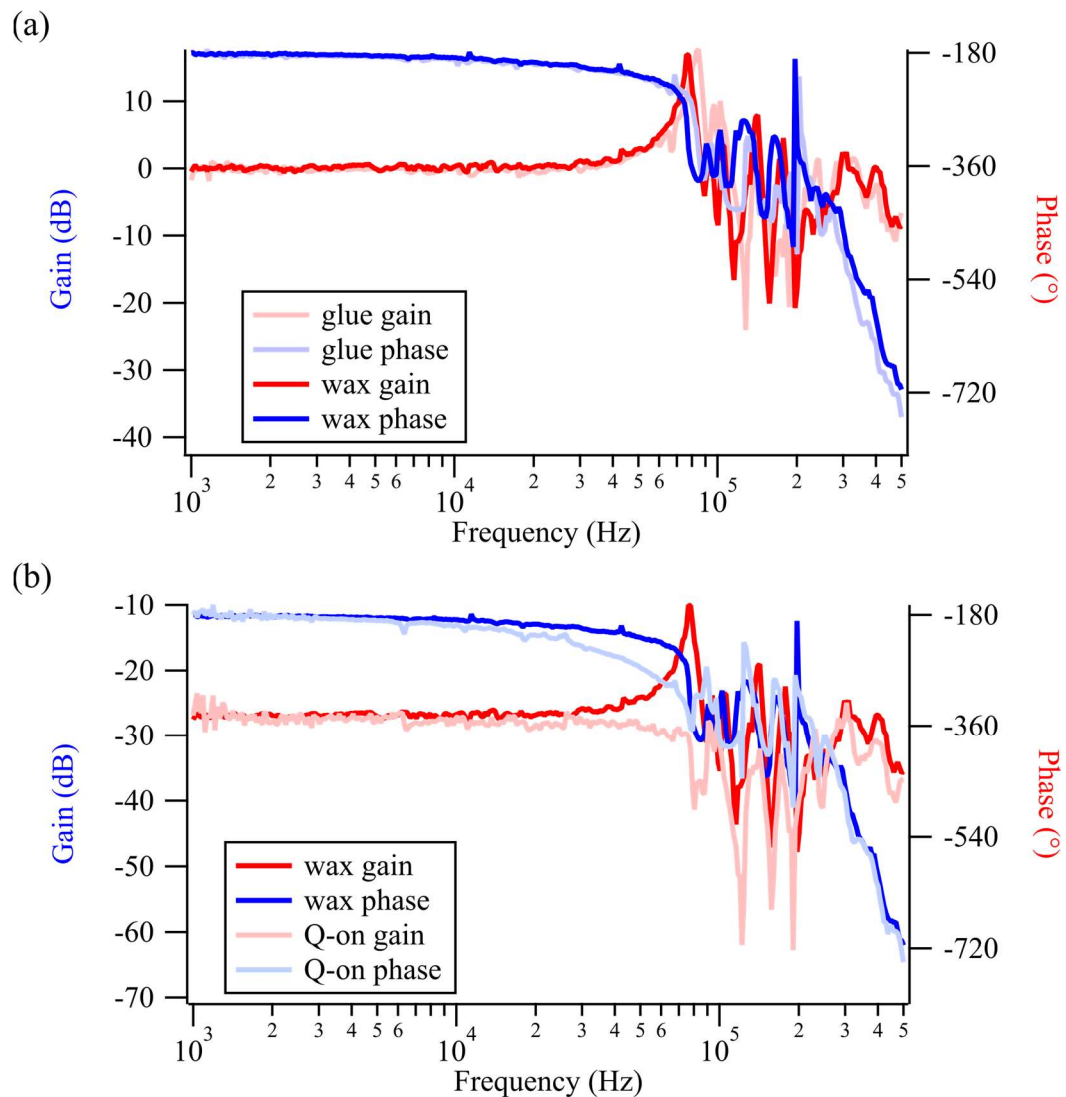
Figure 2.13   Comparison between wax and glue fixation on Z-scanner frequency response. (a) Frequency response of wax and glue fixation. (b) Effect on Q-controller damping performance with wax fixation.

for setting the cantilever in place is much more required than a slow-cured glue. Using water-insoluble glue also means that a solvent-based cleaning process to detach the cantilever from the holder is usually demanded, which increases the risk to damage the surrounding piezostacks by solvents.

To overcome this problem, fixation wax (NP-0010, ONO SOKKI, Japan) was introduced in our instrument. The merits of the wax mounting technique include the shorter mounting and unmounting time for the cantilever and excludes the need for a solvent-based dissolving process.

As described in the HS-AFM limitation section, the bandwidth of the z-scanner is the bottleneck for fast scanning. Therefore, the frequency responses of the cantilever mounted on the holder with different fixation methods were examined, as shown in Figure 2.13 (a). The result shows that the resonance frequency of the z-scanner decreased from 84 kHz to 76 kHz after adopting the fixation method from glue to wax. Despite that, the resonant peak is effectively suppressed when Q-controller is activated, resolving a bandwidth of around 70 kHz of the scanner, as plotted in Figure 2.13 (b). A possible reason for the resonance frequency shift is the wax layer changes the damping behavior between the cantilever and the holder. A simplified system is illustrated in Figure 2.14. A mass-spring-damper model in which the wax or glue layer altered the spring constant K_2 and damping constant C_2. The cantilever is modeled as M_1 whereas the piezostacks/holder assembly is modeled as M_1-C_1-K_1. As the wax is less stiff than the cured glue in general, the overall resonance frequency is decreased when the wax is used to join the cantilever and the holder. Although the resonance frequency is decreased, the bandwidth of the Z-scanner with the Q-controller is still high enough to image the fragile biomolecule structure at 500 ms per second without damaging the structure, as shown in the following characterization section.
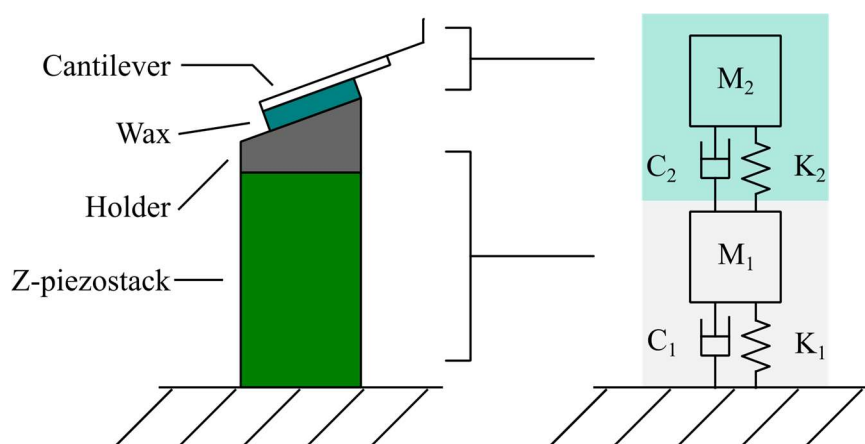

Figure 2.14   Simplified dynamic model of z-axis actuator for wax fixation.

2.5 Evaluation of the Tip Scanner

Conventional AFMs usually use test grating to calibrate and evaluate the scanner's performance, including spatial and temporal resolutions. These gratings are generally made from silicon dioxide with well-defined repetitive patterns. Despite the precise dimension of the test grating, scanning on a tough sample does not demonstrate the applicability of AFM on soft samples. Thus, the tip scanner was evaluated by scanning the proteins whose structure dimensions are well studied, including actin filament (F-actin) of the cytoskeleton and GroEL of molecular chaperones. AFM images were scanned with an ultra-small cantilever (BL-AC10DS-A2, Olympus, Japan) which has a nominal size of $10 \times 2 \ \mu m^2$ and a thickness of 130 nm. A bird-beak-like protrusion at the free end serves as a probing tip having a radius of around 24 nm. The spring constant of the cantilevers is 0.1 N/m nominally. The probe was further sharpened to a radius of around 2 nm by growing a carbon tip on the original silicon nitride tip by electron beam deposition, followed by plasma etching. All images were recorded in tapping mode. The resonance frequency of the cantilever was typically 510 kHz in the water and the free oscillation amplitude A_0 was driven to 4 nm, and $0.8A_0$ was set as the setpoint of the feedback control.

2.5.1 Actin Filament & α-actinin

First, the horizontal spatial resolution of the tip scanner was evaluated by imaging actin filament (F-actin) in the liquid. F-actin, one of the three cytoskeleton proteins, is polymerized from globular actin monomer (G-actin) which weighs around 42 kDa. F-actin has a right-handed double helix structure with a periodicity of 37 nm, as illustrated in Figure 2.15 (a), and thus is the ideal sample for characterizing the in-plane spatial resolution of the AFM scanner at the nanometer scale.

F-actin used for characterization was polymerized from the G-actins described below. 1 mg G-actin powder (AKL99, Cytoskeleton, Inc., USA) was first dissolved in the 100 μL pure water (Direct-Q UV3, Millipore, USA) and reconstituted in the Tris-based buffer (5 mM Tris-HCl pH 8.0, 0.2 mM $CaCl_2$, 0.2 mM ATP, 5% (w/v) sucrose, and 1% (w/v) dextran). The G-actin solution was further polymerized at room temperature for 1 hour in the polymerization buffer (100 mM KCl, 2 mM $MgCl_2$, 1 mM EGTA, 0.2 mM ATP) at the G-actin concentration of 10 μM. Finally, phalloidin was added to the solution at a double molar ratio to the actin to inhibit the F-actin from depolymerization. The resulting F-actin was preserved at 4 °C before use.

As the F-actin's negatively charged surface, negatively charged mica surface needs

to be modified for adsorbing the F-actin. Freshly cleaved mica was silanized with 1% (3-aminopropyl)triethoxysilane (APTES) (LS-3150, Shin-Etsu Silicone, Japan) for 3 minutes. The silanized surface was then rinsed with the imidazole buffer (20 mM imidazole, 2 mM $MgCl_2$, 25 mM KCl, 1 mM DTT, and 1 mM EGTA). 5 μL of 10 μM F-actin solution was deposited on the modified surface and incubated for 10 minutes. The surface was rinsed again with the imidazole buffer to remove excessive F-actin. The imidazole buffer was then used for AFM imaging as well.

Figure 2.15 (b) shows the AFM image of the F-actin incubated on the mica surface obtained by using the tip scanner. The double helix structure with a periodicity
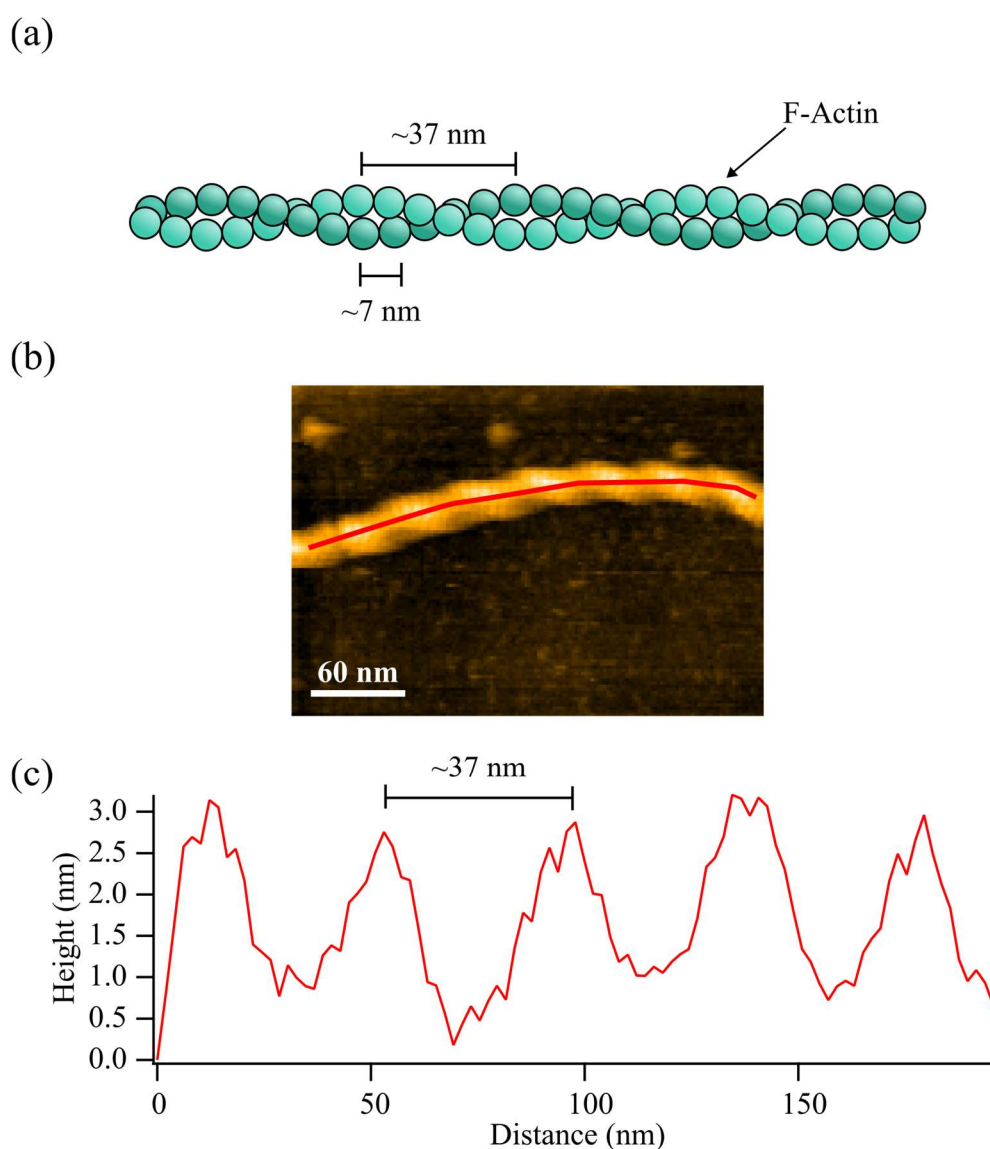

Figure 2.15   Evaluation of tip scanner with F-actin. (a) Illustrtation of actin filemnet. (b) HS-AFM image of F-actin on mica surface. (c) Lineprofile taken from the AFM image alogn the red line in (b).

of 37 nm can be seen at 500 ms/frame, as shown in Figure 2.15 (c). Also, the individual monomer on the filament is clearly visible. This observation shows that the tip-scan HS-AFM had a nanometer scale resolution at high-speed scanning without damaging the sample.

α-actinin is an actin-binding protein with a molecular weight of 100 kDa. α-actinin bridges F-actins to form sarcomeres and stabilizes the contractile apparatus of muscles, as illustrated in Figure 2.16 (a). Besides the mechanical role of bundling the F-actins, it is known that α-actinin is also a multitasking protein that plays roles in interacting with membrane and signaling proteins[48].

Here, tip-scan HS-AFM was used to observe the bridging between α-actinins and F-actins in the liquid. 50 μg α-actinin in the powder form (AT-01, Cytoskeleton, Inc., USA) was reconstituted with 50 μL pure water, followed by the aliquot, and flashed frozen. α-actinin aliquots were stored at -80 °C. The thawed α-actinin aliquot was diluted to 50 mM with Tris-based buffer (4mM Tris-HCl pH 7.6, 4mM NaCl, 20 μM EDTA, 1% (w/v) sucrose, 0.2% (w/v) dextran).

Due to the strongly positively charged silanized mica surface adsorbing F-actins as well as α-actinins, a lipid bilayer surface with a mild positive charge was used. Lipid solution comprised of 30% 1,2-dipalmitoyl-3-trimethylammonium-propane (DPTAP) (890870C, Avanti, USA) and 70% 1,2-dipalmitoyl-sn-glycero-3-phosphocholine (DPPC) (860355C, Avanti, USA) (w/w) was prepared. Each lipid in chloroform was mixed in the glass tube and dried with a nitrogen stream. Then the residual solvent was evaporated by sealing it in a vacuum desiccator for 30 minutes. The lipid was resuspended with pure water and made a concentration of 1 mg/mL. The solution was vortexed and dispersed with a tip-sonicator (NR-50M, Microtec, Japan). The solution was aliquoted and flash-frozen with liquid nitrogen and then stored at -30 °C before use.

For the AFM experiment, DPPC/DPTAP lipid was thawed and diluted with Tris-based buffer (10 mM Tris-HCl, pH 7.5, 150 mM NaCl, 2 mM $CaCl_2$) to 0.1 mg/mL. The solution was then sonicated with an ultrasonic bath (1510-DTH, Branson, Japan) for 10 minutes. The lipid solution of 5 μL was deposited on the freshly cleaved mica at room temperature for 30 minutes. Excessive lipid was flushed off with imidazole buffer. 5 μL F-actin solution described above was deposited on the surface, incubated for 5 minutes and flushed with the same buffer. 5 μL α-actinin solution was then deposited on the surface and incubated for 5 minutes.

Figure 2.16 (b) shows the HS-AFM images taken at 200 ms/frame with a scanning area of 160×140 mm^2 with tip-scan HS-AFM. Though F-actins bridged by α-actinins (indicated by red arrows) were observed at high speed, the dissociation of α-actinins did not happen entirely. As reported in the literature, the binding force between α-

actinin and F-actin was as weak as 18 pN[47] that our observation on the F-actin complex confirmed that the developed tip-scan HS-AFM could be applied to fragile protein complexes without breaking the interaction.

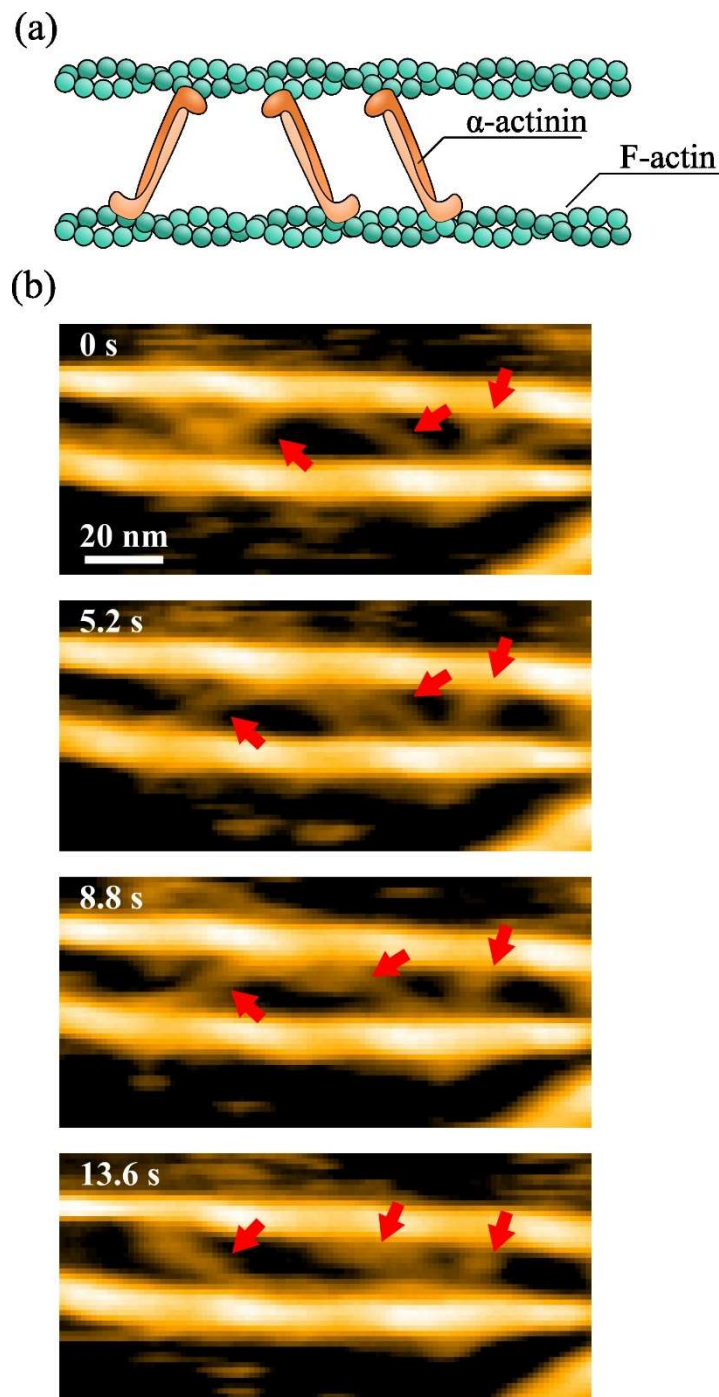
Figure 2.16   F-actin/α-actinin for tip scanner evaluation. (a) Interaction between F-actin and α-actinin. (b) HS-AFM image of F-actin/α-actinin complex. α-actinin is pointed with arrow. Tip-scan mode,160 × 140 mm², 136 × 73 pixels, 0.2 s/frame.

2.5.2 GroEL

The second evaluation was done by imaging the GroEL on the silanized mica surface with the tip-scan HS-AFM. GroEL is a membrane protein of 58 kDa with a hexamer structure. By binding to GroES, the GroEL/ES complex was found to fold the protein correctly. The double layer of the GroEL shown in Figure 2.17(a) is known to be fragile, easily dissected, and recognized as a benchmark for AFM imaging.[49] To perform the imaging, the freshly cleaved mica was treated with 1% APTES solution for 3 minutes to silanize the mica surface and create a positively charged surface for incubating the GroEL. Recombinant GroEL was diluted with the zwitterionic buffer (50 mM HEPES-KOH, pH 6.9, 50 mM KCl, 10 mM $MgCl_2$) to 2 μM and 5 μL of the GroEL solution was incubated on the silanized mica surface for 5 minutes. The zwitterionic buffer was also used as the imaging solution for the AFM.

From Figure 2.17(b), the double layer of the GroEL structure is clearly seen by tip-scan HS-AFM at 500 ms/frame speed. The pore feature of the GroEL is also visible for both layers. Around 7 nm height of the top GroEL was confirmed, as shown in Figure 2.17 (c). Time-lapse images of the GroEL are shown in Figure 2.17 (d). GroEL double-layer structure was observed by the tip-scan HS-AFM for continuous 20 seconds at 500 ms/frame. This result shows that the tip scanner can resolve high resolution off-plane imaging.
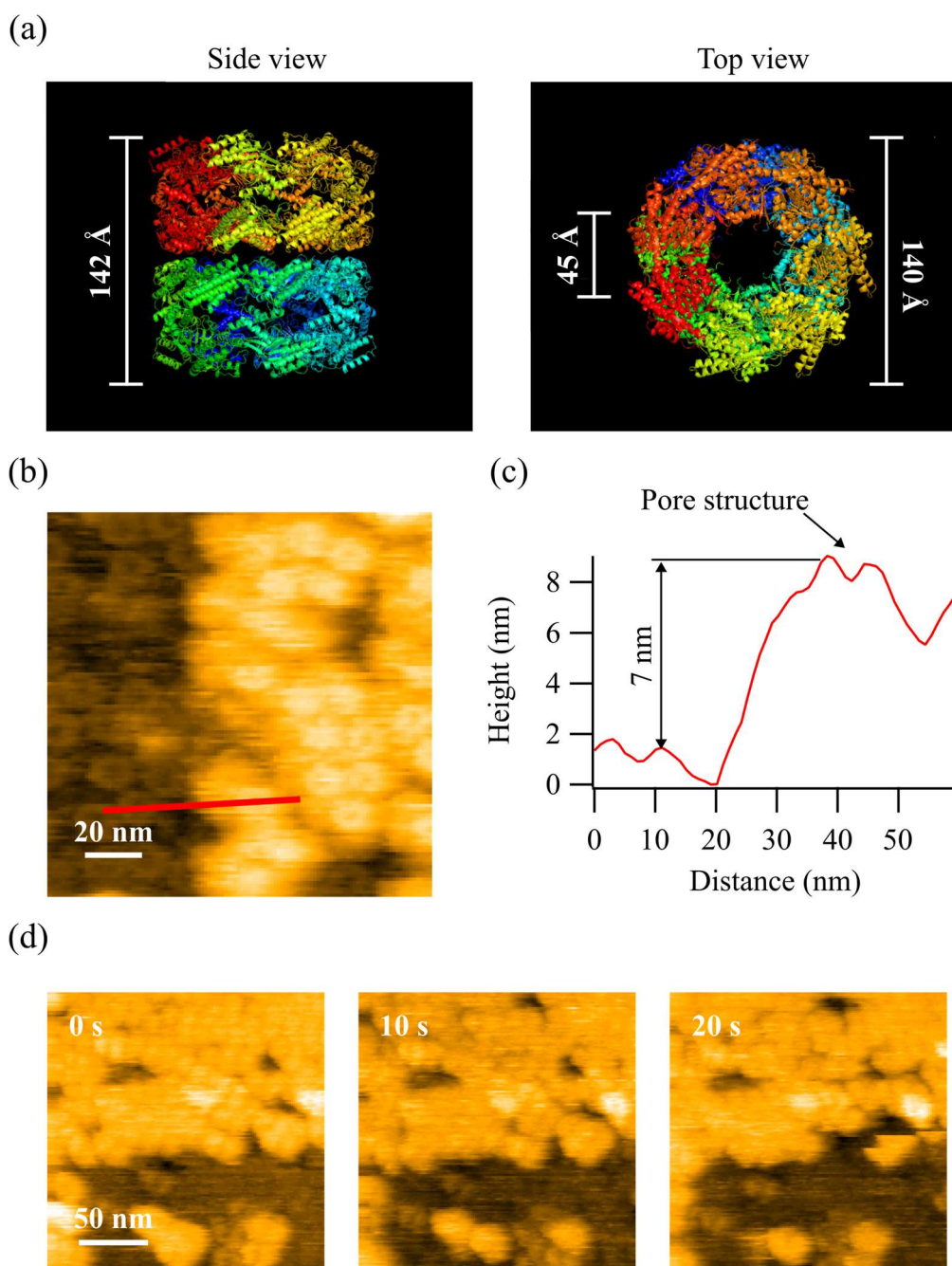
Figure 2.17　GroEL for tip scanner evaluation. (a) Structure of GroEL from side view and top view. PDB: 1KP8. (b) Double layer of GroEL visualized by tip-scan HS-AFM. (c) Line profile on the stacked GroEL. (d) Time lapse images of GroEL shows the structure was maintained during scanning up to 0.2 s/frame within 200 × 200 nm^2 at 120 × 120 pixels.

2.6 Sample Scanner

The development of the tip-scan type HS-AFM is to overcome the disadvantage of the sample-scan type HS-AFM; however, the wide range sample scanner is still a preferred auxiliary function to the tip scanner despites its low scanning speed.

A commercially available sample scanner (SFS-120XY(WA), Sigmakoki, Japan) is installed on a slider structure with four manual micrometer heads (MHN4-25, Mitutoyo, Japan), as shown in Figure 2.18. The maximum displacement of the sample scanner is 120 μm per direction. To further position the sample stage, the micrometer heads were used to locate the sample scanner within a 25×25 mm^2 area at a 10 μm resolution. An opening of the sample scanner can be used to install different mechanisms or simply covered with a lid as a solid support.

The evaluation of the sample scanner was carried out by measuring a test grating (TGQ1, NT-MDT, Russia). SEM image of the TGQ1 grating is shown in Figure 2.19 (a). The square pattern on the TGQ1 has a 3 μm periodicity for both directions for X- and Y-scanner evaluation. Figure 2.19 (b) shows the sample scan image with 10×10 μm^2, 30×30 μm^2, and 80×80 μm^2 with 500×500 pixels at 5 minutes per frame. Measurement accuracy was determined from a 30×30 μm^2 AFM image. In the X direction, a mean periodicity of 3.0 μm with $\sigma = 0.13$ μm was given, whereas Y direction gave a mean periodicity of 3.0 μm and $\sigma = 0.05$ μm (N = 7). Low variance in measurements for each direction indicates the sample scanner is capable of performing reliable measurement or precision positioning.
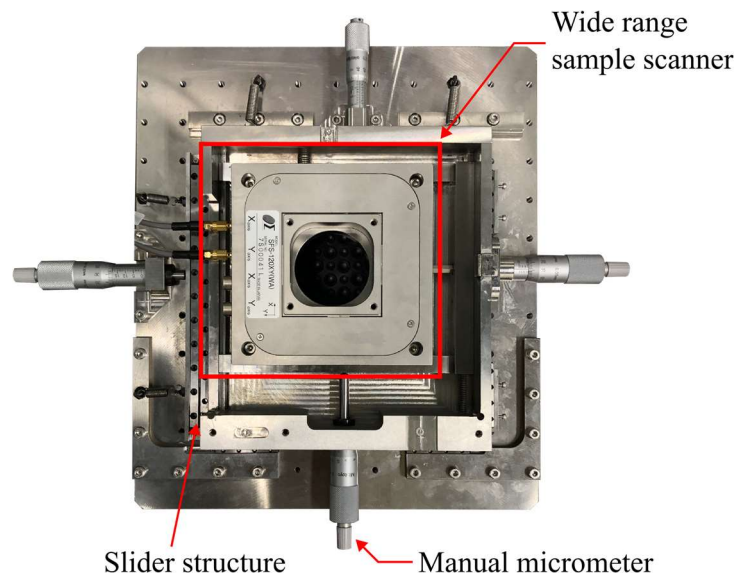
Figure 2.18   Sample scanner assembly for tip-scan HS-AFM.

(a)

(b)
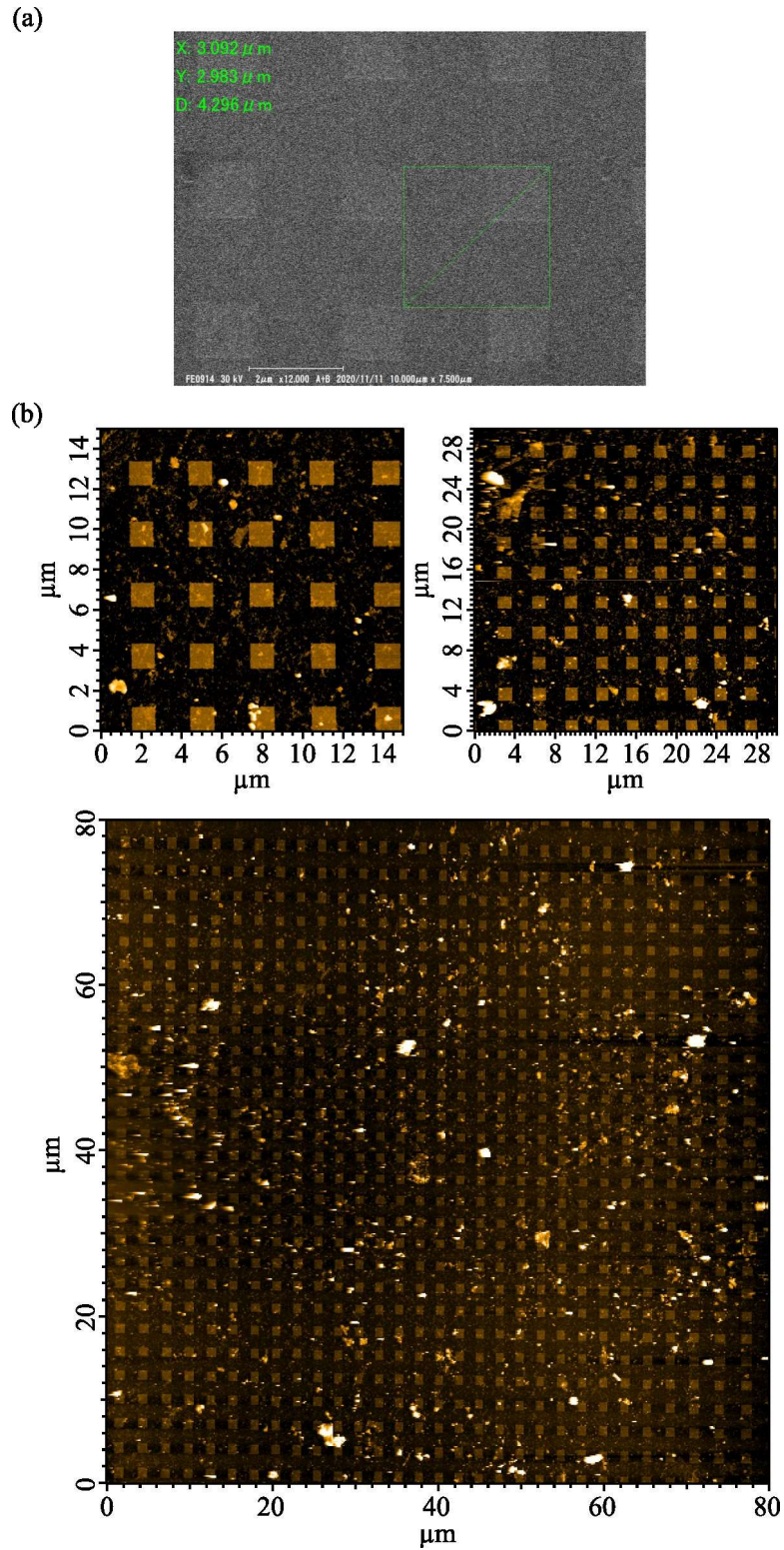
Figure 2.19   Standard grating was used to characterize the performance of sample scanner. (a) SEM image of the used TGQ1 grating. (b) Sample scan AFM images of the TGQ1 grating within 10 × 10, 30 × 30, and 80 × 80 μm². The measurements were performed in the water. Resolution of 500 × 500 pixels for each image.

2.7 Summary

In this chapter, the development of the tip-scan HS-AFM was described. Evaluations of the tip-scan HS-AFM were carried out by HS-AFM imaging on the fragile samples, including the F-actin complex and GroEL. Stable images were given at high imaging speed without deleterious perturbation on the sample. The wide-area sample scanner was compensated and characterized as well. With the sample scanner and tip scanner settled discretely, large-scale imaging and small-scale but high-speed imaging can be chosen depending on the needs. Appended to the instrumentation content, the wax fixation method was verified to have a negligible impact on the tip scanner bandwidth and improve the convenience in HS-AFM operation.

Chapter 3 Development of Stretching Device

3.1 Background

Mechanical stimuli are crucial environmental signals for cells that orchestrate complex cellular processes, including locomotion, proliferation, and morphology. To observe how the biological samples respond to mechanical stress, various studies by optical microscopies have been reported. Stretching experiments on cell,[50] and tissue level[51] were usually accomplished with deformable membrane,[52] microstructure fixation,[53] or optical traps.[54] Because of nanometer scale observation is inaccessible with optical microscopies, yet the sample-scan HS-AFM has the limit in implementing a mechanical manipulator, the tip-scan HS-AFM thereby is provided the opportunity of single-molecule imaging under mechanical stress.

As the finite displacement of the Z-scanner possesses, a smooth solid-supported surface is preferred for HS-AFM imaging. Thus, a stretchable membrane was chosen as the substrate, which defined the design direction as described in this chapter.

3.2 Vacuum Stretching Device

To deform the membrane and apply stress on the cell, a vacuum-actuated stretcher is widely adopted.[53] Figure 3.1 shows a typical design of a vacuum-actuated stretcher which usually consists of a cavity where the air is confined by the deformable membrane and
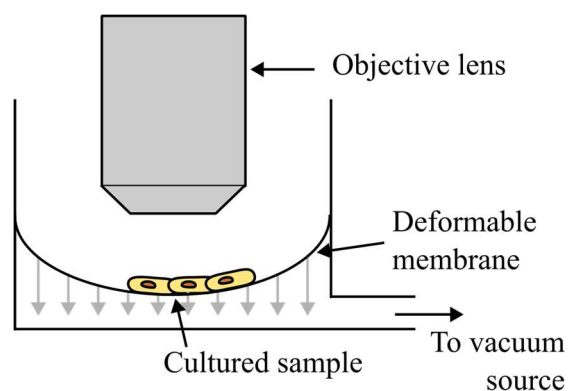

Figure 3.1 Vacuum-actuated stretcher. The deformable membrane is stretched when vacuum source is activated, hence inducing tensile strain on the sample.

static structures. By removing the air with a vacuum source, the atmosphere deforms the membrane, and the tensile strain on the membrane is obtained. Here, the tensile strain is generally estimated from the relative displacement of the illuminative markers.[53] Observation of the sample under tension can be conducted from either side of the membrane.

Considering the AFM imaging is vulnerable to vibration, the membrane must be supported with a solid structure. Thus, a vacuum device for tip-scan HS-AFM was designed, as shown in Figure 3.2 (a) with a cross-sectional view in Figure 3.2 (b). The vacuum device was composed of a silicone membrane, a supporting stage with a sealing O-ring and an air duct, and a membrane retainer to hold the boundary of the membrane on the housing. The air kept between the membrane and housing was removed with a syringe driven by a syringe pump (YSP-201, YMC, USA) via the air duct and the air hose. By exchanging the shape of the supporting stage from circular to rectangular, one can change the strain direction from universal to uniaxial.[55]

Images of devices subjected to vacuum can be seen in Figure 3.2(c). At the center area, a red circular mark was made to indicate the strain when negative pressure was applied. For the universal stretching setup, the circular mark was expanded in the radial direction The area was increased by around 115%, and the center of the area drifted 0.8 mm from the original place. As for the uniaxial stretching setup, the area was only increased by 2% with the major axis extended by 48%. The center mark for the uniaxial stretching setup drifted 0.5 mm after the such strain was applied. Though deformation, as indicated by the red circular mark area change, were verified on both vacuum designs, a drawback should be noted that the strain was not observable without an image-based estimation approach or additional strain sensors during AFM imaging. Thus, the application of the designed vacuum devices was has limited the application, and precise strain control without the image-based estimation approach was still required.

3.3 Unilateral Stretching Device

To eliminate the need for image-based strain characterization, a unilateral stretching device with precise motor control is designed, as shown in Figure 3.3 (a) with cross-sectional view in Figure 3.3 (b). An elastic substrate is fixed with a pair of retainers in which one end remains static as another end is driven. A stepper motor, as the power source, is controlled by customized software that transmits digital pulses to the motor driver circuit and generates 10^{-5} rotation per pulse. The rotational motion of the motor is converted into linear motion with the screw mechanism with 0.5 mm thread pitch,
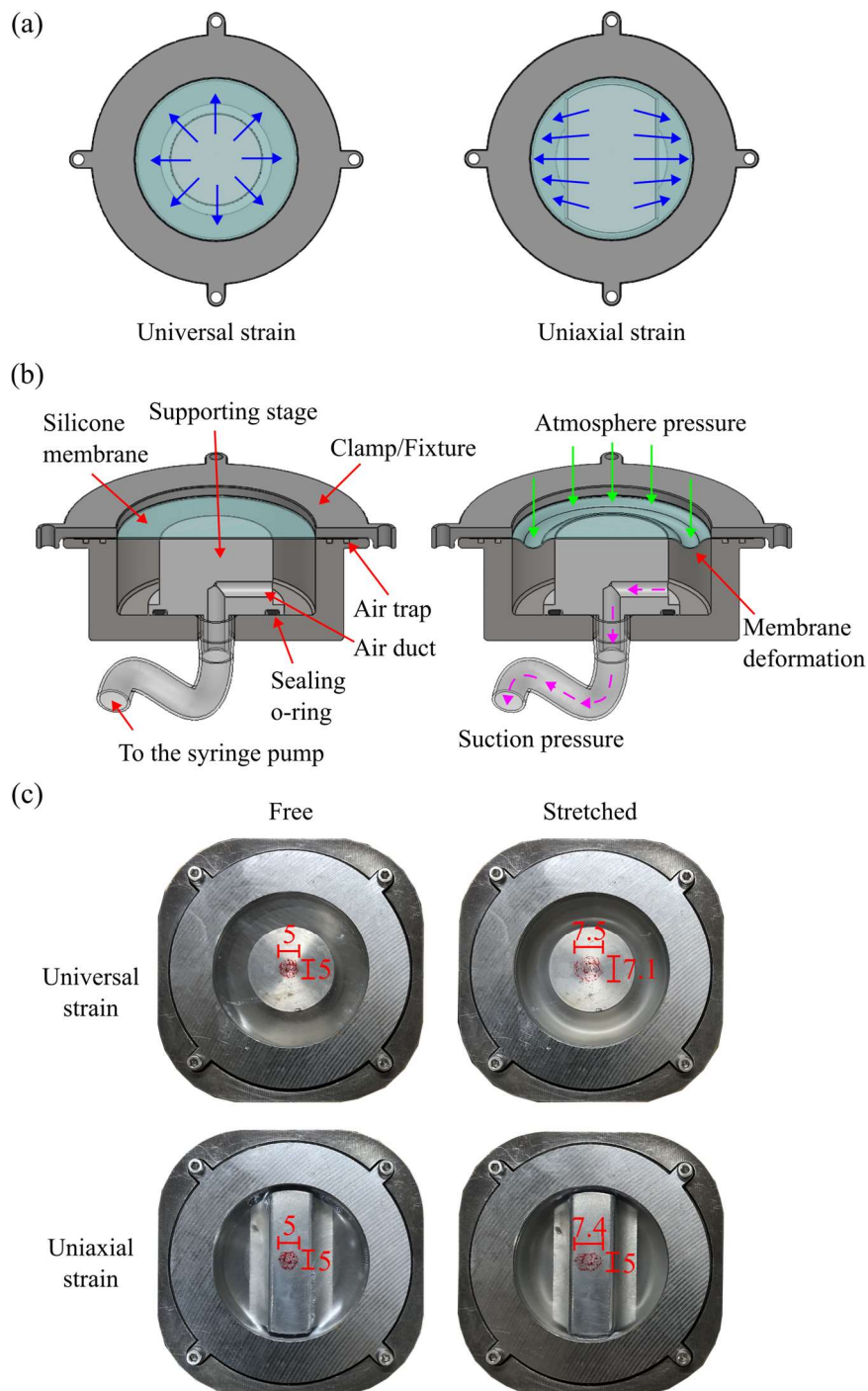
Figure 3.2 Mechanical model of vacuum actuated stretching device. (a) Strain direction can be applied in either universal or uniaxial direction. (b) Cross-sectional view of designed vacuum stretching device (left) and working principle (right). (c) Image of stretching behavior of universal and uniaxial stretching device. Unit: mm.

which results in a 0.5 mm displacement linearly per 10,000 pulses. The screw mechanism then drives the guiding structure linearly. As one of the retainers is fixed on the guiding structure, the elastic substrate is then stretched linearly at a theoretical resolution of 50 nm. A thin layer of grease is applied on the contact surface between the substrate and the stage to eliminate the undesired friction. Considering the minimum distance of 10 mm between the clamps was defined as the initial length, the maximum length of the substrate that could be elongated with this stretching device was 15 mm, or 50% equivalently.
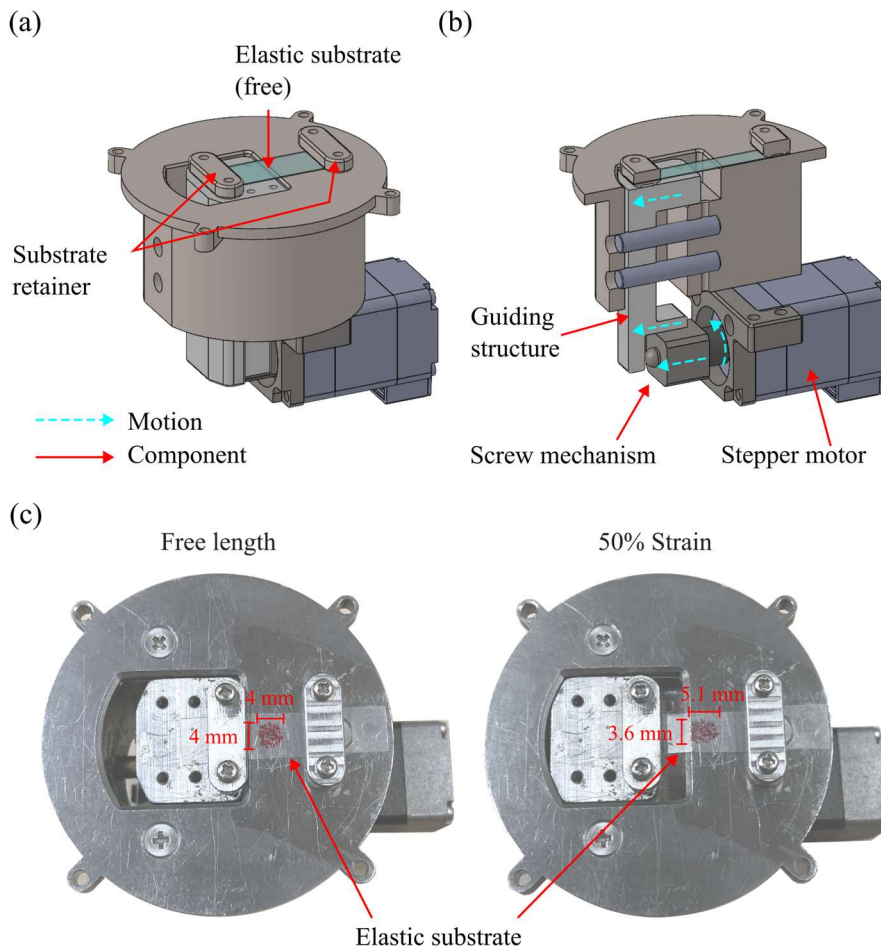
Figure 3.3   Mechanical model of motorized uniaxial stretching device. (a) Rendering image of the device. (b) Cross-sectional view shows the working principle. The stepper motor drives the guiding structure via the screw mechanism. A pair of substrate retainer fix the elastic substrate (blue) where one of the retainers is synchronized with the guiding structure. The substrate is then stretched as motor activated. (c) Image of stretching behavior of motorized uniaxial stretching device up to 50% strain applied. (Strain calculated from the red-painted area.) Unit: mm.

Figure 3.3 (c) shows the silicone substrate was extended from free strain to the maximum stroke of the device. A red mark was painted on the substrate to exemplify the deformation and displacement of the substrate.

After being subjected to 5 mm elongation on the substrate, the marked area was merely increased (~ 1%), in which the major axis was elongated by 13%, and the minor axis was compressed by 9%. The center of the region of interest (ROI) was shifted by 1.4 mm due to stretching. Overall, the unilateral stretching device showed a major improvement in the controllable strain than the vacuum-actuated design. However, the drift distance of ROI when experiencing strain can easily exceed the maximum displacement of the sample scanner. Assuming the scan area is 5 mm apart from the fixed end, 10 % strain will offset the ROI by 500 μm which is four times higher than the sample scanner's operating range.

Thus, the stretching experiments must be limited to a smaller incremental strain so that part of the surface topography will still be covered within the sample scanner range and allows us to zero the offset by micrometer heads manually. For this reason, a bilateral stretching device was designed to tackle the ROI shift problem in the following section.

3.4 Bilateral Stretching Device

The stretching device shown in Figure 3.4 (a) is constructed with three modules: a stepper motor with a screw mechanism, a pair of clips for retaining the elastic substrate, and a support stage for the substrate. The stretching device is then hosted in the wide-area sample scanner, as shown in Figure 3.4 (b). On top of the sample scan stage, the developed tip-scan HS-AFM is settled for scanning [Figure 3.4(c)]. A cross-sectional view of the model is shown in Figure 3.4 (d). The stepper motor connected to the screw mechanism generates linear displacement along the motor shaft axial direction by the same configuration as the unilateral stretching device described before. A pair of transmission shafts are symmetrically fixed on the screw mechanism with one end and with string retainers connected to another end. The traction strings are connected between the clips, which fasten the elastic substrate, and the string retainers. Thus, synchronization between the stretching motion with the screw mechanism is made. String with different materials were tested, including stainless, polymer, and cotton yarn. Cotton yarn-made string is chosen for the traction string as the material is compliant with the device profile yet less elastic under tension. The two clips move uniaxially by following the designed gliding structure and symmetrically to each other.

Of the most concerning issue of lateral displacement from stretching, even tension is

applied from both sides of the substrate as designed here, and the AFM tip is positioned near the center between the clips afterward. Consequently, stretching-induced lateral movement on the ROI is reduced, resulting in more accessible imaging of the same location. The stage underneath the substrate has two functions designed. First, the central region supports the substrate firmly so that substrate vibration is avoided. Second, the glide structure of the stage along the stretching direction constrains the clips during the stretching and allows uniaxial motion only. To reduce the friction between the substrate and stage and further damp the substrate vibration, a thin layer of grease is applied between the substrate and the stage.

The longitudinal strain is derived from the ratio of the increased length to the initial length of the substrate. As mentioned, a linear displacement of 0.5 mm per ten-thousand pulses transmitted will relocate individual clips 0.5 mm synchronously and symmetrically about the substrate center. Consequently, the substrate is elongated by 1 mm and undergoes 10% strain accordingly. The strain of 80% is the maximum strain that can be applied to a 10-mm substrate as designed. Although one can conduct more significant strain by shortening the substrate, the surface buckling resulting from transversal compression by Poisson's effect is generally unappreciated in AFM imaging.[56] Practical consideration of the lateral relocation of the ROI is described here. Consider an image initially taken on a substrate of 10 mm length and defined as ROI, having a 2 mm distance away from the substrate center along the stretching direction. When the substrate experiences 1% strain, the ROI is shifted by 20 μm eventually, which surpasses the operational range of most precision nano-positioner includes the tip scanner configured here. Although imaging at the central region throughout the experiment is agreeable, as no drift of ROI at any strain applied, attempting to encounter the geometrical center position is impractical. As the central region depends on substrate geometry, which varies with different strains, a workaround to this problem is restricting the cumulative elongation of each stretching step. Hence, topographic features are consistently noticeable between stepwise strains. Accordingly, one can approach the region of interest by knowing the shift of features. Thus, with sufficient scanning area of XY-scanner and precision micrometer heads for coarse positioning, performing AFM-based stretching experiments of the same area is possible, as to be shown in the following section.
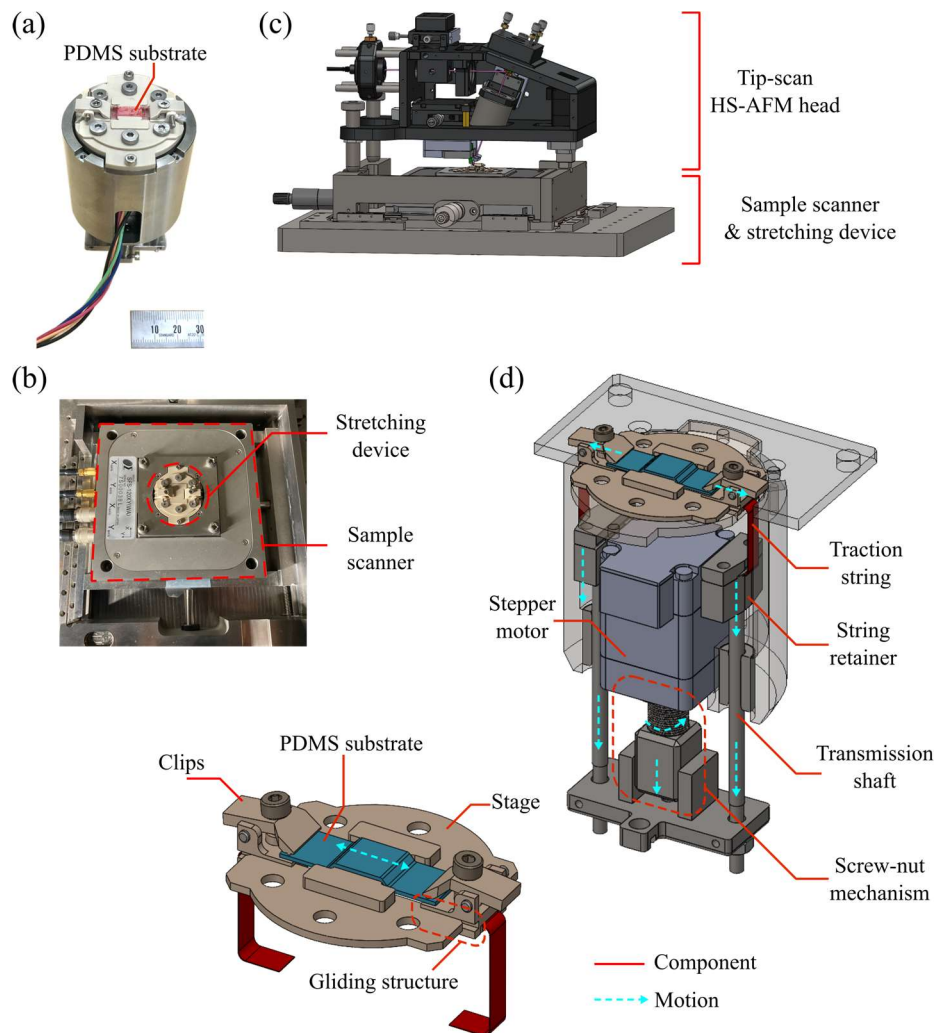
Figure 3.4 Mechanical design of substrate stretcher incorporated in tip-scan HS-AFM. (a) An overview of the stretching device developed. A transparent PDMS substrate is colored in red for better visual contrast. (b) The substrate stretcher is hosted on the wide-range sample scanner. (c) The tip-scan HS-AFM head module is settled on top of the substrate stretcher device. (d) 3D rendering cross-sectional view of rendering model of the stretching device. A pair of clips clamps the elastic substrate (e.g. PDMS) (blue) are relocated synchronously and symmetrically via the traction string (red). Such actuation is powered by the stepper motor via the screw mechanism and transmission shafts.

3.5 Characterization of the Stretching Device

Characterization of the bilateral stretching device was performed with a periodic square patterned polydimethylsiloxane (PDMS) substrate. The local strain was derived from the dimensional variation of the pattern and further quantified the Poisson effect. The preparation of the patterned substrate is illustrated in Figure 3.5. First, the standard grating TGQ1 as a positive mold was immobilized with a drop of glue on a borosilicate glass dish. The silicone elastomer kit was prepared at a 10-to-1 ratio (Sylgard 184, Dow Corning,

Figure 3.5 Negative mold PDMS substrate was prepared for characterizing stretcher device. (a) Preparation of the square patten negative mold PDMS substrate from TGQ1 grating. (b) The expected dimensional change of under tensile stress including longitudinal elongation and Poisson's effect induced transversal compression.

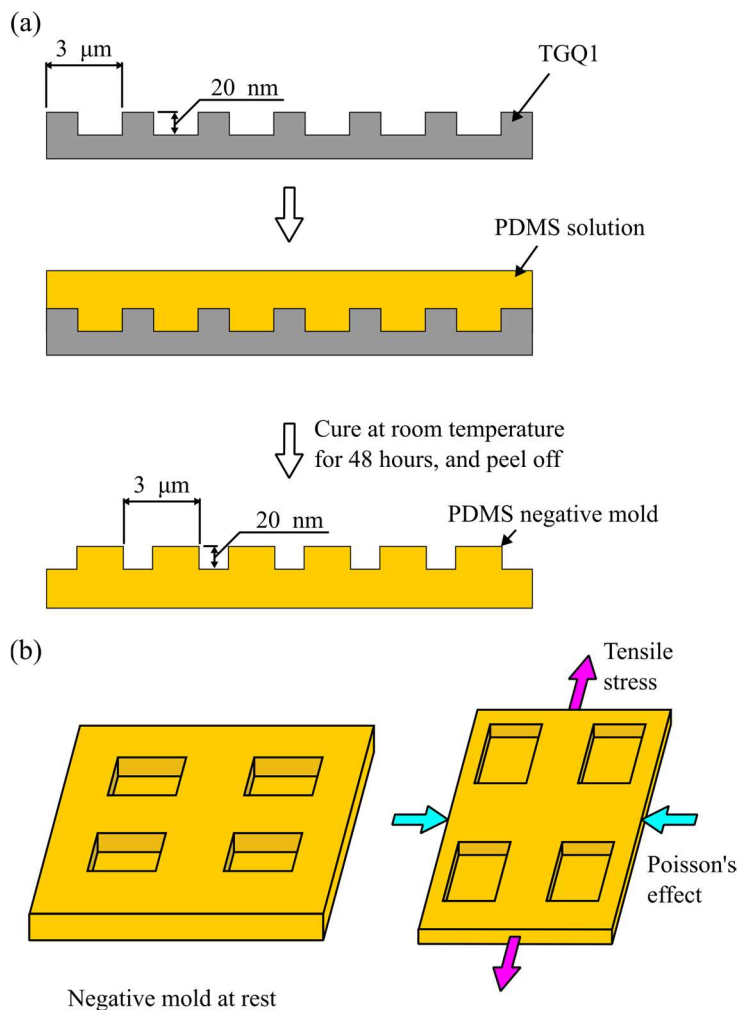Japan) and thoroughly mixed. The elastomer mixture was transferred into the borosilicate glass dish, where TGQ1 grating was immobilized, that the elastomer immersed the grating entirely. Degasification of the uncured elastomer was executed in a vacuum desiccator for 30 minutes to prevent bubbles from the grating patterns. The elastomer was then cured in the laboratory drying oven at 70 °C for 4 hours, followed by slow cooling in the oven for 12 hours. Cured PDMS was picked up deliberately from the glass dish and trimmed to a sheet sized 14×5 mm^2 where the required TGQ1 pattern was situated at the central region. Finally, the patterned PDMS sheet was settled on the sample stage, and the grating region of 5×5 mm^2 was located at the approximate center of the stage. The sheet was clamped with individual clips holding each side and here by having a 10 mm distance between the clips. This distance was defined as the initial length for strain characterization.

Images of the TGQ1 grating pattered PDMS negative mold was taken at equal-
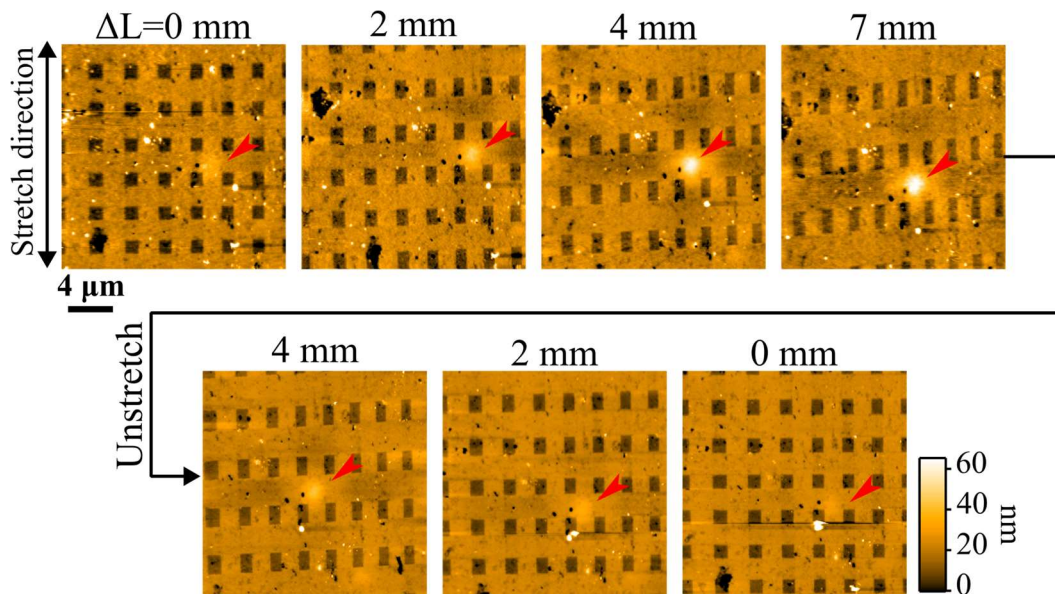
Figure 3.6 Determination of the tensile strain on a micropatterned PDMS substrate. AFM images was taken at successive 1 mm stretching steps by stage scan mode. 20×20 μm^2, 450×450 pixels. The nominal dimensions of the square pattern were determined when unstrained. Stretching was stopped after 7 mm elongation of PDMS substrate was reached. Strain was released afterward and back to 0 mm. AFM images were also taken at the same strain interval to verify the reversible deformation.

spaced elongation and restoration in water at room temperature. Periodicity variation in

square patterns was used to derive local strain in X and Y directions, while strain in Z was estimated from the variation in depth of the square cavity. The substrate was stretched up to 7 mm (0% to 70% global strain) in a step of 1 mm at 10 μm s^{-1}, then reversed with the same step size and stretching speed until the motor step counter returned zero.

The topographies acquired at different elongation conditions are shown in Figure 3.6. The imaging area was approximately retained throughout the stretching and releasing. The square patterns can be seen prolonged along the stretch direction and compressed transversally as the stretching was increased. As the square pattern of TGQ1 has a periodicity of 3 μm in X and Y directions and a height of 20 nm, dimensions of the negative mold of TGQ1 were determined by the tip-scan AFM in sample-scan mode, giving the periodicity of 2.88 ± 0.17 μm in the X direction, 3.03 ± 0.06 μm in the Y direction, and cavity depth of 17.4 ± 0.6 nm in Z direction(mean ± standard deviation, N = 5), respectively. In Figure 3.6, a cupola (indicated by a red arrow) can be seen developing during stretching, and it was well reverted when the elongation was reversed. The reversed topography suggests that the cupola is related to the boundary disturbance exerted by clamping first and propagated to the center area. Further inspection of the cupola with nanoindentation might bring deeper insight but is beyond the scope of this study. It is also obvious from Figure 3.6 that the squares were gradually deformed into rhombi when the longitudinal strain exceeded 40%. However, the square shape was also resumed when the strain was released to 30%. The pattern deformation is caused by the misalignment between the Y-axis of the TGQ1 pattern and the tensile direction.

Dimensional strain ε was calculated by dividing the pattern dimensions after elongation or compression with the initial values. Figure 3.7(a) shows the strains ε_x, ε_y, and ε_z evaluated from the pattern periodicity of X, Y directions and depth of Z directions respecting the elongated length ΔL of the PDMS sheet. 7 mm elongation resulted in the longitudinal strain ε_y of 0.73, and transversal strains ε_x of 0.24 and ε_z of 0.23. After the elongation was reversed, the residual strains for ε_x, ε_y, and ε_z were 0.015, 0.02, and 0.05, respectively. It was found that the stretching motion of the mechanism conveyed a linear variation in longitudinal strain by fitting $\varepsilon_y - \Delta L$ relation with a linear function and a regression coefficient of 0.998 is given. Figure 3.7(b) and (c) plot Poisson's ratios of the pattern ($\nu_{yx} = -\varepsilon_x/\varepsilon_y, \nu_{yz} = -\varepsilon_z/\varepsilon_y$). When the low strain ($\varepsilon_y = 0.1$) was applied, and the Poisson's ratios, ν_{yx} = 0.49 and ν_{yz} = 0.44, concurred with the reported results with bulk material (0.4 ~ 0.5).[57–60] It was also noticed that the Poisson's ratio decreased as ε_y increased and regained as ε_y decreased. The negative correlations between the longitudinal strain ε_y and Poisson's ratio ν_{yx}, ν_{yz} are consistent with previous observations of grid-textured PDMS.[61]

3.6 Summary

In this chapter, feasible stretching methods applied in AFM were reviewed and categorized by the actuating sources and their stretching directions. Applicable devices of each type were constructed and examined accordingly. The bilateral stretching device shows the most advantages and is chosen to integrate into the tip-scan HS-AFM. Characterization of the stretching motion was performed with a negative mold PDMS sheet textured with TGQ1 grating. The dimensions of the square pattern were determined with sample-scan mode imaging, and the local dimensional changes linearly with the applied strain along the tensile direction show the stretching devices is applicable.

Chapter 4 PDMS Surface Treatment

PDMS has become a favorable material for making complex microfluidic cells or sample substrates as it's flexible, easy-processing, optically transparent, and low-cost. However, the hydrophobic nature that originates from the surface methyl group leads to unspecific adsorption and protein denaturation.[62] Considering this drawback, numerous efforts have been devoted to improving the PDMS surface wettability and biomolecule compatibility.[63]

4.1 Ultraviolet-Ozone Treatment

UV-O_3 treatment can oxidize the surface organic group into carbonyl and hydroxyl groups and increases PDMS surface hydrophilicity.[64,65] The oxidation process by UV-O_3 is illustrated in Figure 4.1 (a). First, the atmospheric oxygen O_2 is irradiated with 184.9 nm UV ray and forms O_3; the O_3 is the exposed to 253.7 nm UV ray and decomposed to strong oxidizing atomic oxygen O. On the other hand, the organic compounds absorb the energy from the UV rays, and chemical bonds with energy below the UV rays will be decomposed. Consequently, these activated or the free radicals of the organic compounds react with the atomic oxygen to form simple molecules, such as CO_2, H_2O, and O_2, which are then removed from the surface. The oxidized surface forms a thin layer of the silica-like surface, and the heterogeneous stiffness on the surface is prone to surface buckling when subjected to load.[66] To characterize the surface buckling topography with respect to tensile strain, hence exploiting the buckling topography, UV-O_3 treated PDMS surface was stretched and scanned with tip-scan HS-AFM. A UV-O_3 cleaner (UV-O_3 cleaner, Ossila, UK), shown in Figure 4.1 (b), was used to carry out the surface oxidation process. First, a PDMS sheet was treated with UV-O_3 cleaner for 1 hour, then clamped on the stretching device with an initial length of 9 mm. The stretching motion was actuated at a speed of 10 $\mu m \cdot s^{-1}$ at successive ~10 % strain with the stretching device. Images were taken by tip-scan mode with 1×1 μm^2, 200×200 pixels, 0.2 s/frame , as shown in Figure 4.2 (a)

Tensile stress along the Y axis was accompanied by compressive stress due to Poisson's effect and led to surface buckling as early as the 11% strain applied with an average peak-to-peak height (H_{p-p}) of 3 nm and a wavelength of about 50 nm as the highest value throughout the experiment. The horizontal boundaries were found when the strain was applied. These boundaries were the breakage of the oxidized layer PDMS due

to the tensile load exceeding the tensile strength of the layer. As the strain increased to 30%, the H_{p-p} reached 7.6 nm as the maximum, with a wavelength of 42 nm. It's found that H_{p-p} did not grow monotonically with the loading but saturated to ~ 7 nm until 55%.Wavelength continuously declined and reached 36 nm as the strain increased up to 60%, whereas the H_{p-p} decreased to 5.6 nm. By taking a horizontal line profile on the 60% strain surface, a higher-wavelength ripple of ~ 500 nm was formed, as plotted in Figure 4.2 (c). The formation of the secondary ripple originated from the higher-mode buckling. Due to first ripple structure was compressed and saturated, indicated by the declining wavelength and comparatively stalled growth of the H_{p-p} , the closely packed ripple formed a layer equivalent to a thicker one and higher-mode buckling was triggered by the increasing load.[67,68] However, a zoom-out tip-scan or sample-scan image was not available due to the higher-mode buckling generated ripple structure that exceeded the maximum stroke (~ 2 μm) of the Z piezostack implemented on the tip scanner.
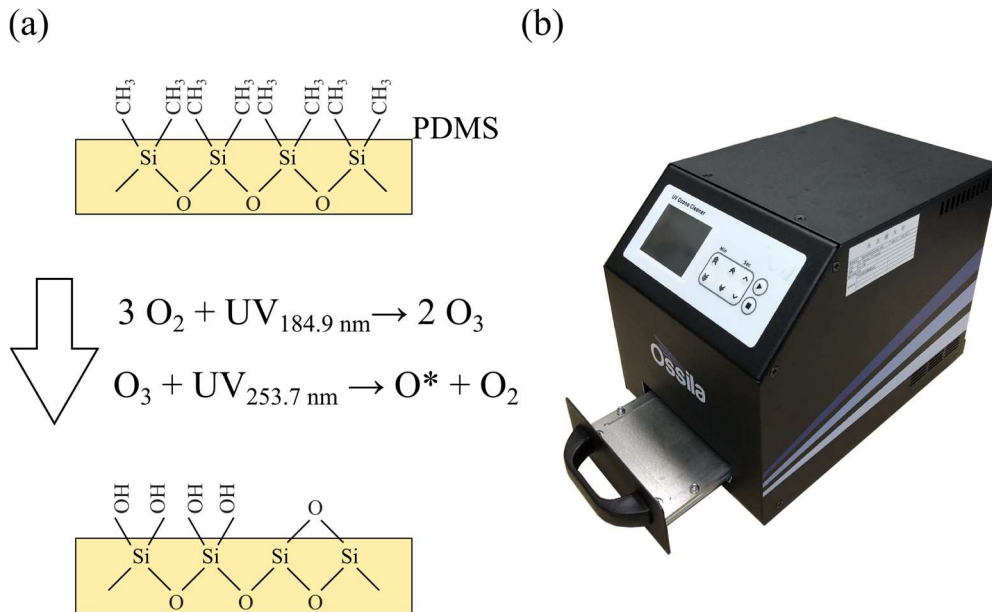
Figure 4.1   PDMS surface treatment with UV-O₃. (a) Methyl group is oxidized with UV induced atomic oxygen. (b) UV-O₃ cleaner used for surface oxidation (UV-O₃ cleaner, Ossila, UK).
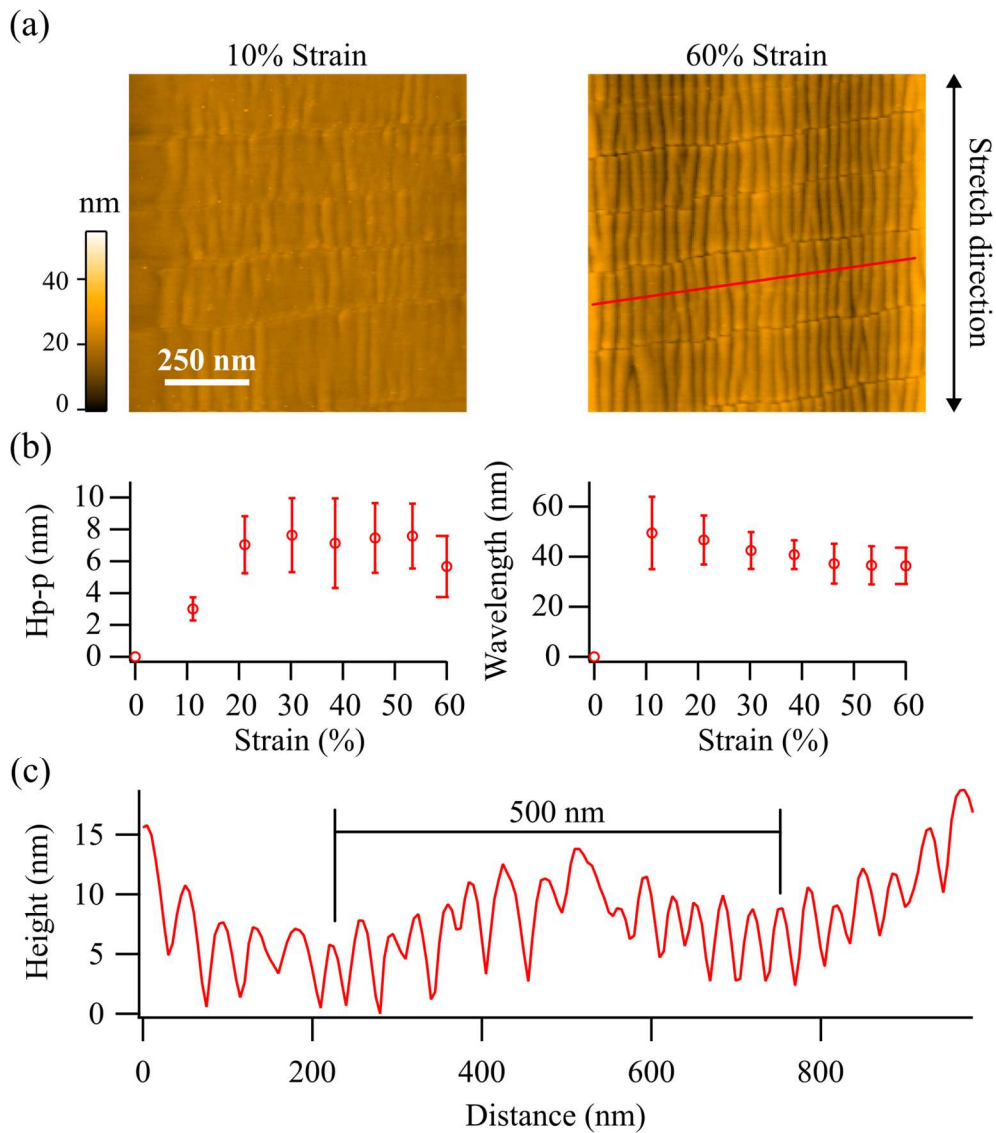
Figure 4.2 Determination of PDMS surface treatment with UV-O$_3$. (a) Surface buckling was observed with sample scan mode in the liquid. Ripple structure was controlled by different strain applied up to 60%. Horizontal breakage was found at all strain larger than zero. Tip-scan mode, 1×1 μm^2, 200×200 pixels, 1 frame/s. (b) The peak-to-peak of height, H$_{p-p}$, and wavelength of rippled surfaces were observed as function of applied strains. (c) Higher-mode buckling observed when 60% strain applied.

4.2 Ion Bombardment

Other than UV-O$_3$ treatment, the surface can be oxidized by ion bombardment as well.[69] The plasma excites gas atoms into higher energy states and ionizes the gas atoms. The mixture of the plasma then breaks the surficial methyl group of PDMS and forms carbonyl, and hydroxyl groups, as illustrated in Figure 4.3 (a). To characterize the oxidized surface properties, a plasma ion bombardment device (PIB-10, Vacuum Device, Japan, [Figure 4.3 (b)]) was used to modify the PDMS surface, and surface topography of plasma-treated PDMS was evaluated at various strain conditions. PDMS sheet was first treated by ion bombardment for 5 seconds and clamped on the sample stage with the unstrained initial length of 10 mm. Stretching was applied at 10 μm·s^{-1} along the Y axis and strain-

(a)　　　　　　　　　　　　　(b)

Figure 4.3　PDMS surface treatment with ion bombardment. (a) Methyl groups are oxidized with plasma induced atomic oxygen. (b) Ion-bombardment device used for surface oxidation (PIB-10, Vacuum Device, Japan).
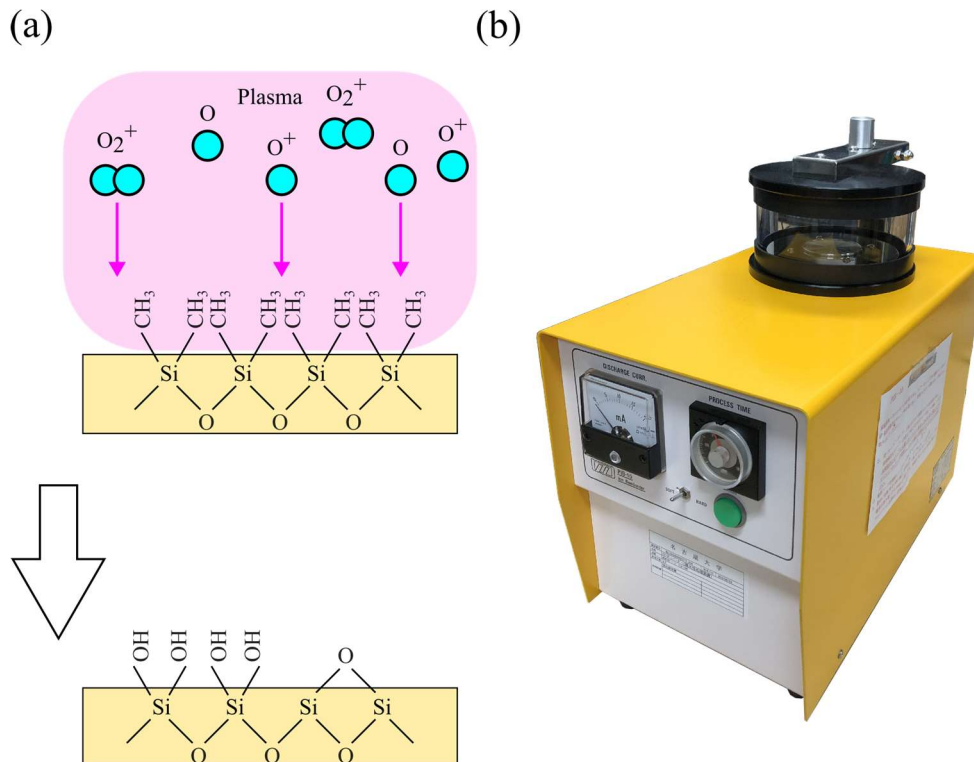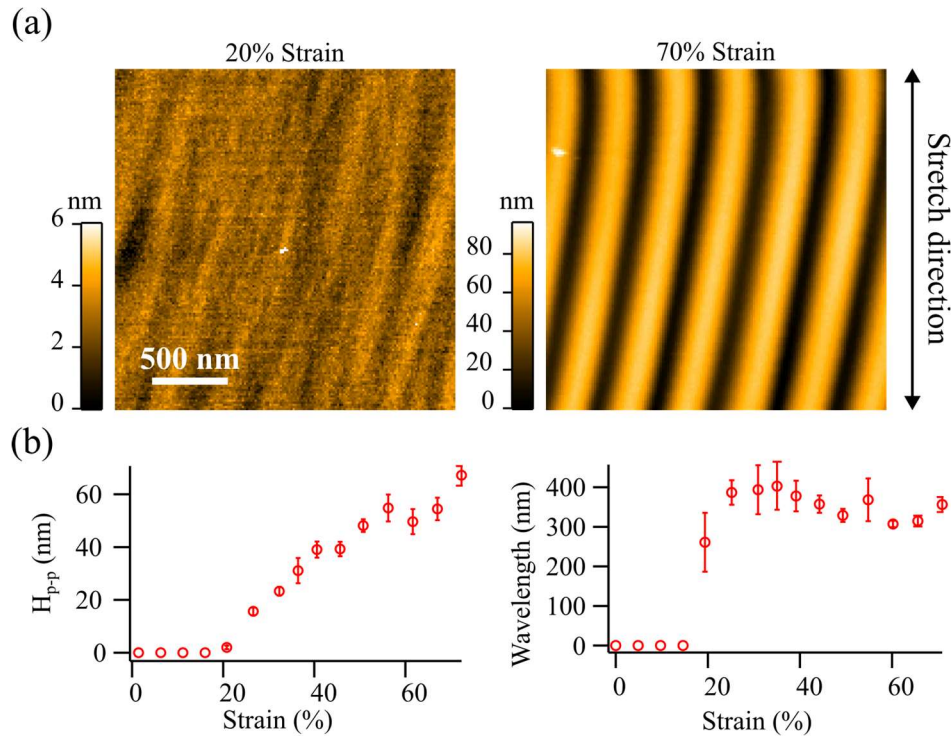
Figure 4.4 PDMS surface treatment by plasma ion-bombardment. (a) The topography of the surface ripples can be regulated by the strain applied to the PDMS substrate. (b) The peak-to-peak of height, H_{p-p}, and (c) wavelength of rippled surfaces were measured as function of applied substrate strains.

dependent topography of the PDMS surface was imaged at successive 5 % strain by sample-scan mode with 2×2 μm^2, 135×135 pixels, as shown in Figure 4.4 (a). As can be seen, the ripple structure was formed along the X direction due to surface buckling. A rotational angle of the ripple with respect to the stretch direction was found and was increased as the applied strain increased. It's believed the rotation originated from imperfect alignment between the substrate's longitudinal axis with the stretch direction and is considered the same reason for the square pattern of negative mold TGQ1 transformed between square and rhombic shapes. The development of the ripple properties with applied strain is depicted in Figure 4.4 (b). Ripple with a wavelength of 250 nm and average peak-to-peak height (H_{p-p}) of 2 nm showed up when the strain was applied up to 20%. H_{p-p} of strain below 20% was not discernible and increased as the strain increased up to 67 nm when 70% strain was applied. The wavelength of the ripples first rapidly reached 402 nm at 35% strain and declined to 307 nm at 60% before slightly

rising again to 356 nm at 70%. The inclining trend of the ripple wavelength could be considered as the inhomogeneous occurrence[70] of surface buckling as evidenced by the largest standard deviation in wavelength (74 nm). The wavelength deviation converged gradually as the strain increased basically. Furthermore, surface breakage along the transversal direction was found, as shown in Figure 4.5, suggested the tensile load exceeded the tensile strength of the oxidized PDMS layer.

Compared to the UV-O$_3$ treatment, surface buckling in a higher-mode was not found in the plasma-treated PDMS surface. A possible reason for the secondary buckling not being detected is that the first-mode ripple structure was not saturated, thus lacking an effective thicker layer for further buckling, as evident with the H$_{p-p}$ increasing with applied strain and showing no the tendency of saturation until 60% strain. Wavelength development of the two treatments indicates that the ion-bombardment method converted the soft PDMS surface into a thicker silica-like layer than the UV-O$_3$ treatment. The current setup could not resolve treatment conditions that create equivalent surface properties with both methods; however, both observations show the ripple structure is controllable and that the stretching platform can be used for studying topographic-dependent properties.
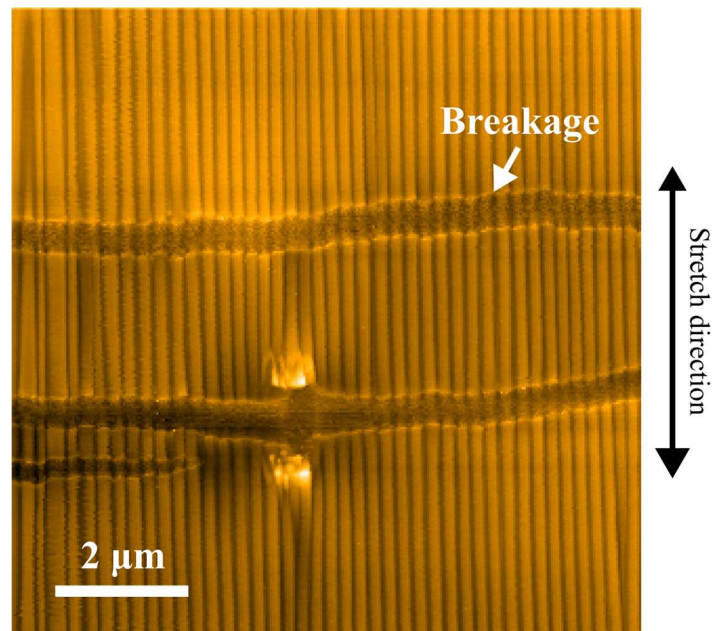
Figure 4.5 Cracked perpendicular to the stretch direction on Plasma-treated PDMS surface at 60% strain. Sample-scan mode, $10 \times 10 \ \mu m^2$, 400×400 pixels.

4.3 Surface Amination

Though surface treatment by oxidation reaction can be processed in a few seconds and allows a hydrophilic layer, surface buckling eventually happens to the PDMS substrate when a compressive load is gradually increased. The amplitude and periodicity of the buckling pattern depend on the load, the stiffness of the oxidized layer that the amplitude of the wrinkle would reach hundreds of nanometers in the case of a plasma-treated surface.
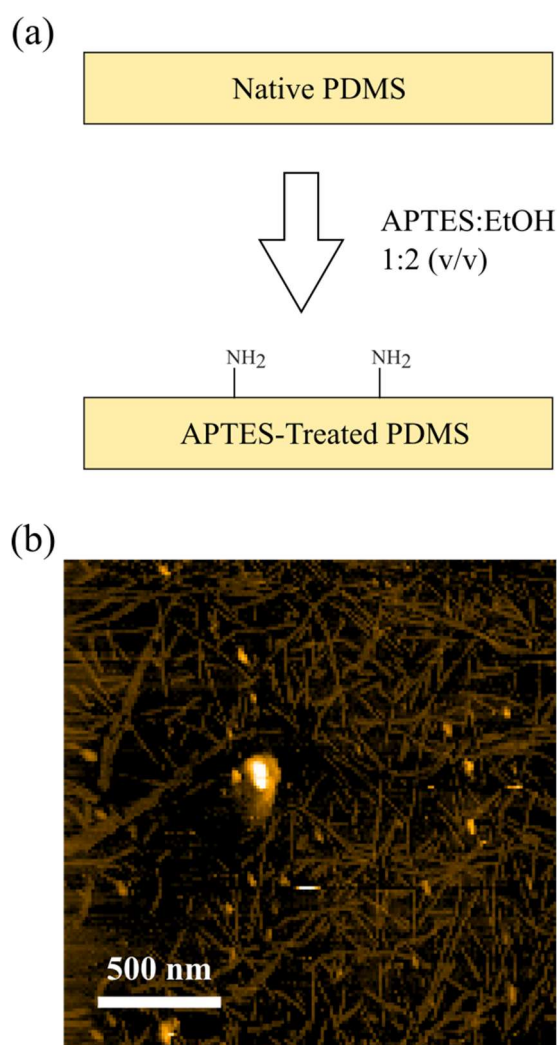
Figure 4.6   PDMS surface treated with APTES. (a) Amine group is introduced to the PDMS surface by PDMS swelling. (b) F-actin fixed on the treated PDMS surface. Sample scan, 2×2 μm^2, 150×150 pixels.

As a result, the imaging becomes difficult due to limited Z-scanner stroke and scanning parachuting.[33] Therefore, surface treatment without inducing surface stiffening is demanded. Here, a surface modification on the PDMS substrate reported by Beal et al.[71] is demonstrated.

Normally, the tendency of PDMS swells organic solvent is considered undesirable[72] because the uncured elastomer oligomer extracted from the bulk material may interfere with the biological applications.[73] However, the swelling property can be used to uptake alkoxysilanes, such as APTES, into PDMS.[74] The modification is described below with an illustration in Figure 4.6(a). The PDMS surface was immersed in the 33% APTES ethanolic solution for 5 minutes. Dilution of the APTES is to prevent precipitate formation. The surface is then drained with a laboratory wipe and immersed in the 33% (w/v) aqueous acetic acid (011-00276, Fujifilm Wako, Japan) to catalyze the ATPES, then rinsed with pure water to remove the residue catalyst solution. The PDMS surface functionalized with APTES improved the surface charge property that can be used to adbsorb negatively charged proteins or particles.[75] As an example, the F-actin solution was deposited on the APTES-treated surface and incubated for 5 minutes. The excessive solution was then flushed away with imidazole buffer and imaged by tip-scan mode. As shown in Figure 4.6 (b), the PDMS surface treated with APTES can adsorb F-actin, while no F-actin was found on the pristine PDMS surface with the same incubation concentration and time as a negative control experiment.

4.4 Biotinylation

Although physisorption can immobilize target molecules on the substrate surface, the binding energy of physisorption and the orientation of target molecules are often perturbed by surface conditions. Therefore, specific adsorption methods, such as linker connection or antibody, are implemented for better binding controllability.[76] One of the widely used techniques is the streptavidin-biotin binding method. Streptavidin, a tetrameric protein from the bacterium *Streptomyces avidinii* has a molecular of around 60 kDa. Streptavidin-biotin binding is known to have a strong non-covalent interaction in nature with $K_d \sim 10^{-14}$ M. Because the binding is stable over a wide range of pH[77] and temperature,[78] streptavidin-biotin complexes are widely used for labeling and immobilization.[79] One of the biotinylation methods is using an amine-reactive agent to connect biotin to the target molecules. The N-hydroxysuccinimide (NHS) ester is a commercial biotinylation reagent that covalently links the amine group of protein to biotin. The surface biotinylation is described here. Biotin-(AC5)$_2$-OSu (B306, Dojindo, Japan)

was diluted by dimethyl sulfoxide (DMSO) (034-07216, Fujifilm Wako, Japan) to 170 µM and incubated on the APTES processed surface for 10 minutes and rinsed by pure water. Streptavidin solution at 50 nM was reconstituted from powder (9013-20-1, Sigma Aldrich, Japan) with pure water and incubated on the biotinylated PDMS surface for 10 minutes. The excessive solution was drained with a laboratory wipe, and the surface was rinsed with pure water. G-actin was modified with Biotin-(AC5)$_2$-OSu at a molar ratio of 1:99. Polymerization of the biotin F-actin from the biotinylated G-actin was performed by the procedure as same as unmodified F-actin in instrument characterization section. 5 µM of the biotinylated F-actin solution was incubated on the streptavidin-covered surface for 15 minutes and rinsed with imidazole buffer to remove excessive protein. The scheme of the fixation is depicted in Figure 4.7 (a).

AFM image of biotinylated F-actin fixed on the elastic substrate is shown in Figure 4.7 (b). Unmodified F-actin was incubated on the surface with the same preparation as a control group, and resulted in no adsorption of F-actin was observed [Figure 4.7 (c)].
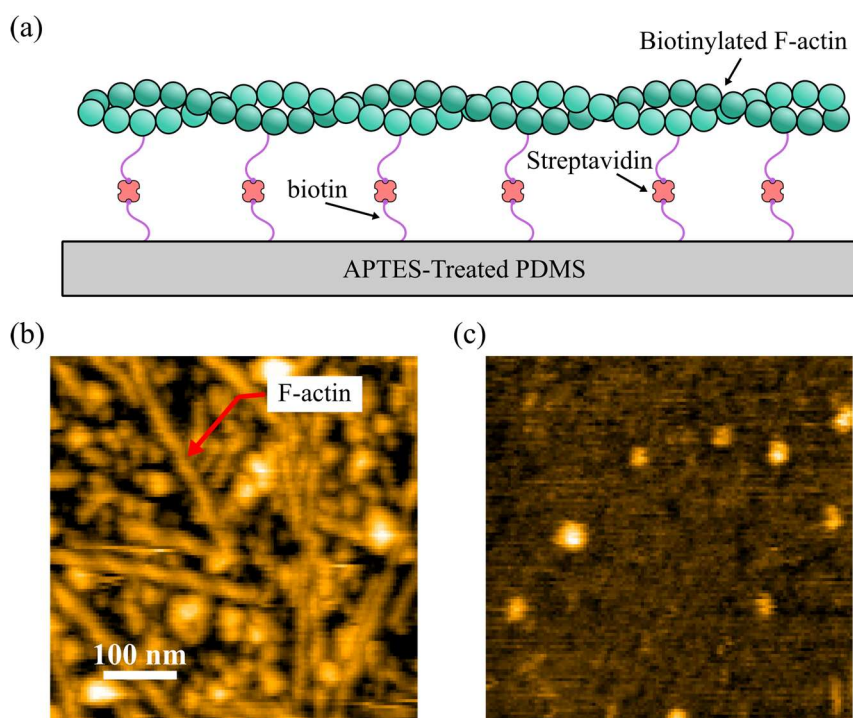
Figure 4.7 PDMS surface modification with biotin/streptavidin pattern. (a) Exemplar application of the biotin/streptavidin method on PDMS to incubate F-actin. (b) F-actin was fixed on the biotin modified surface. (c) Unmodified F-actin was not found on biotin modified surface. Tip-scan mode, 500×500 nm^2, 150×150 pixels, 1 s/frame.

4.5 Motor Protein Anchor

Other than biotin functionalization, the nonspecific adsorption propensity of the PDMS surface was applied to create a layer of motor protein anchor, kinesins, and retain the target protein, microtubules.[80] Microtubules are the stiffest protein polymer in the cytoskeleton of eukaryotic cells. Kinesins are microtubule-dependent motor proteins that participate the mitosis, meiosis, and cellular cargo transportation. The binding strength between the kinesin and microtubule is weaker than tubulin-tubulin binding,[81] therefore, when the microtubule experiences relative displacement to the kinesin, microtubule will be detached from the kinesin anchor.

The preparation of the microtubules is described as follows. 50 μL of frozen tubulin at 6 mg/mL purified from the porcine brain was thawed. Guanosine-5'-triphosphate (GTP)

Figure 4.8   PDMS surface coated with kinesin for fixing microtubule. (a) Illustration of the kinesin fixation. (b) AFM image of microtubule fixed on the PDMS substrate via kinesin. Sample-scan mode, 5×5 μm^2, 200×200 pixels.

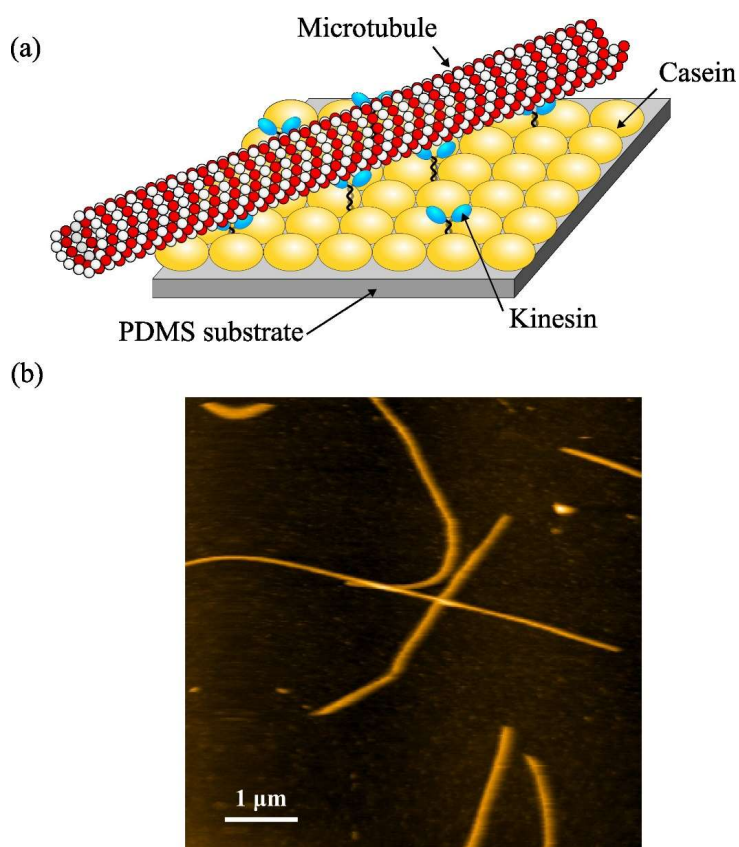and paclitaxel were added to the tubulin solution to make the concentrations of 1 mM and 40 μM, respectively. The centrifuge tube with the mixture was transferred to the ice box (0 °C) for 5 minutes to incubate microtubule seeds. The tube was incubated in the dry incubator at 37 °C for 30 minutes to promote polymerization. In a centrifuge tube, cushion buffer was prepared by mixing 40% glycerol in the BRB80 buffer (80 mM PIPES pH 6.9, 1 mM MgCl$_2$, 1 mM EGTA) containing 1 mM GTP and 40 μM paclitaxel at final concentrations. The polymerized solution was carefully moved to the top layer of the cushion buffer and loaded into the ultracentrifuge to be pelleted at 58000 rpm and 37 °C for 40 minutes. The supernatant was discarded, and the pellet was resuspended by 80 μM BRB80 buffer containing 1 mM GTP and 40 μM paclitaxel. PDMS surface with kinesin anchor was prepared with new PDMS substrate and kinesin-1/BRB80/casein solution. The casein in the solution acts as the surface passivation and kinesin supporter. Without the casein, the kinesin will be denatured on the PDMS surface[62] and incapable of attaching to microtubules.[80] First, casein powder was dissolved in BRB80 to make a concentration of 0.2 mg/mL. Recombinant kinesin-1 consisting of the first 573 amino acids was added to the BRB80-casein solution and diluted to 100 nM. The kinesin solution was then incubated on the pristine PDMS substrate for 20 minutes. After coating the kinesin on the PDMS, followed by BRB80-casein solution rinsing, the microtubule solution was incubated on the surface for 30 minutes. Excessive microtubule solution was rinsed with BRB80 containing 20 μM paclitaxel. Figure 4.8 (a) depicts the fixation scheme via the kinesin motor. AFM image, as shown in Figure 4.8 (b), was acquired by sample-scan mode of AFM at 5×5 μm^2, 200×200 pixels, as proof that the anchor method is applicable. Different methods were reported for fixing microtubules on the elastic substrate. However, the method demonstrated here require neither PDMS oxidation before the casein/kinesin deposition, nor the using streptavidin to fix the biotinylated kinesin.[82] Therefore, the demonstrated method is a convenient alternative to the other kinesin fixing methods.

4.6 Summary

PDMS substrate is widely used for its convenience in preparation, mechanically flexible toughness, and robustness. However, the hydrophobicity nature of PDMS hindered the application in the biological application. Five surface treatment methods on the PDMS surface were described in this chapter. Oxidation methods, like UV-O$_3$ or ion bombardment, created a stiff layer on the PDMS surface. Such stiff layer can be used to create a curvature-controllable topography by surface buckling with the stretching device. As for the non-oxidation modification, surface charge polarity modification with APTES, surface biotinylation with the biotin reagent, and motor protein grafting on native PDMS were separately demonstrated as well. Therefore, a stretching device combined with proper surface treatment allows for the manipulation of the topographical environment and investigation of accompanied phenomena.

Chapter 5 Application

5.1 Observation of Microtubule Bending

5.1.1 Background

Mechanical signal, such as stress and geometry, is important to regulate cellular function. Various proteins were found to react to the environmental stimulation as a sensor, a transducer, or an actuator. Microtubule in the cytoskeleton was regarded as having a structural role and organizing the cell morphology,[83] and a sensor for abiotic stimuli.[84] Of one the stimuli of mechanical stress, microtubule dynamics under bending attract widespread attentions.[85] Thus, bending and buckling experiments were reported with various techniques, including axonemes fixation with optical tweezer[86] and hydrodynamic deformation,[87] biotin/streptavidin fixation,[88] pinning by lipid defects,[30] and kinesin anchors on PDMS surface.[89] However, the observation at a single-molecule resolution scale with real-time stress-controllable stimulation is still lacking. Therefore, the bending experiment with stretched-combined tips-scan HS-AFM is conducted.

5.1.2 Materials and Experiment Setup

A pristine PDMS substrate with a size of 14×5 mm^2 was clamped on the stretching device with an initial length of 10 mm defined by the distance between clips. The PDMS was further elongated to a length of 15 mm. Microtubules were polymerized and incubated on the kinesin-covered PDMS substrate prepared as described in Chapter 4.5. The elongated substrate was slowly released by the bilateral stretching device with a step of 0.25 mm, which is 1.6% strain approximately, at a speed of 25 $\mu m \cdot s^{-1}$. Figure 5.1 illustrates the bending assay of microtubules on the PDMS surface. Images were acquired by sample-scan mode at each releasing step.

5.1.3 Experimental Result

Microtubules anchored on the PDMS substrate via kinesin were observed by sample-scan
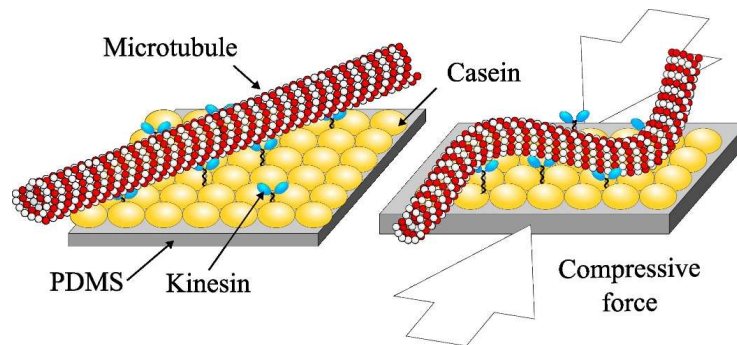
Figure 5.1 Microtubule bending assay. Microtubule was first fixed on the kinesin coated PDMS substrate and bent by the compressive load via the kinesin anchors on the substrate.

mode of AFM, with a large scanning area of $30 \times 30 \ \mu m^2$ at 400×400 pixels shown in Figure 5.2 (a). Two cupolas, marked with cyan circles, were exploited to relocate the sample stage, and retain the imaging area. Magnified scanning area images of $10 \times 10 \ \mu m^2$ with 300×300 pixels were taken to observe the microtubules at different strains. As can be seen in the images, the population of microtubules on the substrate was reduced after the compression (13.3%). A possible explanation is described as follows. When the microtubule experienced buckling, the microtubule was bent from straight to curved conformation that detached from the kinesin anchor points, but there were not enough anchor points available to firmly fix the microtubule at its new shape, resulting in an elevated force on the remaining kinesins that the microtubule entirely detached from the kinesin eventually. In addition to microtubule detachment, the compressive stress may have promoted microtubule depolymerization locally and resulted in fragmented microtubules on the surface after compression.

The progressive bending of a single microtubule situated in the red solid-line rectangular in Figure 5.2 (a) of $10 \times 10 \ \mu m^2$ is magnified in Figure 5.2 (b). The microtubule at its initial state was slightly curved and further bent even at 1.65% compression applied, and the bending radius decreased as the compressive strain increased. At 3.3% strain, the bending radius was estimated to be 2000 nm by fitting a circle to the microtubule's shape. The bending radius gradually decreased as the strain increased that reached 740 nm at 10% strain. When the compressive strain of 11.7% was applied, the local deformations due to compression led the microtubule to kink and break. The microtubule underwent depolymerization, and the fracture was further developed at

59

13% strain that the microtubule became discrete segments.

The bending radius of the microtubule was plotted in Figure 5.2 (c), which shows the curvature-controllability of the microtubules with the stretching device.[90] The microtubule bending assay can be further applied to curvature-regulated affinity with microtubule-associated proteins by HS-AFM imaging, as well as curvature-dependent mechanical characteristics[30] with nanomechanical measurements, is anticipated.
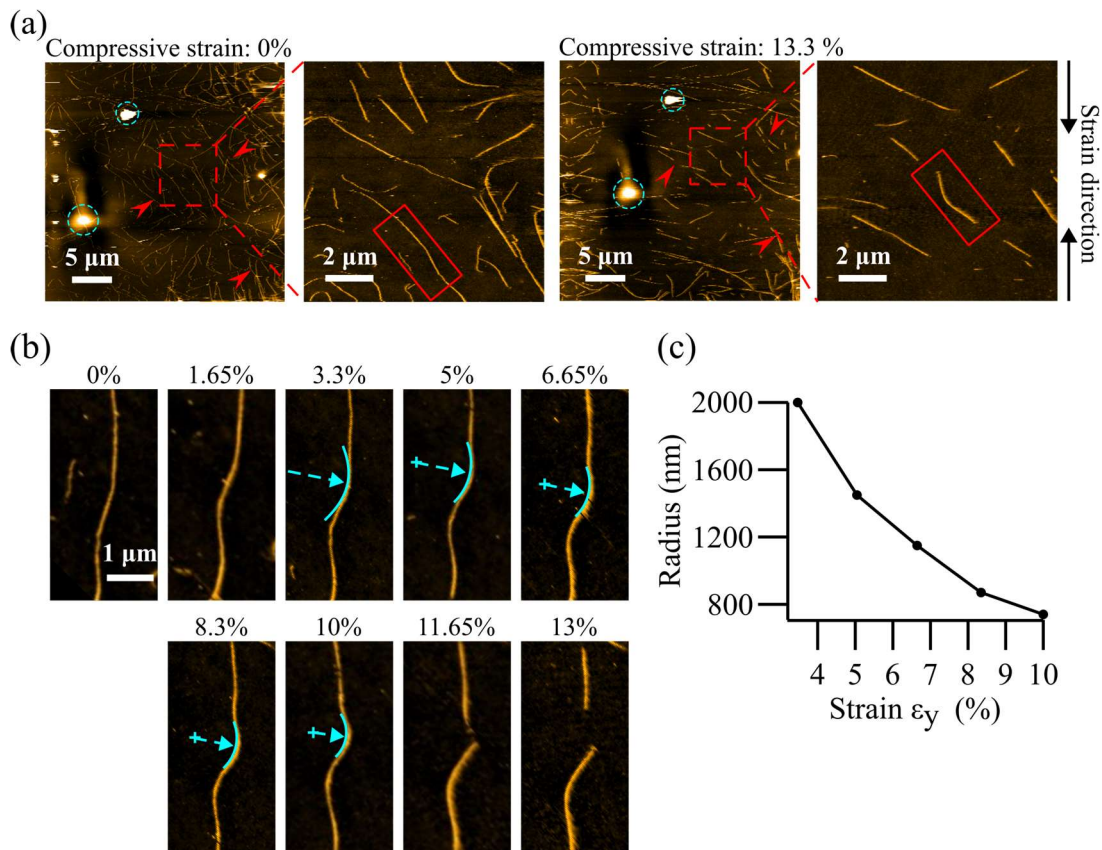
Figure 5.2   Buckling of microtubules induced by compression of PDMS substrate. (a) Wide-area AFM images taken by the sample-scan mode before and after the PDMS substrate compression. 30×30 μm^2, 400×400 pixels; 10×10 μm^2, 300×300 pixels. Topography features encircled in cyan dash line were used to identify the identical microtubule throughout the bending experiment. Red arrows indicate surrounding microtubules ruptured under compressive load. (b) Single microtubule underwent buckling from 0% ~ 13.3% compressive strain. (c) Bending radius of the microtubule shown in (b) as a function of applied compressive strains.

5.2   Actin Filament and α-actinin on Rippled Surface

5.2.1 Background

Actin filament (F-actin) is a soft and flexible cytoskeleton component[91], unlike rigid microtubules. When a cell experiences external stress, the F-actin network is reorganized with an increased binding affinity of cross-linker protein, α-actinin,[92] to stabilize the actin filament bundle.[93]

5.2.2 Materials and Experiment Setup

Due to the negatively charged surface of the F-actins, the pristine PDMS surface, which is slightly negatively charged, is not the optimum substrate for direct incubation. To create a surface apt to adsorb F-actins, the positively charged lipid bilayer with the following composition was prepared at a gravimetric ratio: 70% DPPC and 30% DPTAP. The preparation of the lipid solution was as same as described in chapter 2. The pristine PDMS is hydrophobic, so it's difficult to form a stable lipid bilayer on such a surface[94]. Therefore, the PDMS substrate was treated by ion bombardment for 5 seconds, and 5 μL of
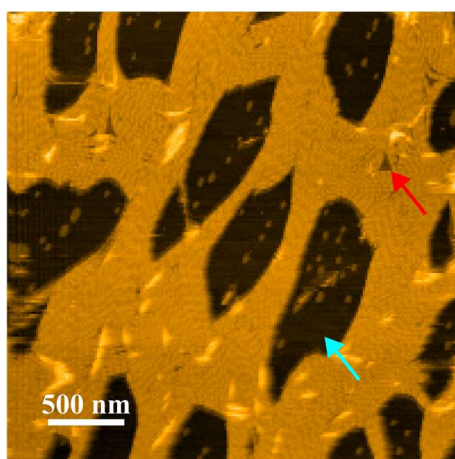

Figure 5.3   Adsorption of F-actin on the lipid covered PDMS. The red arrow indicates the lipid bilayer where no F-actin was adsorbed; the cyan arrow indicates the PDMS substrate without lipid bilayer, where no F-actin was found on such region. Sample scan mode, 3×3 μm^2, 200×200 pixels.

DPPC/DPTAP lipid solution was immediately deposited on the treated PDMS surface. The substrate was kept at 70 °C for 20 minutes to promote the lipid bilayer formation, then rinsed thoroughly with pure water. The PDMS substrate was then transferred to the sample stage and clamped with clips afterward. 5 μL of F-actin solution was incubated on the substrate for 10 minutes and rinsed with imidazole imaging buffer to remove excess proteins. Tip-scan HS-AFM images shown in Figure 5.3 confirmed that F-actins were vastly adsorbed on the lipid bilayer while no F-actin was found on the plasma-treated PDMS region. After applying 30% strain in the Y direction, surface buckling was triggered as expected. Figure 5.4 (a) shows the lipid bilayer, including the adsorbed F-actins, following the ripple topography.

To inspect the interplay between α-actinins and F-actins on different ripple surfaces, the α-actinin solution was injected into the imaging solution with the final concentration of 50 nM after the F-actins were adsorbed on the free, flat lipid/PDMS substrate. Images were taken at different strains applied with tip-scan mode.

5.2.3 Experimental Result

Figure 5.4 (b) shows the F-actin/α-actinin complex at 0% and 40% strained substrate. Neither F-actin nor α-actinin was found to attach outside the lipid bilayer region at both strain conditions. Images with the ripple structure were processed with a high-pass filter to improve the image contrast. The binding between F-actins and α-actinins on different surfaces shows distinct patterns. On the unstrained flat surface, the α-actinins bridged between neighboring F-actins with diverse angles relative to the F-actins. On the curved surface, α-actinins bound to the F-actins in an aligned orientation. In contrast, α-actinins along the F-actins were denser on the curved surface. The mean distance of adjacent α-actinins along the F-actins was calculated which calculation method described as follows with the illustration shown in Figure 5.5. A line profile (drawn in the red line in Figure 5.5 (a)) was taken along the approximately middle position between two F-actins. Mean distances between adjacent α-actinins, pointed by cyan arrows, were calculated by averaging the distances measured between the apexes of the line profile [Figure 5.5 (b)] .

It's found that F-actins allowed a denser bridging with α-actinins due to surface curvature. The average distance between α-actinins was 9.0 nm for curved substrates and 14.5 nm for the flat.[90] It's reported that the tension applied to the F-actin enhanced the binding affinity of α-actinin to F-actin.[95] Here, the HS-AFM results on the curved surface pointed out that the bending of F-actin might also affect the F-actin/α-actinin network. As the α-actinin was comparatively more diffusive on the lipid bilayer than the F-actins, the

bent　F-actin could equivalently act as a force sensor that more α-actinins were recruited when the more α-actinin binding sides were exposed due to bending.[96] Detailed molecular mechanisms underlying the dynamics observed here would require further investigation.
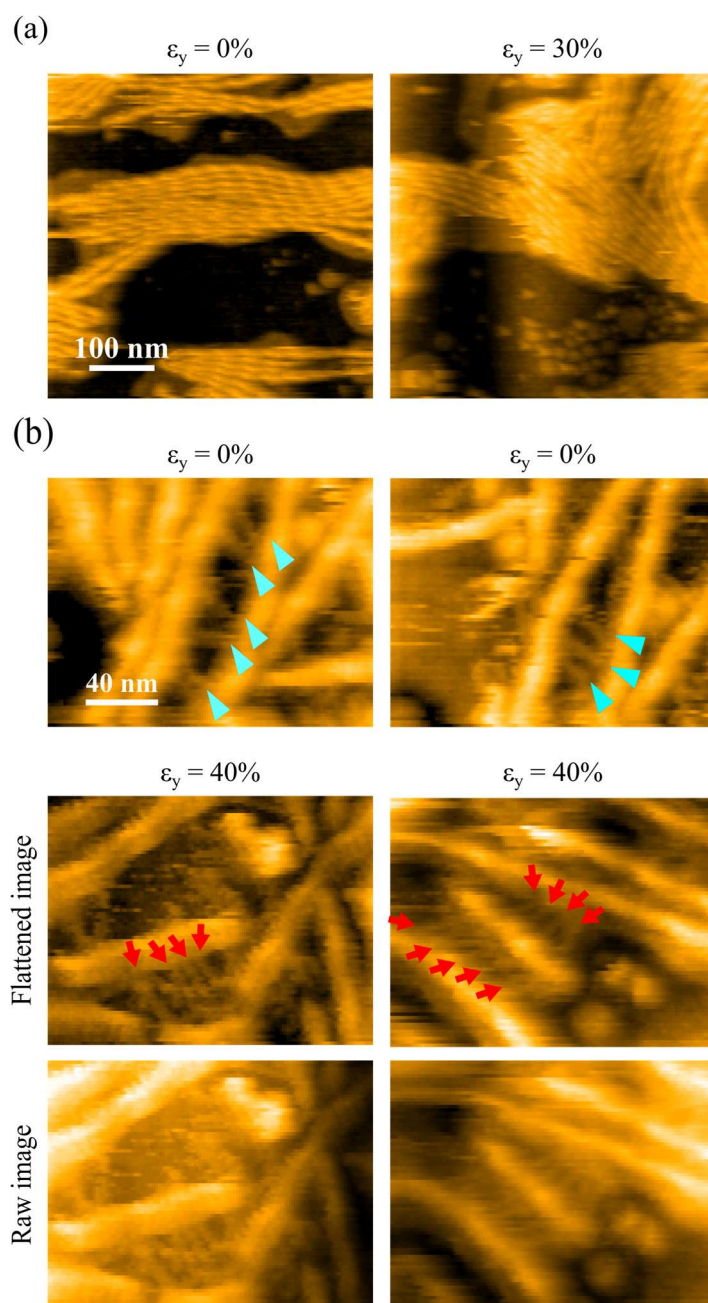
Figure 5.4　Actin filaments bridged by α-actinin on locally curved PDMS surfaces. (a) Deposited F-actin conformed to the local surface curvature. Tip-scan mode, $500 \times 500 \text{ nm}^2$, 150×150 pixels, 1 s/frame. (b) HS-AFM image of binding between α-actinin and actin-filaments. Tip-scan mode, $135 \times 64 \text{ nm}^2$, 101×48 pixels, 0.2 s/frame.
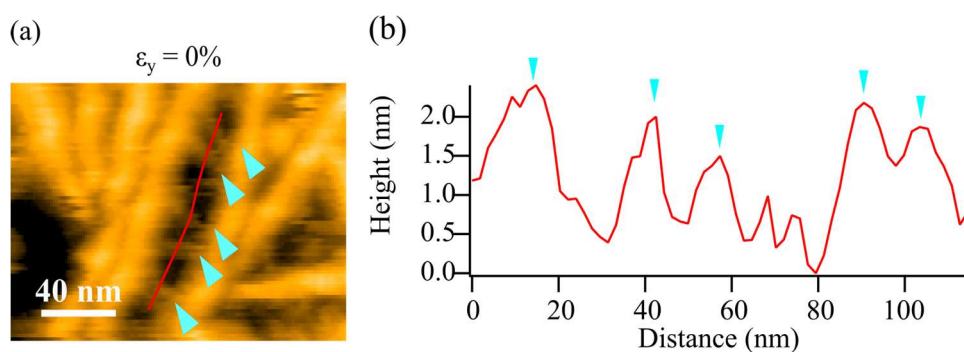
Figure 5.5　Calculation of average distance between adjacent α-actinin (indicated with cyan arrow). (a) Line profile was taken along the middle position between the bridged F-actins. (b) Average distance was calculated from the distance between the apexes recognized as α-actinin.

5.3 BIN1 K436X Adsorption on Rippled Surface

5.3.1 Background

Bridging Integrator-1 (BIN1), also known as Amphiphysin-2 and Myc box-dependent interacting protein 1, is a protein encoded in the human BIN1 gene. The structure of
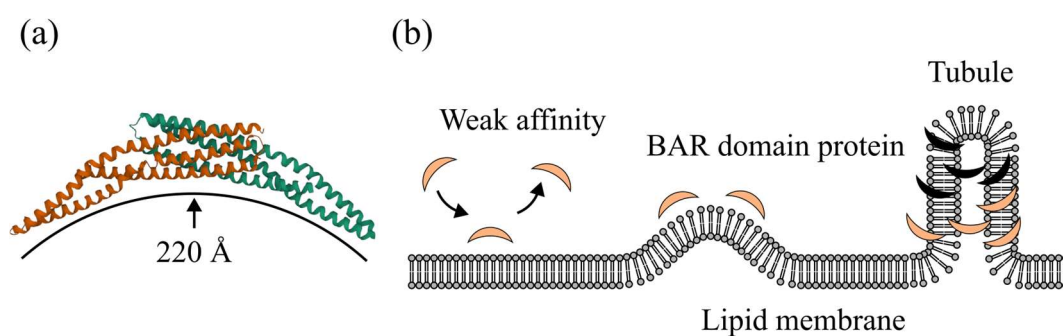
Figure 5.6　Interaction between BIN1 protein and lipid membrane. (a) Structure of BIN1. (PDB: 2FIC) The BIN1 has a concave structure with radius around 220 Å. (b) BAR domain adsorbs on the curved lipid membrane resulted membrane remodeling.

BIIN1 protein[97] is shown in Figure 5.6 (a). BIN1 can sense the plasma membrane curvature[98] and be found to be a crucial protein associated with membrane remodeling during endocytosis[99], membrane trafficking[100], and cell division.[101] The membrane deformation caused by BIN1 was considered a result of electrostatic interaction that the concave side of BIN1 protein, which is positively charged,[102] interacts with the negatively charged lipid membrane, like phosphatidylinositol 4,5-bisphosphate (PI(4,5)P$_2$).[100] Once the initial binding on a flat surface is established, the curvature of the lipids is enhanced by BIN1. As a result, the concave shape of BIN1 can attach to the bent surface easier and forms tubules in advance, as illustrated in Figure 5.6 (b). Multiple diseases are involved with BIN1, such as Alzheimer's disease[103] centronuclear myopathy (CNM),[104] and cancer progression.[101] By far, BIN1 binding affinity assays were mainly conducted with fluorescence microscopy.[102,105] As the controllability of the surface curvature has become possible on tip-scan HS-AFM, curvature-dependent binding dynamics of BIN1 on a lipid bilayer surface was observed.

5.3.2 Materials and Experiment Setup

Lipid solution was prepared according to literature[106] at gravimetric ratio: 64% porcine brain PS (840032C, Avanti), 2% PI(4,5)P$_2$ (805155P, Avanti), 14% porcine brain PE (840022C, Avanti) and 20% cholesterol (70000P, Avanti). Materials in powder form, PI(4,5)P$_2$ and cholesterol, were dissolved in the chloroform first and mixed with the rest components. The lipid was rehydrated with 0.3 M sucrose to make a lipid concentration of 1 mg/mL and incubated at 37 °C for 2 hours. Tip sonicator was used to homogenize the solution before aliquot and stored at -80 °C. Before the experiments, the lipid solution was thawed and diluted with a Tris-based buffer (10 mM Tris-HCl, pH 7.5, 150 mM NaCl, 2 mM CaCl$_2$) to a concentration of 0.1 mg/mL and sonicated for 15 seconds with tip sonicator. PDMS substrate was first treated by UV-O$_3$ for 1 hour to make a stiff glass-like surface for later controllable surface curvature purposes. However, the oxidized PDMS surface was considered negatively charged as the hydroxyl group created the negatively charged lipid vesicles that couldn't form a stable layer on this surface. Therefore, oxidized PDMS surface was immersed with 1% APTES for 5 minutes and drained with pure water. Following that, 5 μL of the lipid solution was incubated on the silanized surface at 55 °C for 20 minutes and rinsed thoroughly first with pure water first and with cytosolic buffer (25 mM HEPES, 25 mM KCl, 2.5 mM Magnesium acetate, 0.1 M K-glutamate, pH 7.2). Cytosolic buffer was also used as the AFM imaging buffer. Figure 5.7 (a) shows the lipid bilayer almost completely covered the PDMS surface except for several cracks, as

indicated by arrows. Recombinant BIN1 mutant K436X, which has enhanced membrane deformation capacity[106], was diluted with the cytosolic buffer to 2.1 µM and injected into the AFM imaging buffer to a final concentration of 25 nM. The BIN1 K436X binding/dissociation dynamics under different surface curvatures were observed by tip-scan HS-AFM. The surface curvatures were controlled by stretching the PDMS substrate from a length of 10 nm to 12 mm (20% strain) and 14 mm (40% strain).

5.3.3 Experimental Result

Line profiles shown in Figure 5.7(b) were used to estimate the local maximum curvatures of the surface buckling profiles at a close distance about the apex. Three points, including the apex and two neighboring points distance 20 nm from each side of the apex were used
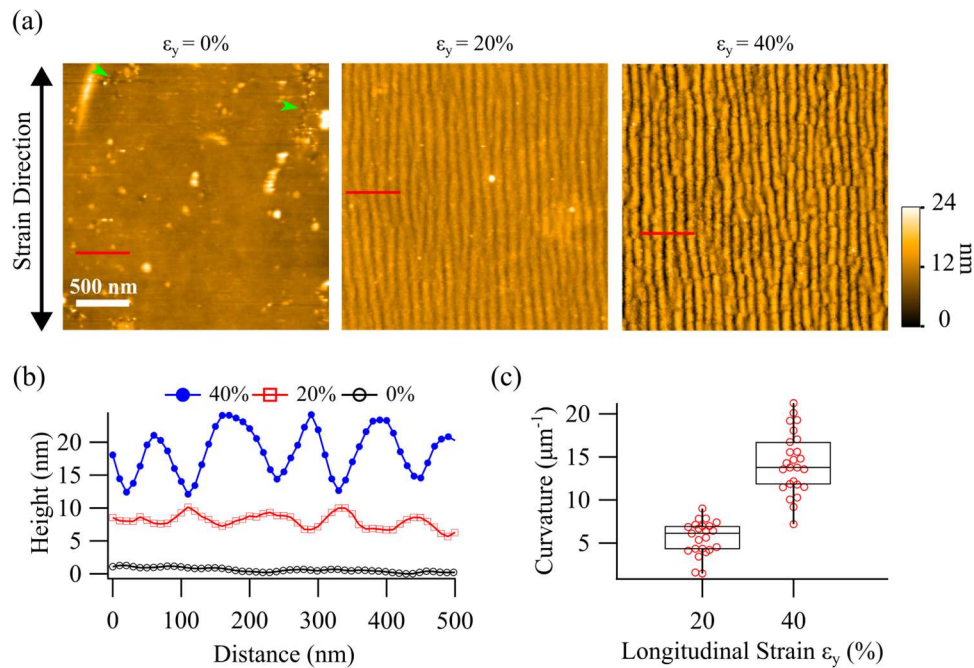
Figure 5.7   Strain-dependent supported lipid bilayer topography on the UV-O$_3$/APTES modified PDMS substrate. (a) AFM images of the surface at strain values of 0%, 20% and 40%. Sample scan, 2.5×2.5 µm^2, 250×250 pixels. The green arrows shown in (a) indicate defect on the lipid bilayer. (b) Line profiles normal to the ripple patterns indicated by red lines in (a). The profiles are respectively shifted by 5 and 10 nm for 20% and 40% strain for clarity. (c) Curvature of the ripple apex region determined from line profiles.

to fit a circle equation. The statistical analysis between bending radius and strains is plotted in Figure 5.7 (c).

The binding event of BIN1 to the flat lipid before applying stretching was not found(Figure 5.8 (a)). This implies that the interaction force between the positively charged membrane is not strong enough to fix BIN1 stably with the flat lipid, even if the affinity-enhancing CNM-associated mutant K436X is easily detached by disturbance from the AFM tip or the binding time is much shorter than the finest time resolution, 0.1 s/frame, of HS-AFM we used. In contrast, BIN1 was clearly observed on curved lipid
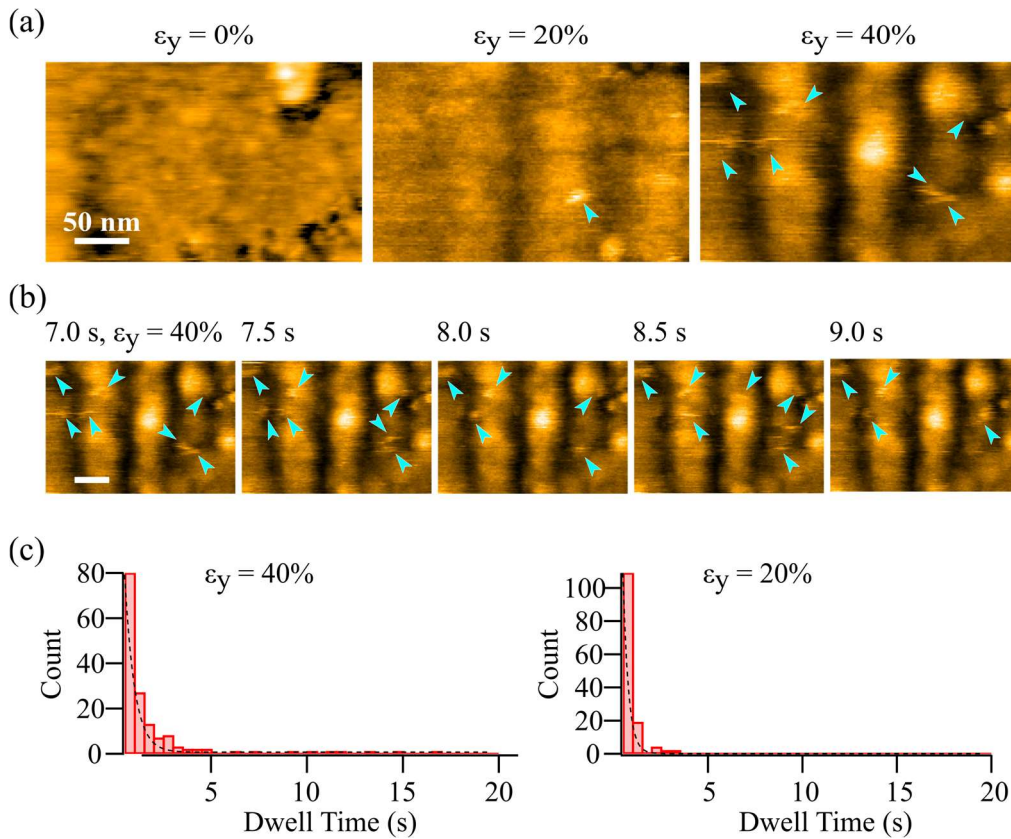
Figure 5.8   Curvature-dependent binding kinetics of BIN1 K436X. (a) BIN1 bound to a high local curvature surface under 40% strain , low local curvature under 20% strain, and flat surface. Tip scan mode, 300×210 nm^2, 150×105 pixels, 500 ms/frame. (b) Snapshots of the dynamic binding and dissociation process of BIN1 to the highly curve surface at 40% strain. (c) Measured within the same time, the dwell time of BIN1 was higher on the 40% strained surface compared to the 20% strained surface (103 frames, $N_{40\%} = 153$, $N_{20\%} = 137$).

membrane surfaces even at 0.5 s/frame, as shown in Figure 5.8 (b). Most BIN1 molecules were found stably bound near the apex of a lipid-covered ripple and less so at the other region, suggesting preferential binding of BIN1 to positive curvature. Example HS-AFM images of the BIN1 interacting with a curved lipid surface under 40% strain are shown in Figure 5.8 (b). Average counts of BIN1 proteins bound to the lipid surface per frame were calculated within a scanning area of 300×210 nm^2, giving the average count of 5.8 ± 1.7 and 1.8 ± 1.1 (N = 103 frames) at 40% and 20% strain, respectively. The result confirmed that BIN1 has a higher binding affinity to larger curvature surfaces.[98,107] The dwell time analysis of BIN1 with respect to surface curvature is shown in Figure 5.8 (c). Histograms of dwell time were fitted with a single exponential decay, giving the time constant τ of 1.83 ± 0.09 s for 20% strain surface and 3.77 ± 0.06 s for 40%. The difference in lipid curvature between 5.59 μm^{-1} (20% strain) and 14.27 μm^{-1} (40% strain) results in distinct binding behavior. In previous studies, the interaction between BIN1 and lipids could only be characterized by a change in fluorescence intensity contributed to the BIN1 adsorption on different curvatures.[98,107] In contrast, the developed system allows the direct measurement of curvature-dependent binding and dissociation dynamics at the single-molecule level.[90]

5.4 Tensile strain and Breakage of Poly(methyl acrylate) Latex Film

5.4.1 Background

Plastic products are ubiquitous in our daily routine because of their durability and scaled industry. Latex films, as one of the applications, are widely applied in painting,[108] coatings,[109] and adhesives.[110] The latex film is made with water-dispersed latex microparticles. After the water is evaporated above glass-transition temperature, the discrete latex microparticles coalesce with each other, accompanied by deformation and interpenetration of particles. Eventually, a honeycomb-like arrangement film is formed. In contrast to latex film formation, the conventional solvent casting method uses organic solvents to dissolve the polymer and spread it out to the film mold. The films are collected after the solvent is evaporated. For the reason of the solvent-free process, waterborne latex film formation is considered a more environment friendly alternative. To increase the mechanical properties of the latex films, the addition of additives or annealing after

formation is applied.[111] Recently, the relation between the fracture energy and interpenetration depth of the microparticles was investigated with the poly(butyl-co-methyl methacrylate) and showed a positive correlation.[112] However, the fracture mechanism at the nanoscale is still unclear. In this study, tensile fracture of poly(methyl acrylate) film was investigated with the bilateral stretching device.

5.4.2 Materials and Experiment Setup

Poly(methyl acrylate), PMA, is a synthetic polymer of methyl acrylate, and has properties including flexure, strong, hydrophobic[113], and soluble in the less toxicity solvents, i.e., water/ethanol solution.[114] To prepare the PMA film, PMA microparticles were first prepared by the surfactant-free emulsion polymerization with methyl acrylate (138-07676, Wako, Japan) 1,6-hexanediol dimethacrylate (6606-59-3, Tokyo Chemical Industry, Japan) as a crosslinker, potassium persulfate (169-11891, Wako, Japan) as an initiator. PMA latex films were fabricated by depositing the latex-microparticle dispersion on the silicone rubber mold and evaporating at room temperature.[115] Formation of the PMA latex film is shown in Figure 5.9. The PMA film was then trimmed to a size of 14×5 mm^2 and clamped on the bilateral stretching device as described with a clip-to-clip distance of 10 mm as the initial length. Stretching was conducted at a strain rate of 10 μm s^{-1} with a step of 1 mm by sample-scan mode AFM in the air with an Arrow cantilever (Arrow UHFAuD, NanoWorld, Switzerland). The oscillation amplitude was driven to 10 nm at ~ 1.3 MHz, and the setpoint for feedback controller was configured to 8 nm.

5.4.3 Experimental Result

The PMA latex film was first stretched along the Y axis from the initial length to 20%, as shown in Figure 5.10. The closely packed microparticle was observed. Unlike the experiments demonstrated in the microtubule bending assay, the surface of PMA latex film was rough rather than flat. The observation of the same area under different strain steps was not possible due to the limited stroke of the Z-scanner. Thus, it was necessary to withdraw the cantilever before increasing the load and re-approach. This process resulted in a loss of recognition of the topographical features shown in the earlier state. Along the strain direction, the particle shape was not homogeneous on the surface at the initial state. This could be related to the surface roughness that some particles were under compressive or tensile load during the drying-deformation transition. As the strain went up to 20%, both the particle shape was elongated along the stretch direction, and the

Latex film solution

Polymer particles
dispersed in water

Water evaporation above Tg

Particle deformation during and after drying

Particle interpenetration
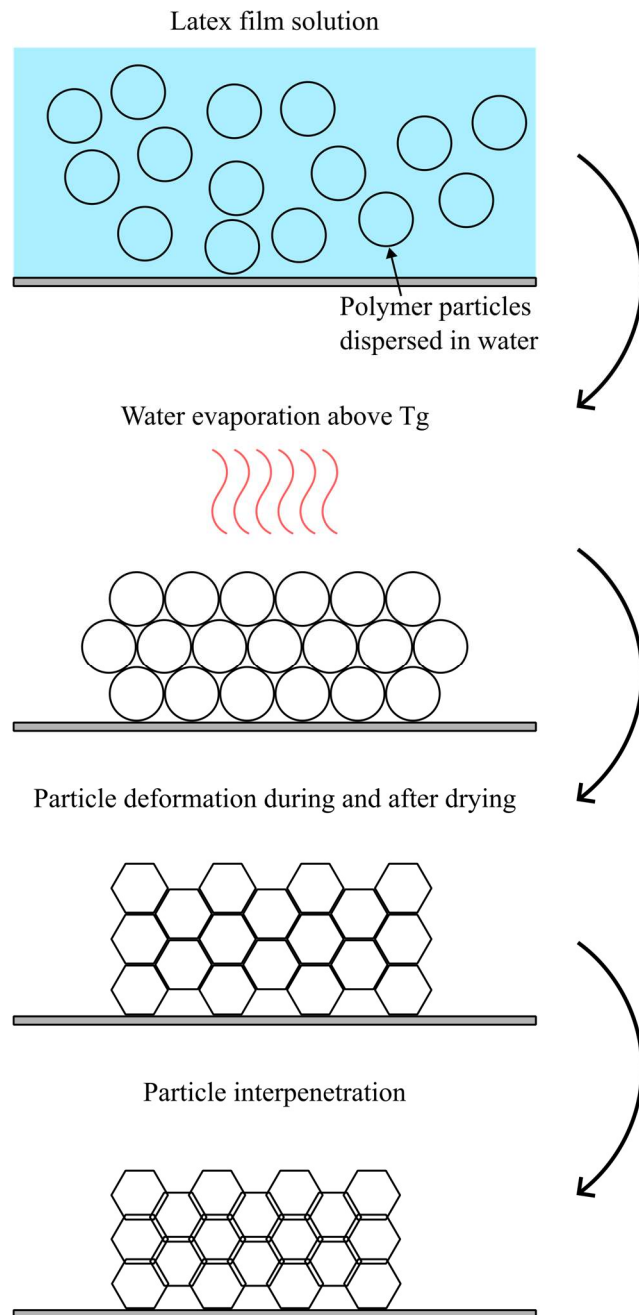
Figure 5.9   Preparation of the PMA latex film. PMA microparticles dispersed in the water was dries above the glass transition temperature, T_g, and formed closed packing structure followed by deformation and interpenetration.
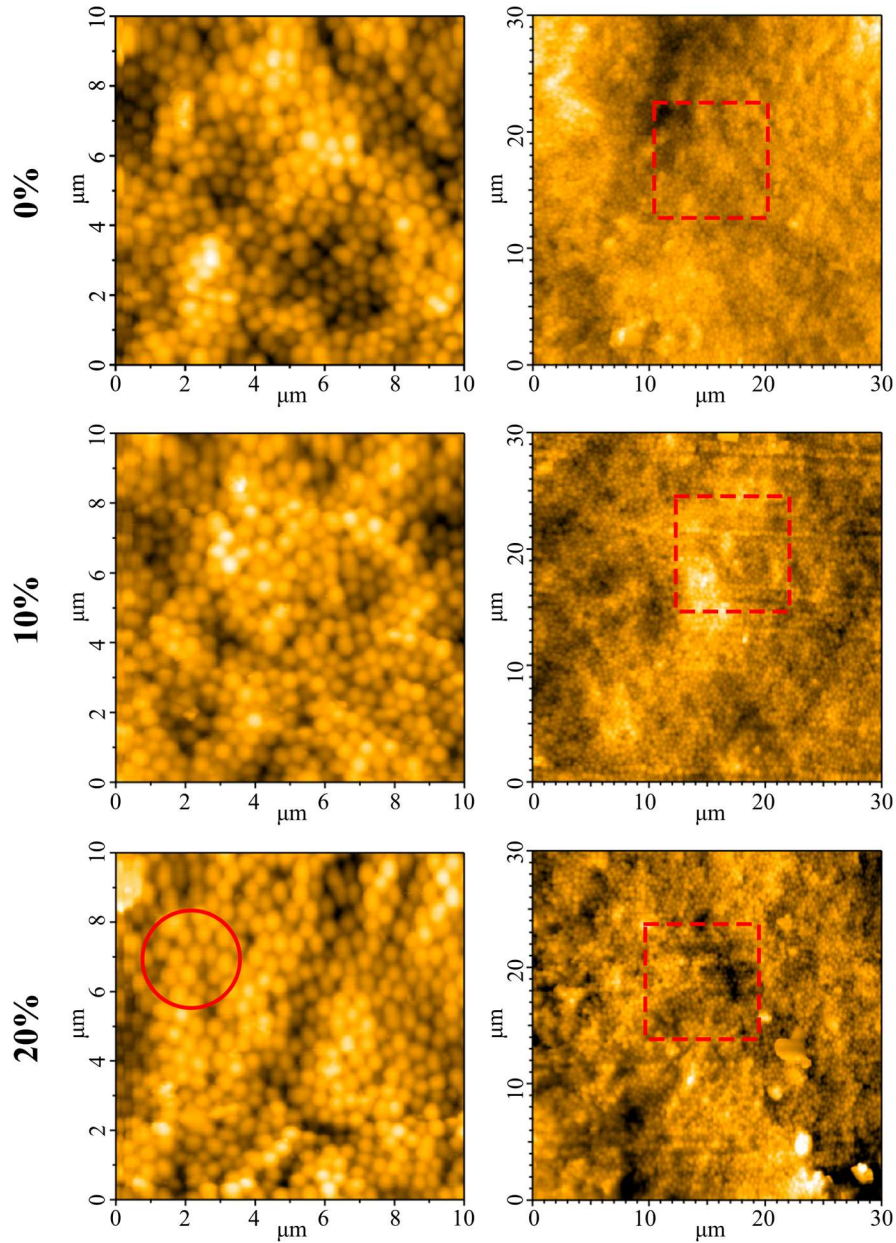
Figure 5.10 AFM images of PMA latex film subjected to strain below 20% show surface integrity. Distance between particles was enlarged as strain increase. The red box in the right image highlights the same area as the corresponding image in the left column for each row. Sample scan mode, 500 × 500 pixels. Left column: $10 \times 10\ \mu m^2$; right column: $30 \times 30\ \mu m^2$.

71

adjacent distance between particles was increased on certain regions (encircled in red, 20% strain). From a view with 30×30 μm^2 of the image at each strain, taken a right after the 10×10 μm^2, neither obvious surface buckling, nor breakage was found up to 20%.

Starting from 30% strain until the end of the experiment, and the imaging drifting was noticed from the consecutive frames. To compensate for the drift effect, a simple image scaling method was used to resize the image dimensions. The method is described below with the illustration in Figure 5.11. Assume a particle on the image was identified at y_0 with timestamp t_0, and all images were acquired with the same imaging area and speed. In the frame at t_1, the particle was found to be at y_1. With this information, the drift velocity, v_{drift} of the topography can be derived by assuming the drift speed between t_0 and t_1 was constant. v_{drift} was estimated by dividing the travel distance by the time passed from the time passed between the timestamp of the particle:

$$v_{drift} = \frac{y_0 - y_1}{t_1 - t_0}.$$

(5.1)

With drift velocity, actual scanning dimension y_{drift} was derived from the preset imaging time per frame, t_{frame}, scanning dimension along the drift direction, y_{scan}, and v_{drift} as follows:

$$y_{drift} = v_{drift} \times t_{frame} + y_{scan}.$$
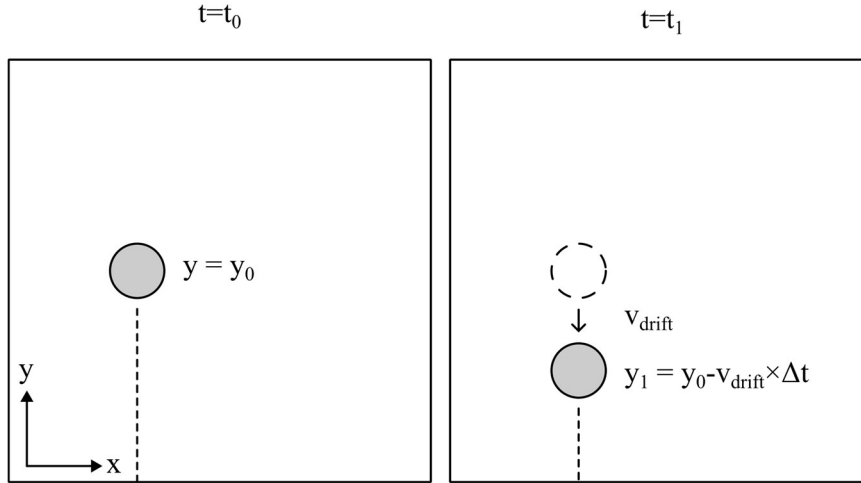
(5.2)

Figure 5.11   Image scaling method depending on the particle location shifted between frames. A particle located at y_0 when t_0 was later found at y_1 with new timestamp t_1. These parameters were used to restore the image distortion due to substrate drift. Calculation is described in the text.

Figure 5.12 shows the AFM image of PMA film taken at 30%, 40%, and 50% strain, respectively. It's noticed that the dimension deformation of the particles did not follow with the strain as much as expected. However, gaps between the particles were enlarged as circled with the red line. In addition, clear horizontal stripes were found when imaging large areas at 40% and 50%.

In both images of 60%, the trench area revealed the particles were aligned in a wavy pattern (indicated with an arrow in 60% image), as shown in Figure 5.13. It's believed that the wavy pattern was correlated with buckling. As the particles were torn apart from the tensile direction, buckling happened simultaneously on the serially connected particles, termed particle streamlines here, in a transversal direction triggered by the increased compressive load. More wavy patterns were identified as the strain increased to 70% and 80%. Clear separation between the particle streamlines was observed together with pits (the red circle on the right image under 80% strain) in the trenches. It's not yet clear whether the pit existed inherently from the fabrication process or if it was a structural defect resulting from the stretching. The particle shape remains deformed, though not proportionally, with the strain up to 70%. Interestingly, the 80% strain image revealed that the particles were restored to a much spherical shape. This suggests that the tensile load at this strain was adsorbed by other mechanisms instead of particle deformation.

88% and 100% images were taken, as shown in Figure 5.14. Due to the design limit of the stretching device, strain higher than 80% was applied by fixing the substrate on the stage steadily, so the film did not restore its strain, resetting the clips and re-clamping the substrate. From the large image of 88%, the flat area of particle film was shown, and the wavy pattern was identified on the surface, accompanied by multiple pits. In the 100% strain images, the orientation of the particle alignment and trenches reverted to a positive slope. The corrected image range along the stretch direction indicates a drastic change in drift velocity, thus represents the PMA film underwent a comparatively rapid relaxation. As the strain reached 110%, bridging between the particles along the Y direction was widely found. Also, the trench direction was oriented to a larger degree. From the topography, no obvious difference from the topography could be noticed from 110% to 140% strain shown in Figure 5.15.

It's speculated that the material relaxation was realized by the reduced particle interpenetration depth and the opening of the trench, both mechanisms attributed to the fracture energy. Therefore, the horizontal stripes initiated by 40% strain were considered the early breakage of the surface, followed by enlarged trenches and pits.
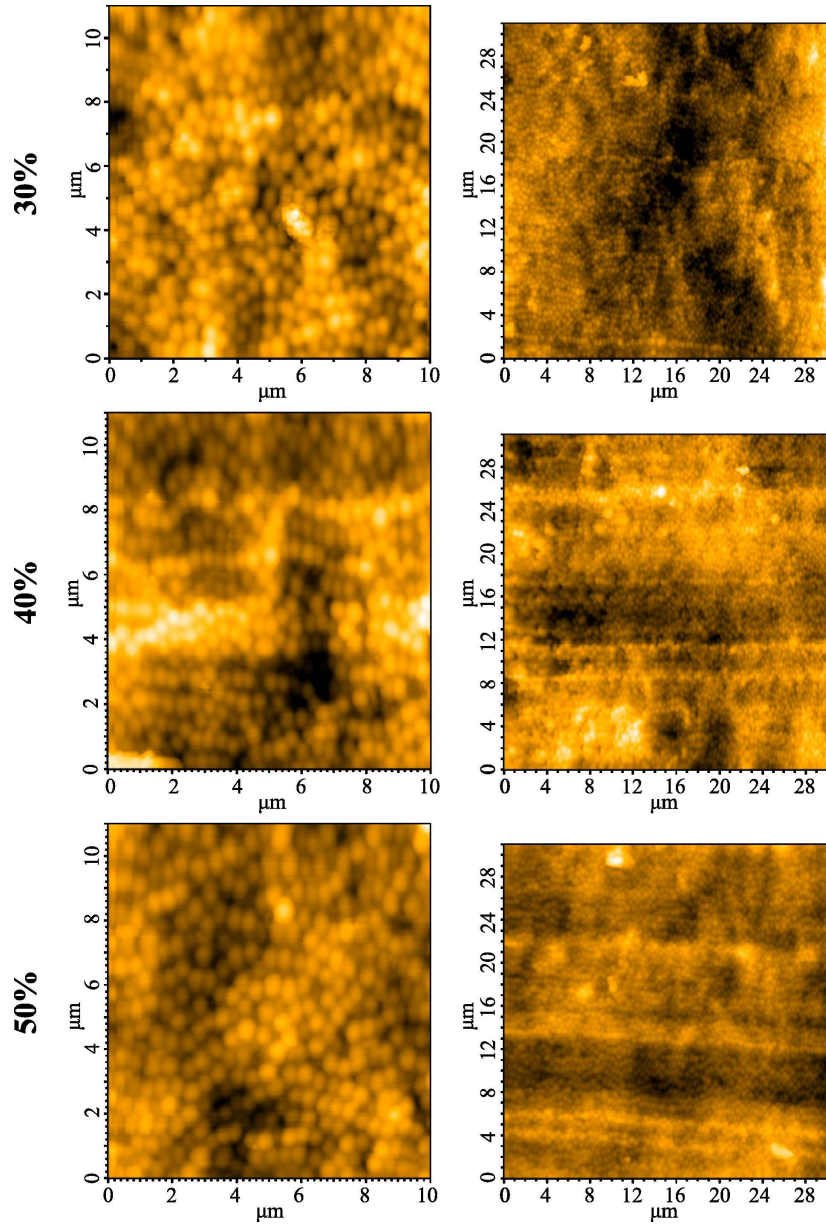
Figure 5.12 PMA latex film subjected to strain of 30%, 40%, an 50% strain show topography deformation in large scale, yet the particle shape was not greatly affected. Interpenetration between particle were likely to be untangled (red circle). The red box in the right image highlights the same area as the corresponding image in the left column for each row. Sample scan mode , 500 × 500 pixels. Left column: 10 × 10 μm²; right column: 30 × 30 μm².
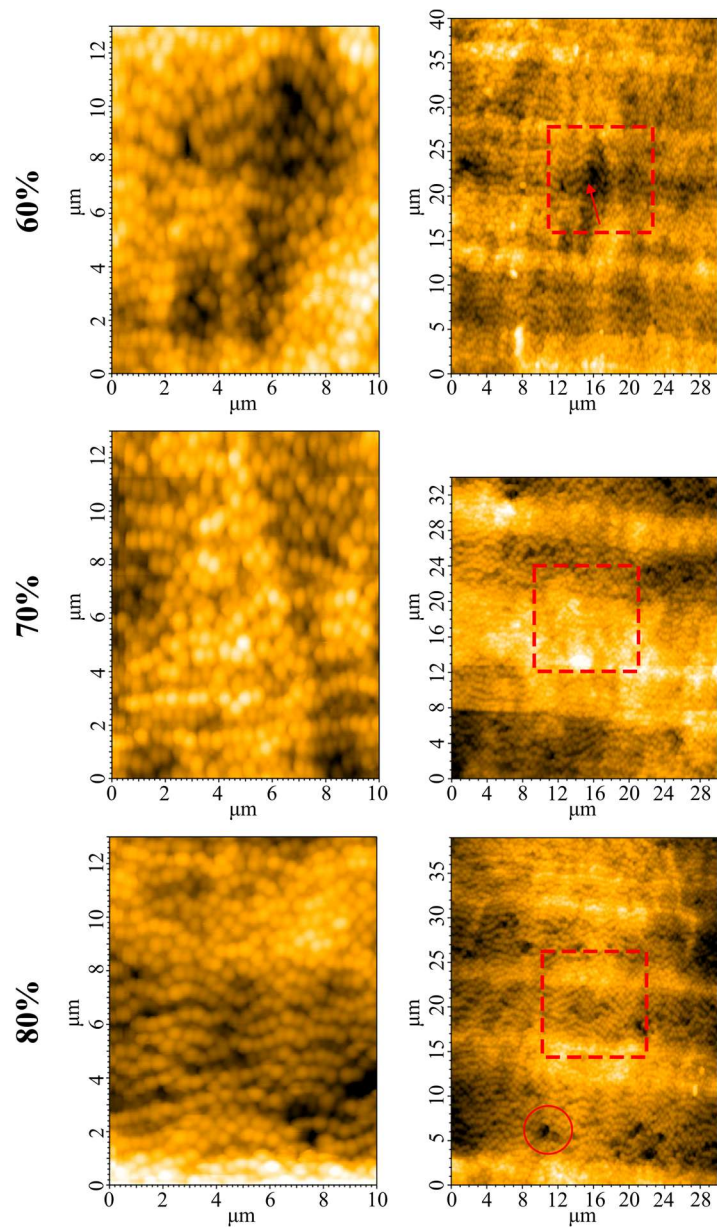
Figure 5.13　AFM images of PMA latex film subjected to strain of 60%, 70%, and 80% show the particle streamline (pointed with red arrow as example) was distorted as strain increase, accompanied with increased pit formation (red circle). The red box in the right image highlights the same area as the corresponding image in the left column for each row. Sample scan mode, 500 × 500 pixels. Left column: 10 × 10 μm^2; right column: 30 × 30 μm^2.
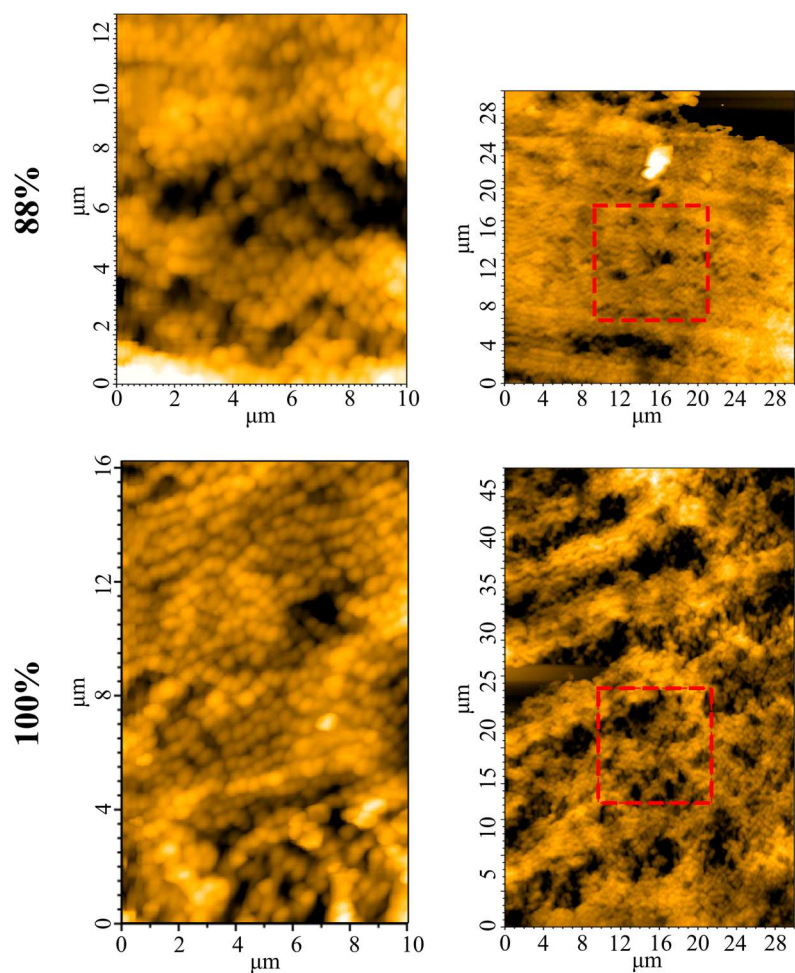
Figure 5.14   AFM images of PMA latex film subjected to strain of 88% and 100% show drastic surface damage on the relative flat surface (88%) as well as the trench region (100%). The red box in the right image highlights the same area as the corresponding image in the left column for each row. Sample scan mode, 500 × 500 pixels. Left column: 10 × 10 μm^2; right column: 30 × 30 μm^2.
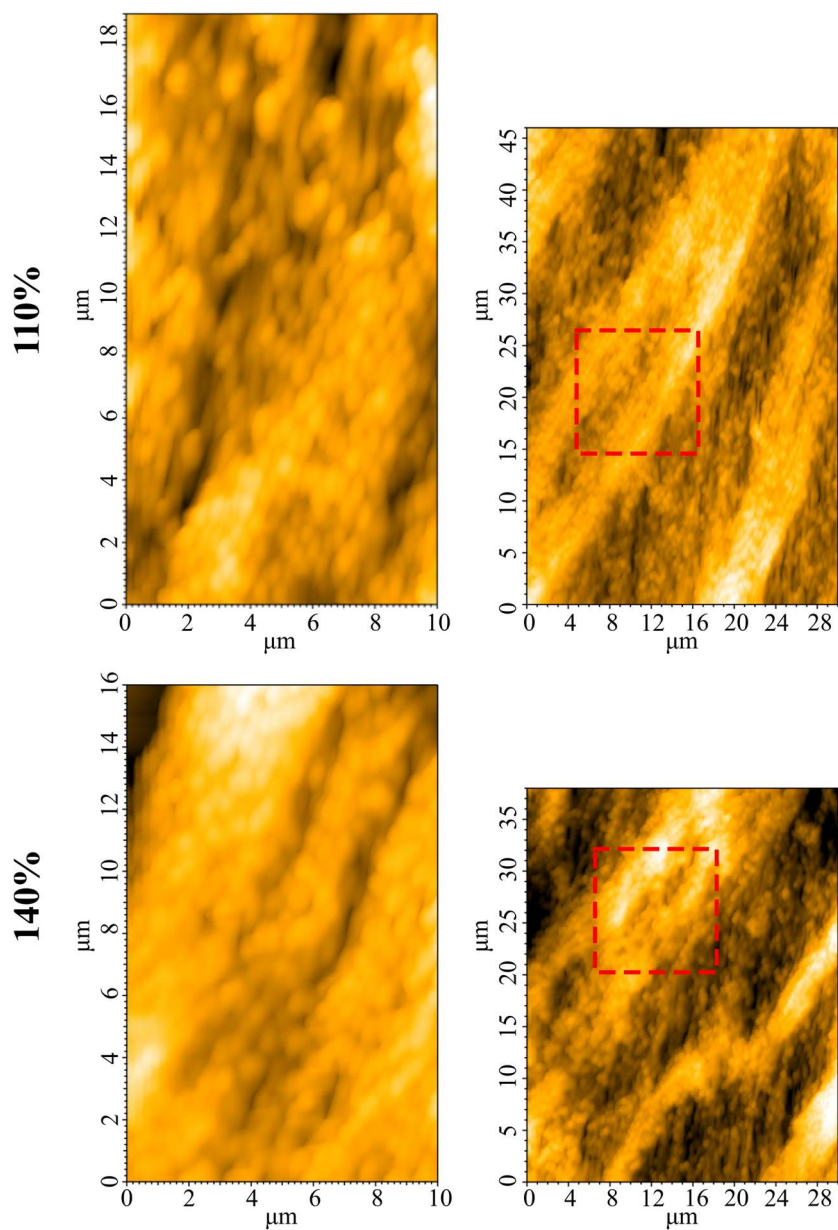
Figure 5.15   AFM images of PMA latex film subjected to strain of 110% and 140% exhibited apparent trench re-orientation. Linkage between particles was found and considered as reverted behavior of interpenetration. The red box in the right image highlights the same area as the corresponding image in the left column for each row. Sample scan mode, 500 × 500 pixels. Left column: 10 × 10 μm^2; right column: 30 × 30 μm^2.

5.5 Summary

Three experiments with different biomolecules and one with polymer film were conducted in this chapter. By using the stretching device, tip-scan HS-AFM observed the bending and buckling event of a particular microtubule. Combined with the oxidized substrate, surface ripple triggered by compressive load provides a controllable platform to investigate the binding affinity of the proteins. Therefore, the binding behavior between F-actin and α-actinin was observed under different curvatures and indicated a curvature-dependent binding preference. With a similar method, BIN1 binding affinity to the rippled surface was analyzed at different surface curvatures as well. The application of the combined machine also extended to visualize the micrometer scale surface damage of latex film under extreme strain in the air. With the above examples, HS-AFM combined with a stretching device is shown to be a powerful tool for studying various samples under mechanical stimulation.

Chapter 6 Conclusion and Prospect

6.1 Conclusion

In this thesis, an instrument capable of uniaxially stretching elastomeric substrates with simultaneous HS-AFM was described. The combined instrument was then used for studying the dynamics of nanometer-scale biological samples under mechanical stress, as well as the breakage mechanism of latex film.

A tip-scan HS-AFM was constructed with an improved tip-fixation method. Evaluation of the tip-scan mode scanning was conducted with fragile and dynamic biological samples in the liquid with high image throughput. A sample scanner covering a $120 \times 120 \ \mu m^2$ area was incorporated into the tip-scan HS-AFM system to provide wide-area, low-speed AFM imaging.

The developed uniaxial stretching device developed can stretch an elastomeric substrate to nearly twice its initial length with a resolution of 50 nm per step. This stretching device was integrated into the tip-scan HS-AFM as the capacious space around the sample stage. Furthermore, the wide-area scanner allowed comparably easy compensation for positional changes caused by substrate stretching. The stretching device was evaluated with a PDMS sheet molded with micrometer scale square patterns. AFM images of the square pattern in the same area were taken when applying strain. Dimensions of the square pattern were determined, and it confirmed that the square pattern was stretched linearly in the longitudinal direction. Dimension shrinkage in the transverse direction due to Poisson's effect was observed as well.

Four surface treatment methods on the PDMS surface were demonstrated. UV-O_3 and ion-bombardment treatments as a one-step method were used to oxidize the PDMS surface, which resembled a glass-like surface. Surface buckling on the oxidized substrate was characterized. Non-oxidation surface modifications, including APTES, biotin linker and kinesin anchor, were also verified with biological samples imaged by HS-AFM.

The contribution of HS-AFM with an integrated stretching device to biophysical problems was demonstrated with three challenging experiments. First, in a microtubule bending experiment, the accumulative compressive load was applied via kinesin anchors covered on the elastic substrate. Then, buckling of the microtubule was induced and further fractured as the strain increased. In the second experiment, the binding of α-actinin to F-actin was investigated on a curvature-controllable surface created by stretching a

plasma-treated PDMS with the stretching device. The results suggest that the bending-induced strain may modulate the cross-bridging density of α-actinin between F-actins.

Thirdly, PDMS surfaces with gentle ripples created by UV-O$_3$ treatment were used to observe the membrane curvature-dependent binding affinity of BIN1 mutant K436X. As a result, no BIN1 binding to flat lipid membranes was observed, indicating that the binding affinity of BIN1 to the flat membrane is too low to be detected by the HS-AFM. In contrast, it was observed that BIN1 bound to the curved membrane and dissociated from it iteratively. The curvature sensing ability of the BIN1 mutant K436X was therefore verified with high-speed scanning. The dwell time analysis of BIN1 on the curved membrane further showed a higher affinity to the membrane with a curvature of 5.59 μm^{-1} compared to that of 14.27 μm^{-1}.

Finally, the tip-scan HS-AFM combined with substrate stretching device was used to visualize PMA latex film under tension. The face center cubic structure of the microparticle was observed at the free strain. As the strain increased up to 20%, microparticles were locally deformed along the tensile direction. When strain exceeded 30%, microparticles started to form the wavey-like buckling pattern in the transversal direction with trenches formation (40%) on the surface, indicating the initial damage, followed by particle streamlines pulled apart (50%), pit defects formation (60%), until the large-scale particle detaching and rapid relaxation (>100%).

As demonstrated with four applications, ranging from molecule-level protein binding dynamics to micrometer-scale polymer fracture under tensile strain, the combined tip-scan HS-AFM is shown to be a useful and flexible nanomechanical measurement platform.

6.2 Prospect

Several methods were applied to study surface science, including scanning probe microscopy, optical microscopy, electron microscopy, X-ray scattering, and spectroscopy. The advantages of the AFM includes high temporal and spatial resolution in the air, liquid, and vacuum environments. Furthermore, such an all-around analysis technique can bring more fruitful outcomes by improving the current setup and integrating it with other techniques.

As demonstrated in this thesis, the deformation of topography or samples is now accessible with tip-scan HS-AFM. Techniques developed with conventional HS-AFM can be implemented on the tip-scan HS-AFM to study mechanical stimulation related responses, including force mapping, nanomachining,[117] single molecule force microscopy,[118] optical microscopy,[43] and ultrasonic force microscopy.[119]

Besides the analytical techniques, the combined machine itself can also be facilitated further. In stretching characterization and microtubule bending assay, the image region of interest (ROI) required the effort to relocate the cantilever to the ROI as different strains were applied. This effort can be effectively reduced if the sample-scanning speed and scanning area are both improved at the cost of spatial resolution[120] or complex scanning trajectories.[121] Even though, if the relocation demands a huge scanning area that exceeds the operational range of the scanner, a sensing method[122] for estimating such image region displacement should be included, hence automatically compensated[123] with motorized mechanisms. Regarding a higher maximum strain observation without a re-clamping procedure, a stretching device with smaller dimensions was implemented, as shown in Figure 6.1. The stage width is shorter in the stretch direction, which allows a shortened substrate for stretching and results in a higher strain. It is anticipated to conduct imaging with latex-film-like high flexible material in the future.

As for the experiments conducted in this thesis, further investigations of each experiment are listed here with possible directions. In the microtubule bending assay, microtubule kink was created under compression. It's worth studying whether the kinesin motor can overcome such a significant structural defect and continue the linear motion on the other end of the segment[124] or whether the motor protein would jam at the edge of the fracture.[125] In the F-actin/α-actinins binding on curved structure experiment, quantitative analysis with binding orientation, the average length of α-actinin, and binding force related to curvature should be further conducted. Though BIN1 adsorption on wrinkle lipid surface was visualized at single-molecule resolution, T-Tubule formation

was not observed in the experiment. It's speculated that the non-ATPase protein BIN1 couldn't further deform the strongly fixed lipid and form a higher curvature lipid protrusion to initiate the T-Tubule formation. Therefore, advanced studies on surface treatment to allow deforming lipid bilayer with BIN1 should be considered. In the last demonstration with PMA latex film, the extreme strain was applied by re-clamping the film and stretching afterward. The interpenetration between the microparticles, however, was yet well-studied. For example, the minimum energy required to break the interpenetration is still unknown. By combining a nanometer-scale probe[126] to manipulate the individual particle, one could resolve the nanometer-scale fracture pattern between particles, thus deepening the understanding of the latex film fracture mechanism.

Strain: 0 ~ 80%   Strain: 0 ~ 200%

Figure 6.1   Comparison between different sample stages. Original stage (left) has a smaller strain limit. A newly implemented stage can reach further strain up to 200% (right).

References

[1] G. Binnig, C. F. Quate, and C. Gerber, *Phys. Rev. Lett*. **56**, 930 (1986).

[2] B. N. J. Persson, *Chem. Phys. Lett.* **141**, 366 (1987).

[3] Y. Martin, C. C. Williams, and H. K. Wickramasinghe, *J. Appl. Phys.* **61**, 4723 (1998).

[4] G. Meyer and N. M. Amer, *Appl. Phys. Lett.* **53**, 1045 (1988).

[5] S. Alexander, L. Hellemans, O. Marti, J. Schneir, V. Elings, P. K. Hansma, M. Longmire, and J. Gurley, *J. Appl. Phys*. **65**, 164 (1998).

[6] M. Tortonese, R.C. Barrett, and C. F. Quate, *Appl. Phys. Lett.* **62**, 834 (1993).

[7] M. Rief, M. Gautel, F. Oesterhelt, J. M. Fernandez, and H. E. Gaub, *Science* **276**, 1109 (1997).

[8] R. Garcia, *Chem. Soc. Rev.* **49**, 5850 (2020).

[9] B. R. Neugirg, S. R. Koebley, H C. Schniepp, and A. Fery, *Nanoscale* **8**, 8414 (2016).

[10] S. R. Baker, S. Banerjee, K. Bonin, and M. Guthold, *Mater. Sci. Eng*. C **59**, 203—212 (2016).

[11] D. Ahrens, W. Rubner, R. Springer, N. Hampe, J. Gehlen, T. M. Magin, B. Hoffmann, and R. Merkel, *Methods Protoc*. **2**, 43 (2019).

[12] G. Tagiltsev, C. A. Haselwandter, and S. Scheuring, *Sci. Adv.* **7**, eabg9934 (2021).

[13] R. Merkel, P. Nassoy, A. Leung, K. Ritchie, and E. Evans, *Nature* **397**, 50 (1999).

[14] H. Liu, X. Liang, and K. Nakajima, *Jpn. J. Appl. Phys*. **59**, SN1013 (2020).

[15] G. Cortelli, L. Patruno, T. Cramer, B. Fraboni, and S. deMiranda, *ACS Appl. Electron. Mater.* (2022).

[16] T. Qian, X. Chen, and F. Hang, *J. Mech. Behav. Biomed. Mater.* **112**, 103989 (2020).

[17] T. Ando, N. Kodera, E. Takai, D. Maruyama, K. Saito, and A. Toda, *Proc. Natl. Acad. Sci. U. S. A.* **98**, 12468 (2001).

[18] L. M. Picco, L. Bozec, A. Ulcinas, D. J. Engledew, M. Antognozzi, M. A. Horton,

and M. J. Miles, *Nanotechnology* **18**, 044030 (2007).

[19] G. Schitter, K. J. Astrom, B. E. DeMartini, P. J. Thurner, K. L. Turner, and P. K. Hansma, *IEEE Trans. Control Syst. Technol.* **15**, 906 (2007).

[20] B. J. Kenton, A. J. Fleming, and K. K. Leang, *Rev. Sci. Instrum.* **82**, 123703 (2011).

[21] M. Kitazawa, K. Shiotani, and A. Toda, *Jpn. J. Appl. Phys.* **42**, 4844 (2003).

[22] T. Ando, T. Uchihashi, and S. Scheuring, *Chem. Rev.* **114**, 3120 (2014).

[23] M. G. Ruppert, B. S. Routley, A. J. Fleming, Y. K. Yong, and G. E. Fantner, *Proceedings of Int. Conference on Manipulation, Automation and Robotics at Small Scales (MARSS)*, Helsinki, Finland, 1–6 (2019).

[24] M. Shibata, T. Uchihashi, T. Ando, and R. Yasuda, *Sci. Rep.* **5**, 8724 (2015).

[25] Y. Nishizawa, H. Minato, T. Inui, T. Uchihashi, and D. Suzuki, *Langmuir* **37**, 151 (2021).

[26] G. R. Heath, E. Kots, J. L. Robertson, S. Lansky, G. Khelashvili, H. Weinstein, and S. Scheuring, *Nature* **594**, 385 (2021).

[27] Y. Ruan, K. Kao, S. Lefebvre, A. Marchesi, P. -J. Corringer, R. K. Hite, and S. Scheuring, *Proc. Natl. Acad. Sci. U. S. A* **115**, 10333 (2018).

[28] T. Uchihashi, Y. Watanabe, Y. Nakazaki, T. Yamasaki, H. Watanabe, T. Maruno, K. Ishii, S. Uchiyama, C. Song, K. Murata, R. Iino, and T. Ando, *Nat. Commun.* **9**, 2147 (2018).

[29] K. Matsuda, M. Sugawa, M. Yamagishi, N. Kodera, and J. Yajima, *FEBS Lett.* **594**, 1237 (2020).

[30] S. R. Nasrin, C. Ganser, S. Nishikawa, A.R. Kabir, K. Sada, T. Yamashita, M. Ikeguchi, T. Uchihashi, H. Hess, and A. Kakugo, *Sci. Adv.* **7**, eabf2211 (2021).

[31] K. Winkler, A. Karner, A. Horner, C. Hannesschlaeger, D. Knyazev, C. Siligan, M. Zimmermann, R. Kuttner, P. Pohl, and J. Preiner, *Nanoscale Adv.* **2**, 3431 (2020).

[32] T. Uchiyama, T. Uchihashi, A. Nakamura, H. Watanabe, S. Kaneko, M. Samejima,

and K. Igarashi, *Proc. Natl. Acad. Sci. U. S. A.* **117**, 19896 (2020).

[33] N. Kodera, M. Sakashita, and T. Ando, *Rev. Sci. Instrum*. **77**, 83704 (2006).

[34] T. Ando, T. Uchihashi, and N. Kodera, *Annu. Rev. Biophys.* **42**, 393 (2013).

[35] M. G. Ruppert, D. M. Harcombe, M. R. P. Ragazzon, S. O. R. Moheimani, and A. J. Fleming, *Beilstein J. Nanotechnol*. **8**, 1407 (2017).

[36] H. Hölscher and U. D. Schwarz, *Int. J. Non. Linear. Mech.* **42**, 608 (2007).

[37] M. Shimizu, C. Okamoto, K. Umeda, S. Watanabe, T. Ando, and N. Kodera, *Rev. Sci. Instrum.* **93**, 013701 (2022).

[38] S. -K. Hung and L. -C. Fu, *IEEE Trans. Instrum. Meas.* **55**, 1648 (2006).

[39] M. Balantekin, S. Satır, D. Torello, and F. L. Değertekin, *Rev. Sci. Instrum*. **85**, 123705 (2014).

[40] T. Akiyama, U. Staufer, and N. F. deRooij, *Appl. Surf. Sci.* **210**, 18 (2003).

[41] J. Otero and M. Puig-Vidal, *Proceedings of 2008 IEEE Instrum. Meas. Technol. Conf.*. 1392–1396 (2008).

[42] S. Fukuda, T. Uchihashi, R. Iino, Y. Okazaki, M. Yoshida, K. Igarashi, and T. Ando, *Rev. Sci. Instrum*. **84**, 73706 (2013).

[43] T. Umakoshi, S. Fukuda, R. Iino, T. Uchihashi, and T. Ando, *Biochim. Biophys. Acta - Gen. Subj.* **1864**, 129325 (2020).

[44] Q. Zou, K. K. Leang, E. Sadoun, M. J. Reed, and S. Devasia, *Asian J. Control* **6**, 164 (2008).

[45] T. Uchihashi, N. Kodera, and T. Ando, *Nat. Protoc.* **7**, 1193 (2012).

[46] Y. -C. Lin, Y. R. Guo, A. Miyagi, J. Levring, R. MacKinnon, and S. Scheuring, *Nature* **573**, 230 (2019).

[47] H. Miyata, R. Yasuda, and K. Kinosita, *Biochim. Biophys. Acta - Gen. Subj.* **1290**, 83 (1996).

[48] M. Walker, P. Rizzuto, M. Godin, and A. E. Pelling, *Sci. Rep.* **10**, 7696 (2020).

49 F. Valle, J. A. DeRose, G. Dietler, M. Kawe, A. Plückthun, and G. Semenza, *Ultramicroscopy* **93**, 83 (2002).

50 T. D. Brown, *J. Biomech.* **33**, 3 (2000).

51 M. Ao, B. M. Brewer, L. Yang, O. E. Franco Coronel, S. W. Hayward, D. J. Webb, and D. Li, *Sci. Rep.* **5**, 8334 (2015).

52 E. Hecht, P. Knittel, E. Felder, P. Dietl, B. Mizaikoff, and C. Kranz, *Analyst* **137**, 5208 (2012).

53 M. Walker, M. Godin, and A. E. Pelling, *Biomed. Microdevices* **20**, 43 (2018).

54 J. Guck, R. Ananthakrishnan, H. Mahmood, T. J. Moon, C. C. Cunningham, and J. Käs, *Biophys. J.* **81**, 767 (2001).

55 A. M. T Quinlan, L. N. Sierad, A. K. Capulli, L. E. Firstenberg, and K. L. Billiar, *PLOS One* **6**, e23272 (2011).

56 E. Puntel, L. Deseri, and E. Fried, *J. Elast.* **105**, 137 (2011).

57 A. T. Sepúlveda, R. G. deVilloria, J. C. Viana, A. J. Pontes, B. L. Wardle, and L. A. Rocha, *Nanoscale* **5**, 4847 (2013).

58 S. Dogru, B. Aksoy, H. Bayraktar, and B. E. Alaca, *Polym. Test.* **69**, 375 (2018).

59 A. Müller, M. C. Wapler, and U. Wallrabe, *Soft Matter* **15**, 779 (2019).

60 I. D. Johnston, D. K. McCluskey, C. K. L. Tan, and M. C. Tracey, *J. Micromechanics Microengineering* **24**, 35017 (2014).

61 H. Liu, J. Yan, M. Kollosche, S.A. Bentil, and S. Laflamme, *Smart Mater. Struct.* **29**, 105037 (2020).

62 M. E. Janson and M. Dogterom, *Biophys. J.* **87**, 2723 (2004).

63 S. Halldorsson, E. Lucumi, R. Gómez-Sjöberg, and R. M. T. Fleming, *Biosens. Bioelectron.* **63**, 218 (2015).

64 K. Efimenko, W. E. Wallace, and J. Genzer, *J. Colloid Interface Sci.* **254**, 306 (2002).

65 Y. Berdichevsky, J. Khandurina, A. Guttman, and Y. -H. Lo, *Sensors Actuators B*

Chem. **97**, 402 (2004).

[66] C. Yu and H. Jiang, *Thin Solid Films* **519**, 818 (2010).

[67] K. Efimenko, M. Rackaitis, E. Manias, A. Vaziri, L. Mahadevan, and J. Genzer, *Nat. Mater.* **4**, 293 (2005).

[68] A. Chiche, C. M. Stafford, and J. T. Cabral, *Soft Matter* **4**, 2360 (2008).

[69] S. Béfahy, P. Lipnik, T. Pardoen, C. Nascimento, B. Patris, P. Bertrand, and S. Yunus, *Langmuir* **26**, 3372 (2010).

[70] S. Singamaneni and V. V. Tsukruk, *Soft Matter* **6**, 5681 (2010).

[71] J. H. L. Beal, A. Bubendorfer, T. Kemmitt, I. Hoek, and W. M. Arnold, *Biomicrofluidics* **6**, 36503 (2012).

[72] J. N. Lee, C. Park, and G. M. Whitesides, *Anal. Chem.* **75**, 6544 (2003).

[73] K. J. Regehr, M. Domenech, J. T. Koepsel, K. C. Carver, S. J. Ellison-Zelski, W. L. Murphy, L. A. Schuler, E. T. Alarid, and D. J. Beebe, Lab Chip **9**, 2132 (2009).

[74] A. Gökaltun, Y. B. Kang, M. L. Yarmush, O. B. Usta, and A. Asatekin, *Sci. Rep.* **9**, 7377 (2019).

[75] L. Yu, *Front. Biosci.* **10**, 2848 (2005).

[76] F. Rusmini, Z. Zhong, and J. Feijen, *Biomacromolecules* **8**, 1775 (2007).

[77] M. Köhler, A. Karner, M. Leitner, V. Hytönen, M. Kulomaa, P. Hinterdorfer, and A. Ebner, *Molecules* **19**, 12531 (2014).

[78] M. González, C.E. Argaraña, and G.D. Fidelio, *Biomol. Eng.* **16**, 67 (1999).

[79] C. M .Dundas, D. Demonte, and S. Park, *Appl. Microbiol. Biotechnol.* **97**, 9343 (2013).

[80] V. Verma, W. O. Hancock, and J. M. Catchmark, *J. Biol. Eng.* **2**, 14 (2008).

[81] Y.- W. Kuo, M. Mahamdeh, Y. Tuna, and J. Howard, *Nat. Commun.* **13**, 3651 (2022).

[82] W. Roos, J. Ulmer, S. Gräter, T. Surrey, and J. P. Spatz, *Nano Lett.* **5**, 2630 (2005).

[83] C. M. Waterman-Storer and E. D. Salmon, *J. Cell Biol.* 139, 417 (1997).

84 C. L. Wymer, S. A. Wymer, D. J. Cosgrove, and R. *J. Cyr, Plant Physiol.* **110**, 425 (1996).

85 T. Li, *J. Biomech.* **41**, 1722 (2008).

86 H. Felgner, R. Frank, and M. Schliwa, *J. Cell Sci.* **109**, 509 (1996).

87 P. Venier, A. C. Maggs, M. F. Carlier, and D. Pantaloni, *J. Biol. Chem.* **269**, 13353 (1994).

88 H. Hess, J. Howard, and V. Vogel, *Nano Lett.* **2**, 1113 (2002).

89 D. Inoue, B. Mahmot, A. M. R. Kabir, T. I. Farhana, K. Tokuraku, K. Sada, A. Konagaya, and A. Kakugo, *Nanoscale* **7**, 18054 (2015).

90 F.-Y. Chan, R. Kurosaki, C. Ganser, T. Takeda, and T. Uchihashi, *Rev. Sci. Instrum.* **93**, 113703 (2022).

91 J. Stricker, T. F Alzone, and M. L. Gardel, *J. Biomech.* **43**, 9 (2010).

92 T. Luo, K. Mohan, P. A. Iglesias, and D. N. Robinson, *Nat. Mater.* **12**, 1064 (2013).

93 J. P. Kemp and W. M. Brieher, *J. Biol. Chem.* **293**, 14520 (2018).

94 E. Miller, L. Stubbington, C. Dinet, and M. Staykova, In *Advances in Biomembranes and Lipid Self-Assembl* **29**, 23– 48 (2019).

95 X. Zhang, X. Hu, H. Lei, J. Hu, and Y. Zhang, *Nanoscale* **8**, 6008 (2016).

96 A. McGough, M. Way, and D. DeRosier, *J. Cell Biol.* **126**, 433 (1994).

97 E. Casal, L. Federici, W. Zhang, J. Fernandez-Recio, E.- M. Priego, R. N. Miguel, J. B. DuHadaway, G. C. Prendergast, B. F. Luisi, and E. D. Laue, *Biochemistr*y **45**, 12917 (2006).

98 M. B. Jensen, V. K. Bhatia, C. C. Jao, J. E. Rasmussen, S. L. Pedersen, K. J. Jensen, R. Langen, and D. Stamou, *J. Biol. Chem*. **286**, 42603 (2011).

99 L. Al-Qusairi and J. Laporte, Skelet. *Muscle* 1, **26** (2011).

100 S. Gowrisankaran, Z. Wang, D.G. Morgan, I. Milosevic, and C. Mim, *J. Mol. Biol.* **432**, 1235 (2020).

[101] K. Ge, J. Duhadaway, D. Sakamuro, R. Wechsler-Reya, C. Reynolds, and G. C. Prendergast, *Int. J. Cancer* **85**, 376 (2000).

[102] B. J. Peter, H. M. Kent, I. G. Mills, Y. Vallis, P. J. G. Butler, P. R. Evans, and H. T. McMahon, *Science* **303**, 495 (2004).

[103] P. L. DeJager, G. Srivastava, K. Lunnon, J. Burgess, L. C. Schalkwyk, L. Yu, M. L. Eaton, B. T. Keenan, J. Ernst, C. McCabe, A. Tang, T. Raj, J. Replogle, W. Brodeur, S. Gabriel, H.S. Chai, C. Younkin, S. G. Younkin, F. Zou, M. Szyf, C. B. Epstein, J. A. Schneider, B. E. Bernstein, A. Meissner, N. Ertekin-Taner, L. B. Chibnik, M. Kellis, J. Mill, and D. A. Bennett, *Nat. Neurosci.* **17**, 1156 (2014).

[104] K. Fujise, S. Noguchi, and T. Takeda, *Int. J. Mol. Sci.* **23**, 6274 (2022).

[105] T. Wu and T. Baumgart, *Biochemistry* **53**, 7297 (2014).

[106] K. Fujise, M. Okubo, T. Abe, H. Yamada, I. Nishino, S. Noguchi, K. Takei, and T. Takeda, *J. Biol. Chem.* **296**, 100077 (2021).

[107] L.-L. Li, Q.-J. Guo, H -Y. Lou, J.-H. Liang, Y. Yang, X. Xing, H.-T. Li, J. Han, S. Shen, H. Li, H. Ye, H. Di Wu, B. Cui, and S.-Q. Wang, *Nano Lett.* **20**, 6387 (2020).

[108] D. Kuscer, O. Noshchenko, H.Uršič, and B. Malič, *J. Am. Ceram. Soc.* **96**, 2714 (2013).

[109] E. Carretti, L. Dei, and P. Baglioni, *Langmuir* **19**, 7867 (2003).

[110] A. F. Routh, *Reports Prog. Phys.* **76**, 046603 (2013).

[111] A. Zosel and G. Ley, *Macromolecules* **26**, 2222 (1993).

[112] T. Kureha, S. Hiroshige, D. Suzuki, J. Sawada, D. Aoki, T. Takata, and M. Shibayama, *Langmuir* **36**, 4855 (2020).

[113] J. A. Brydson, *Plastics Materials*, 7th ed. (Elsevier, 1999).

[114] A. Can, S. Hoeppener, P. Guillet, J.-F. Gohy, R. Hoogenboom, and U. S. Schubert, *J. Polym. Sci. Part A Polym. Chem.* **49**, 3681 (2011).

[115] S. Hiroshige, T. Kureha, D. Aoki, J. Sawada, D. Aoki, T. Takata, and D. Suzuki, *Chem. - A Eur. J.* **23**, 8405 (2017).

[116] C. Ganser and T. Uchihashi, *Nanoscale* **11**, 125 (2019).

[117] A. Notargiacomo, V. Foglietti, E. Cianci, G. Capellini, M. Adami, P. Faraci, F. Evangelisti, and C. Nicolini, *Nanotechnology* **10**, 458 (1999).

[118] M. S. Bull, R. M. A. Sullan, H. Li, and T. T. Perkins, *ACS Nano* **8**, 4984 (2014).

[119] K. Yamanaka, H. Ogiso, and O. Kolosov, *Appl. Phys. Lett.* **64**, 178 (1994).

[120] S. B. Andersson and L. Y. Pao, *Proceedings of 2012 Am. Control Conf.,* 2485–2490 (2012).

[121] Y. K. Yong, A. Bazaei, S. O. R. Moheimani, and F. Allgower, *Proceedings of 2012 2012 IEEE/ASME Int. Conf. Adv. Intell. Mechatronics*, 456–461 (2012).

[122] M. Maiwald, C. Werner, V. Zoellmer, and M. Busse, *Sensors Actuators A Phys.* **162**, 198 (2010).

[123] A. B. Churnside and T. T. Perkins, *FEBS Lett.* **588**, 3621 (2014).

[124] W. H. Liang, Q. Li, K. M. Rifat Faysal, S. J. King, A. Gopinathan, and J. Xu, *Biophys. J.* **110**, 2229 (2016).

[125] C. Leduc, K. Padberg-Gehle, V. Varga, D. Helbing, S. Diez, and J. Howard, *Proc. Natl. Acad. Sci. U. S. A.* **109**, 6100 (2012).

[126] Y. Takahashi, A. I. Shevchuk, P. Novak, Y. Zhang, N. Ebejer, J. V. Macpherson, P. R. Unwin, A. J. Pollard, D. Roy, C. A. Clifford, H. Shiku, T. Matsue, D. Klenerman, and Y. E. Korchev, *Angew. Chemie. Int. Ed.* **123**, 9812 (2011).

Acknowledgement

This thesis can only be finished with the help of everyone I met along this journey.

Firstly, I want to thank my supervisor Prof. Takayuki Uchihashi for his enormous support in research and living in Japan and guided me toward a meaningful destination.

I want to thank Prof. Christian Ganser and Dr. Shigetaka Nishiguchi (ExCELLs, NINS) for their thoughtful advice throughout the study. The discussion with you is always refreshing.

I want to thank Prof. Tadayuki Ogawa (The University of Tokyo) for his precious advice on the microtubule experiment and Prof. Tetsuya Takeda (Okayama University) for his crucial help on the BIN1 experiment.

I want to thank Prof. Ryota Iino, Prof. Akihiro Otomo and Dr. Akasit Visootsat (IMS, NINS) for supporting tubulin preparation and academic discussion.

I want to thank Prof. Chi-Ying Lin (National Taiwan University of Science and Technology), Prof. En-Te Hwu (Technical University of Denmark), and Prof. Ing-Shouh Hwang (Academia Sinica) for their encouragement. Your words are always warm and motivational.

I want to thank Prof. Michio Homma and Dr. Yuichiro Nishizawa for their enthusiastic and altruistic help.

To all the lab members past and present in D Lab at Nagoya University, thank you for all the help with the life and study in Japan.

I want to thank the Ministry of Education of Taiwan for the aid for studying in Japan.

To my family, Mom, Dad, Feng-Tze, Yu-Wen, I appreciate your understanding and belief as well as nourishing my mind.

Finally, Shu-Wen Wang, thank you for always being with me. There is never enough words to express my appreciation to every challenge we have overcome together. Thank you.

Publication List

1. Feng-Yueh Chan, Ryo Kurosaki, Christian Ganser, Tetsuya Takeda, and Takayuki Uchihashi , "Tip-scan high-speed atomic force microscopy with a uniaxial substrate stretching device for studying dynamics of biomolecules under mechanical stress", Review of Scientific Instruments **93**, 113703 (2022), DOI: 10.1063/5.0111017